AN ABSTRACT OF THE DISSERTATION OF

Firas F. Siala for the degree of Doctor of Philosophy in Mechanical Engineering presented on July 24, 2019.

Title: Experimental Investigations of the Unsteady Aerodynamics of Oscillating Airfoils Operating in the Energy Harvesting Regime

Abstract approved: _____

James A. Liburdy

The rising global trend to reduce dependence on fossil fuels has provided significant motivation toward the development of alternative energy conversion methods and new technologies to improve their efficiency. Recently, oscillating energy harvesters have shown promise as highly efficient and scalable turbines, which can be implemented in areas where traditional energy extraction and conversion are either unfeasible or cost prohibitive. Although such devices are quickly gaining popularity, there remain a number of hurdles in the understanding of their underlying fluid dynamics phenomena.

The ability to achieve high efficiency power output from oscillating airfoil energy harvesters requires exploitation of the complexities of the event of dynamic stall. During dynamic stall, the oncoming flow separates at the leading edge of the airfoil to form leading ledge vortex (LEV) structures. While it is well known that LEVs play a significant role in aerodynamic force generation in unsteady animal flight (e.g. insects and birds), there is still a need to further understand their spatio-temporal evolution in order to design more effective energy harvesting enhancement mechanisms.

In this work, we conduct extensive experimental investigations to shed-light

on the flow physics of a heaving and pitching airfoil energy harvester operating at reduced frequencies of $k = fc/U_\infty = 0.06$-0.18, pitching amplitude of $\theta_0 = 75°$ and heaving amplitude of $h_0 = 0.6c$. The experimental work involves the use of two-component particle image velocimetry (PIV) measurements conducted in a wind tunnel facility at Oregon State University. Velocity fields obtained from the PIV measurements are analyzed qualitatively and quantitatively to provide a description of the dynamics of LEVs and other flow structures that may be present during dynamic stall. Due to the difficulties of accurately measuring aerodynamic forces in highly unsteady flows in wind tunnels, a reduced-order model based on the vortex-impulse theory is proposed for estimating the aerodynamic loadings and power output using flow field data. The reduced-order model is shown to be dominated by two terms that have a clear physical interpretation: (i) the time rate of change of the impulse of vortical structures and (ii) the Kutta-Joukowski force which indirectly represents the history effect of vortex shedding in the far wake. Furthermore, the effects of a bio-inspired flow control mechanism based on deforming airfoil surfaces on the flow dynamics and energy harvesting performance are investigated.

The results show that the aerodynamic loadings, and hence power output, are highly dependent on the formation, growth rate, trajectory and detachment of the LEV. It is shown that the energy harvesting efficiency increases with increasing reduced frequency, peaking at 25% when $k = 0.14$, agreeing very well with published numerical results. At this optimal reduced frequency, the time scales of the LEV evolution and airfoil kinematics are matched, resulting in highly correlated aerodynamic load generation and airfoil motion. When operating at $k > 0.14$, it is shown that the aerodynamic moment and airfoil pitching motion become negatively correlated and as a result, the energy harvesting performance is deteriorated. Furthermore, by using a deforming airfoil surface at the leading and trailing edges, the peak energy harvesting efficiency is shown to increase by approximately 17% and 25% relative to the rigid airfoil, respectively. The performance enhancement is associated with enhanced aerodynamic forces for both the deforming leading

and trailing edges. In addition, The deforming trailing edge airfoil is shown to enhance the correlation between the aerodynamic moment and pitching motion at higher reduced frequencies, resulting in a peak efficiency at $k = 0.18$ as opposed to $k = 0.14$ for the rigid airfoil.

Experimental Investigations of the Unsteady Aerodynamics of Oscillating Airfoils Operating in the Energy Harvesting Regime

by

Firas F. Siala

A DISSERTATION

submitted to

Oregon State University

in partial fulfillment of
the requirements for the
degree of

Doctor of Philosophy

Presented July 24, 2019
Commencement June 2020

Doctor of Philosophy dissertation of Firas F. Siala presented on July 24, 2019.

APPROVED:

Major Professor, representing Mechanical Engineering

Head of the School of Mechanical, Industrial, and Manufacturing Engineering

---

Dean of the Graduate School

I understand that my dissertation will become part of the permanent collection of Oregon State University libraries. My signature below authorizes release of my dissertation to any reader upon request.

Firas F. Siala, Author

ACKNOWLEDGEMENTS

First off, I would like to express my sincere appreciation to my advisor Prof. James Liburdy for all of his expertise and guidance throughout the past six years. You constantly challenged and pushed me to my limits to become a better researcher. Your patience, kindness and knowledge have been invaluable to me throughout this long, but extremely rewarding period of my life. I would also like to thank my committee members Profs. Apte, Blunck, Fronk, Pence and Cozzi for agreeing to serve on my committee and for taking the time to read and evaluate my dissertation.

I would like to express my sincere gratitude to my brothers Alexander Totpal and Sebastian Okhovat. Your friendship and continuous moral support have been invaluable to me throughout this journey. Thank you for all the countless memories and adventures in and outside of school.

I would like to thank all my friends whom I have met during graduate school. Forrest Anderson, Pedram Pakseresht, Xiaoliang He, Tabeel Jacob, Mohamed Hrawa, Chaitanya Ghodke, Rishat Ripkat, Roopa Sriram, Laura Herman (soon to be Mrs. Okhovat!!), Kiana Kamrani, Cathy Huang, Amruta Gupte and Ali Mousavian. Each one of you played an important part of my life, and I am very grateful for that. In addition, I would like to thank all of my colleagues that I shared my office with in Rogers Hall: Michael Prier, Brian Tost, Ivan Nepomnyashchikh, Reza Ziazi and Shashank Karra.

I am deeply thankful to my parents, Fuad and Najah, whom without their unconditional love and support (morally and financially), I may have never completed this degree. Thank you for encouraging me in all of my pursuits and inspiring me to follow my dreams. I am eternally indebted to both of you. I would also like to thank my sisters, Noha and Nada, for their continuous support and encouragement. To my brother-in-law, Mohanned, for his encouragement and sense of humor. To my wonderful nieces, Maryam and Nour, for bringing a smile to my face even on my worst days. To my in-laws, for their encouragement and support.

Last, but absolutely not the least, I would like to express my sincere gratitude to my wife and best friend, Marwa. Throughout the past six years, you have been there no matter what. You have endured more than any, the mood-swings and late nights of a graduate student. I am forever grateful for your continuous support.

CONTRIBUTION OF AUTHORS

Prof. James A. Liburdy contributed to the interpretation of results of Chapter 2, 3 and 4. Kiana Kamrani Fard contributed to the editing of Chapter 4.

TABLE OF CONTENTS

TABLE OF CONTENTS (Continued)

Page

LIST OF FIGURES

LIST OF FIGURES (Continued)

LIST OF FIGURES (Continued)

LIST OF FIGURES (Continued)

LIST OF FIGURES (Continued)

Figure Page

LIST OF TABLES

LIST OF APPENDIX FIGURES

Dedicated to my family

Chapter 1 Introduction

The unsteady flow physics around objects has been gaining significant attention within the fluid dynamics community due to its ubiquitous applications in modern engineering. One example of the unsteady phenomena is observed in the flow around airfoils when they experience a rapid change in angle of attack. Such flows are commonly found in the flapping wings of insects and birds (Sane, 2003; Hedenström & Johansson, 2015; Chin & Lentink, 2016), micro-air-vehicles (Ellington, 1999; Mueller, 2001; Ansari *et al.*, 2006) and rotating blades of helicopters and wind/hydro-turbines (Dean, 1959; Seddon & Newman, 2001; Dobrev & Massouh, 2011; Hansen, 2015). The flapping and rotational motion of these systems typically induces large-scale unsteady flow separation that causes significant deviations from the well-known static aerodynamic lift curve, in a process known as dynamic stall. During dynamic stall, flow separates at the leading edge of the airfoil surface and subsequently rolls into leading edge vortices (LEVs). Polhamus (1971) shows that LEVs are beneficial to lift generation by producing a region of low pressure on the suction side of the airfoil, resulting in a strong suction force, as long as they remain attached to the surface. As LEVs increase in size by entraining more vorticity from the separated shear layer, they eventually grow past the airfoil trailing edge, which may result in the roll-up of the trailing edge shear layer into trailing edge vortices (TEVs) (Rival *et al.*, 2014; Widmann & Tropea, 2015). Unlike LEVs, TEVs are known to generally deteriorate lift production by producing a downwash velocity on the airfoil, which decreases the effective angle of attack (Li & Wu, 2016). The growth and evolution of LEVs are thereby of primary interest in the field of unsteady aerodynamics.

The effects described above may occur in diverse fields of applications, however they are especially predominant in oscillating/flapping airfoil aerodynamics at low Reynolds numbers ($Re = U_\infty c/\nu$, where U_∞ is the free stream velocity, c is air-

foil chord length and ν is the kinematics viscosity). Engineering devices based on oscillating airfoils are typically divided into two groups: (i) thrust producing and (ii) energy harvesting devices. Despite the similarities between these two modes of operation, there exist key differences between them. Namely, in thrust producing devices, oscillating airfoils expend energy into the surrounding fluid to propel themselves forward as demonstrated by flying and swimming animals. On the other hand, energy harvesting devices extract energy from oncoming flow to generate power. The transition between thrust generation and energy extraction was investigated by Jones *et al.* (1997) by introducing the *feathering parameter*, χ, to distinguish the regime of propulsion from that of energy harvesting. For heaving and pitching airfoils, the feathering parameter is defined as:

$$\chi = \frac{\theta_0}{arctan(\dot{h}_{max}/U_\infty)} \tag{1.0.1}$$

where θ_0 is the pitching amplitude and $\dot{h}_{max}$ is the maximum heaving velocity. The heaving and pitching motion is typically modeled as:

$$h(t) = h_0 sin(2\pi f t) \tag{1.0.2}$$

$$\theta(t) = \theta_0 sin(2\pi f t + \Phi) \tag{1.0.3}$$

where h_0 is the heaving amplitude, f is the oscillation frequency , Φ is the phase shift between heaving and pitching and t is time. The denominator of Eq. 1.0.1 represents the induced angle of attack that the oscillating airfoil sees as a result of the heaving motion. Based on simple quasi-steady argument, one can show that $\chi < 1$ is associated with thrust generation, while $\chi > 1$ corresponds to energy extraction (Kinsey & Dumas, 2008). In words, for an airfoil to extract energy from the oncoming flow, the amplitude of pitching angle must be greater than the angle of attack induced by the heaving motion.

It is often possible to identify which regime an oscillating airfoil is operating in based on its wake characteristics. Energy harvesting devices generate a

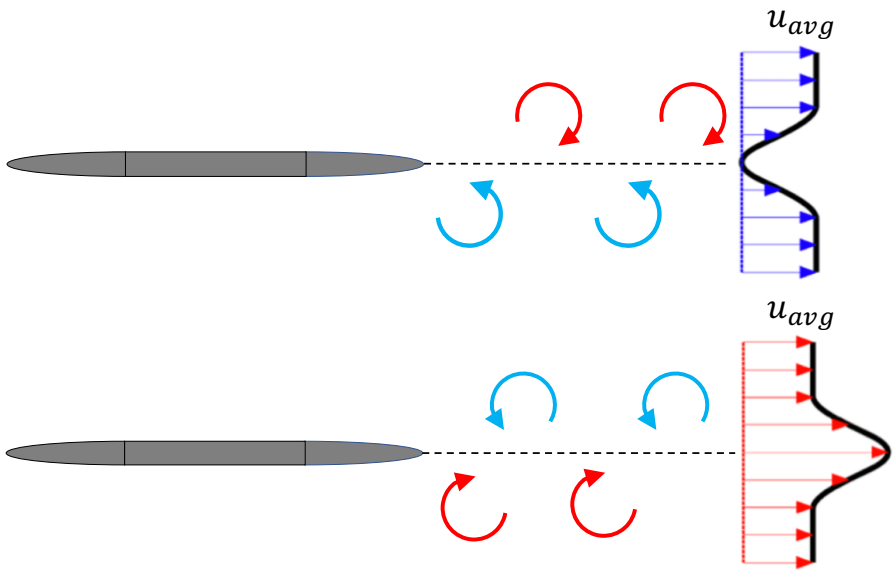

Figure 1.1: (Top) von Kármán vortex street and (bottom) reversed von Kármán vortex street.

von Kármán-like vortex street that results in a wake with momentum deficit, as observed in flows over bluff bodies. In fact, it is hypothesized that the energy extracted by an oscillating airfoil is directly correlated with the energy deficit in its wake (Zhu, 2011). Conversely, thrust producing airfoils generate a reversed von Kármán-like vortex street, where vortices interact to induce a wake with momentum surplus. A sketch of the two different regimes of vortex shedding is shown in Fig. 1.1. Furthermore, the role of LEVs in thrust producing airfoils is well documented and an extensive literature exists from studies of animals and insects (Dickinson *et al.*, 1999; Birch *et al.*, 2004; Muijres *et al.*, 2008; Chen *et al.*, 2017). While the effect of LEVs on lift force production is generally favorable, their formation and coalescence with TEVs weakens the interactions of the wake vortices and therefore reduces thrust efficiency (i.e. the wake momentum surplus is reduced) (Tuncer & Platzer, 2000; Tuncer & Kaya, 2005). However, oscillating airfoil energy harvesters operate in a different flow regime, and unlike oscillating propulsors, they

require high amplitude and relatively large time scales of motion. These kinematic requirements of energy harvesting introduce fundamental fluid dynamics problems that up to this date, have not been thoroughly explored. Specifically, there is a need to understand the coupling of LEV and motion kinematic time scales, as well as the spatio-temporal evolution of the LEV and how to strategically control it in order to achieve high power output.

The concept of flow energy harvesting using oscillating airfoils was first proposed by McKinney & DeLaurier (1981). With the growing importance of renewable energy, the interest in this novel concept has been revived in recent years. In traditional wind/hydro-turbines, the flow around the blades must remain attached to the foil surface to achieve high efficiency levels. This is in contrast to oscillating energy harvesters, where the unsteady flow separation and LEV formation are exploited to attain high power output and efficiency levels. The instantaneous power output of an oscillating airfoil is defined as follows:

$$P = F_y \dot{h} + M\dot{\theta} \tag{1.0.4}$$

where F_y is the force perpendicular to the free stream velocity, M is the pitching moment and $\dot{\theta}$ is the pitching velocity. The power extraction efficiency, η, is defined as the ratio of the cycle-averaged power extracted ($\overline{P}$) to the total power available in the oncoming flow passing through the swept area:

$$\eta = \frac{\overline{P}}{1/2\rho U_\infty^3 SH} \tag{1.0.5}$$

where S is the airfoil span and H is the overall extent of the airfoil motion with both heaving and pitching motions considered. Preliminary studies show that oscillating energy harvesters are capable of extracting energy with efficiencies comparable to rotary devices, and are slowly approaching the maximum theoretical efficiency of 59.3% (known as the Betz limit) (Kinsey & Dumas, 2008; Zhu, 2011; Xiao & Zhu, 2014). Moreover, there are several prominent features of oscillating energy harvesters compared to conventional turbines: (i) they are environmentally friendly

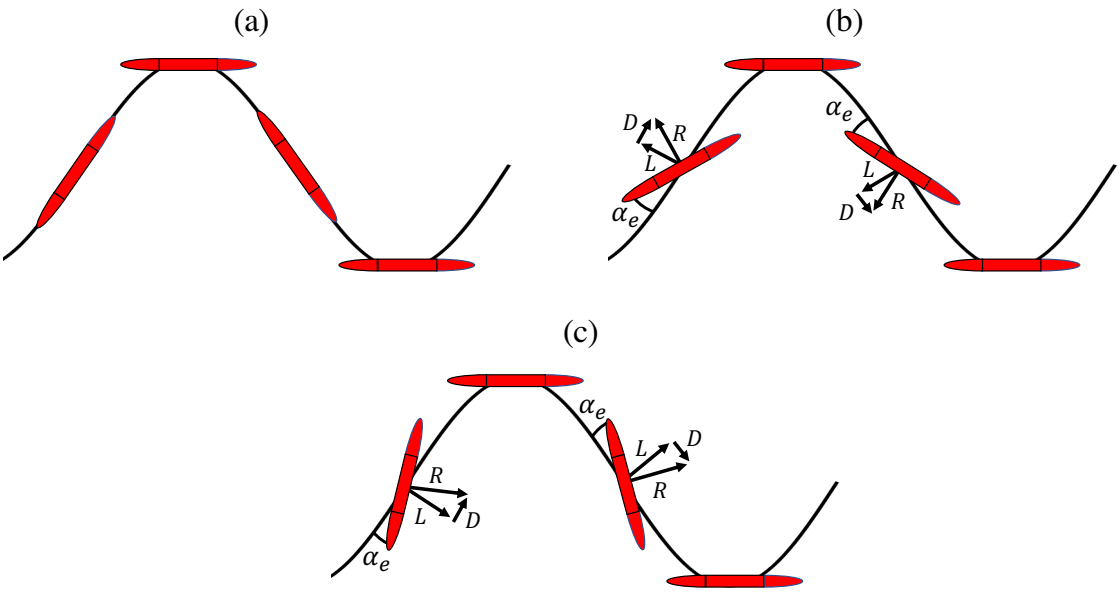

Figure 1.2: Schematic showing the airfoil trajectory and resulting operating regimes. The cases shown here correspond to (a) the feathering limit when $\chi = 1$, (b) the propulsion regime when $\chi < 1$ and (c) the energy harvesting regime when $\chi > 1$.

in terms of noise generation due to their relatively low tip speed, thus reducing impact on the flying/swimming animals; (ii) without centrifugal stress associated with rotating blades, the oscillatory devices are structurally robust and (iii) oscillating devices sweep through a rectangular cross section of the flow, and therefore the swept area of a single foil can be wide and shallow, allowing large systems to be installed in shallow water.

The process of power extraction is illustrated in Fig. 1.2. The sinusoidal curve represents the trajectory of the oscillating airfoil, or the effective flow velocity relative to the airfoil frame of reference. The free stream flow direction is from left to right. The variables L and D represent lift and drag forces, respectively, and R represents the resultant force acting on the airfoil. Figure 1.2a corresponds to a feathering parameter value of $\chi = 1$, which is known as the feathering limit. In

this case, the heaving induced angle of attack is equal to the pitching amplitude θ_0 and therefore they cancel each other out such that the airfoil is always flapping at zero effective angle of attack. Neither energy is extracted nor thrust is produced in this case. Figure 1.2b corresponds to $\chi < 1$. The lift force vector L (and hence the vertical force F_y) is pointing upward when the airfoil is heaving downward, and thus according to Eq. 1.0.4, negative power is generated (i.e. energy is transferred from the airfoil to the surrounding fluid). On the other hand, the airfoil in Fig. 1.2c is operating at $\chi > 1$, where the lift force (and vertical force) vector is pointing downward during the downward stroke of the airfoil, and consequently, the power generated has a positive sign, indicating that energy is transferred from the surrounding fluid to the airfoil. The vast majority of published studies on oscillating energy harvesters have utilized numerical computations to perform parametric investigations and to optimize the overall flow energy harvesting performance (Dumas & Kinsey, 2006; Peng & Zhu, 2009; Zhu, 2011; Kinsey & Dumas, 2012; Kim *et al.*, 2017). It has been shown that energy harvesting efficiency is maximized when the airfoil is oscillating at pitching amplitudes ranging from 60° to 80° and heaving amplitudes of 0.5c-1.0c (Zhu, 2011; Kim *et al.*, 2017). Such large amplitudes of motion are required in order to support leading edge flow separation and the formation of strong and stable LEVs. Furthermore, Kinsey & Dumas (2008) have shown that in order for the LEV to form on the top airfoil surface when it is heaving downward and on the bottom surface when heaving upward, a phase shift between the heaving and pitching of $\Phi = 90°$ is required. This ensures that the lift force generated by the LEV and heaving velocity vectors are aligned positively, thus yielding energy transfer to the device. The contributions of pitching moment to power generation, however, cannot be inferred from a similar quasi-steady argument, as it is highly dependent on the transient trajectory of the LEV along the airfoil chord. In general, the contributions of aerodynamic moment and pitching motion have been shown to have negative effects on power output (Kim *et al.*, 2017).

Of special importance in unsteady aerodynamics is the reduced frequency,

which is a parameter used to define the unsteadiness of the problem:

$$k = \frac{fc}{U_\infty} \tag{1.0.6}$$

The reduced frequency represents the ratio of the time scales of flow convection to airfoil motion ($k = t_{flow}/t_{motion}$, where $t_{flow} = c/U_\infty$ and $t_{motion} = 1/f$). At low reduced frequencies ($k < 0.008$), the airfoil motion time scale is large relative to the convective time scale, meaning that quasi-steady state assumptions can be made. As the reduced frequency increases, the flow dynamics become strongly dependent on the period of the oscillatory motion, and thus quasi-steady state assumption can no longer be made. In energy harvesting applications, the reduced frequency typically ranges from 0.05 to 0.2. When all other parameters are fixed, the energy harvesting efficiency increases monotonically with k, eventually peaking at k = 0.12-0.16. After reaching a peak, it begins to decrease sharply when k is further increased. The peak in efficiency is found to always occur within this same range of reduced frequencies (Kinsey & Dumas, 2012; Liu *et al.*, 2013; Xie *et al.*, 2014). It is well understood that the propulsive efficiency of an oscillating propeller is related to the vortex shedding dynamics in its wake. In general, the vortex shedding of an oscillating airfoil is associated with two different frequencies: (i) the airfoil oscillation frequency and (ii) the *natural* vortex shedding frequency. The natural vortex shedding frequency is related to the inverse of the time it takes for a fluid particle to travel from the leading to the trailing edge of the airfoil. Triantafyllou *et al.* (1993) found that the maximum propulsive efficiency occurs when the propeller operates at a frequency that is equal to the natural vortex shedding frequency. The explanation is that efficiently generated vortex shedding directly contributes to highly efficient thrust generation. Although Zhu (2011) has found that the optimal reduced frequency range of k = 0.12-0.16 also results in the matching of the natural vortex shedding and airfoil oscillation frequencies, it is still not fully understood how the reduced frequency affects the dynamics of the LEV, and hence the energy harvesting performance.

As previously mentioned, the process of LEV generation and shedding plays a significant role in power generation. Specifically, the timing of LEV formation, detachment and shedding is critical to maximize the efficiency of power extraction via changing the local surface pressure distribution (Peng & Zhu, 2009). From Eq. 1.0.4, it can be seen that there are two main factors influencing the power output: (i) the magnitude of the force F_y and aerodynamic moment M and (ii) the correlation between F_y and $\dot{h}$ as well as between M and $\dot{\theta}$. Several studies have been conducted in the past that investigate different mechanisms that enhance both the peak force as well as the correlation between the force and motion (Xiao & Zhu, 2014). One prominent mechanism is the use of deforming airfoils. Previous studies on insect wings as well as fish fins suggest that a certain degree of deformation near the trailing edge may lead to the generation of higher thrust and lift forces. This is attributed to the structural resonance, the manipulation of the LEV generation and the force reorientation associated with the deformations of the surface (Zhao *et al.*, 2011; Nakata *et al.*, 2011; Nakata & Liu, 2012). Surface structural deformation can either be passive or controlled. In controlled flexibility, the deformation of the surface is prescribed whereas the effects of the airfoil inertia and fluid-structure interactions are neglected. Hoke *et al.* (2015) used a 2D laminar simulation with prescribed camber deformation to show that thrust efficiency increases by 16% relative to a purely rigid airfoil. Furthermore, Liu *et al.* (2013) computationally modelled two-dimensional oscillating airfoil energy harvesters with deforming leading and trailing edges. Rather than directly solving the coupled fluid-structure interaction problem, the camber motion is predetermined based on priori results. Their simulations show that airfoil deformation at the trailing edge enhances the strength of the LEV, whereas deformation at the leading edge controls the timing of LEV shedding, and thus the correlation between the aerodynamic forces and airfoil motion.

Passive surface deformation can be divided into two categories: (i) inertia-induced deformation and (ii) flow-induced deformation. Flow-induced deformation can only occur when the airfoil density is comparable with the density of

the surrounding fluid. Tian *et al.* (2014) conducted a numerical model based on immersed-boundary method to study flow energy harvesting by a deforming airfoil. Their results show an 11.3% increase in energy harvesting efficiency by applying control to the leading edge segment. However, for passive flow-induced deformation, no performance enhancement was observed. Totpal *et al.* (2018) have conducted an experimental study to investigate the effects of inertia-induced leading edge deformation at near the airfoil leading edge at $0.04 \leq k \leq 0.08$. While their results show that the leading edge deformation reduces the energy harvesting efficiency by 10% relative to a rigid airfoil at $k \approx 0.08$, the negative effects of the deformation were shown to subside as k was increased from $k = 0.04$ to 0.08. It remains unknown whether at larger reduced frequencies, the effects of inertia-induced leading edge deformation are beneficial.

In order to fully understand the contribution of LEV evolution to the energy harvesting process and how to design flow-control mechanisms that enhance the performance, there is a need to measure the time-resolved aerodynamics forces and synchronize them with the flow structures. In experimental fluid dynamics, the total force on a model is typically measured by mounting it on a load cell instrumented with strain gauges. This approach yields accurate force readings if care is taken to account for the effects of the mounting device on the measured loads. However in wind tunnel experiments, this technique is particularly challenging due to the low density of air compared to the density of airfoil. Totpal (2017) has shown that direct force measurements are limited in their accuracy since at higher reduced frequencies ($k > 0.08$), the inertial forces become quite significant. Inertial forces grow rapidly with oscillation frequency and they can be an order of magnitude larger than the aerodynamic forces, thus further reducing the accuracy of the measurements (Rival *et al.*, 2009). Many researchers recently have applied the classical control-volume approach to estimate the forces, which is often written as:

$$\mathbf{F} = -\frac{d}{dt}\int_{CV} \rho \mathbf{u} dV - \oint_S \mathbf{n} \cdot [(\mathbf{u} - \mathbf{u}_s) \otimes \rho \mathbf{u}] dS + \oint_S \mathbf{n} \cdot (-p\underline{\mathbf{I}} + \underline{\mathbf{T}}) dS \qquad (1.0.7)$$

where $\mathbf{u}$ is the velocity vector, $\mathbf{n}$ is the unit normal vector pointing out of the fluid, $\mathbf{u}_s$ is the velocity of the control volume, p is pressure, $\underline{\mathbf{I}}$ is the identity tensor, $\underline{\mathbf{T}}$ is the viscous stress tensor, CV is control volume and S is the exterior surface of the control volume. The operation $\otimes$ indicates tensor product. The first term on the right-hand side represents the rate of change of momentum in the control volume, the second term represents the net flux of momentum out of the control volume and the third term represents the force required to balance the net pressure and viscous forces on the fluid at the control volume surface. This approach has been used with great success in some experiments where the flow remains steady. In this case, the first and third integrals are assumed to be zero, and the momentum flux is easily measured by a wake survey. However, evaluating Eq. 1.0.7 presents some challenges for unsteady flow applications, namely, because the pressure field must be known. The pressure field can be obtained numerically by solving the pressure Poisson equation given by the divergence of the Navier-Stokes equations. However if the full three-dimensional velocity field is not known, then the continuity equation is not satisfied. Therefore this technique is often unfeasible, because obtaining three-dimensional flow field experimentally can be challenging for oscillating airfoils at very large amplitudes of motion. In addition, evaluating for pressure from the Poisson equation using experimental data poses other challenges in practice due to measurement error accumulation due to the required temporal and spatial derivatives of the velocity field, as well as measurement uncertainty in the boundary conditions, especially at the fluid-solid interfaces (Gurka *et al.*, 1999). Dabiri *et al.* (2014) have addressed these issues, and they suggested evaluating for the pressure by directly integrating the pressure gradient term in the Navier-Stokes equation rather than using the Poisson equation. Their algorithm is based on integrating the pressure gradient along eight paths through each point in the flow field. The starting point of all eight integration paths is located at the control volume boundary. The median of the pressure value obtained from all eight integration paths is then used to estimate the pressure at each point in the field. This can be done because the pressure is a scalar quantity, meaning that

each independent integration path that arrives at a point in the flow is essentially an independent estimate of the pressure at that point.

While the approach discussed above is feasible, it is not physically the most revealing. What appears in various integrands in Eq. 1.0.7 are variables like velocity and pressure, but the mechanisms leading to their specific distributions in a flow field are hidden. These mechanisms arrive from the local dynamics governed by the Navier-Stokes equations, where one sees the spatial and temporal derivatives of the relevant flow variables. There is thus a clear gap between the standard momentum integral equation and the local flow dynamics. Wu *et al.* (2007*b*) derived a force equation based on the vortex impulse. The concept of vortex impulse is discussed in classical texts such as Saffman (1992) and Batchelor (2000). By acknowledging that the rate of change of fluid impulse is related to the force acting on the body, the force equation is written as:

$$\mathbf{F} = -\frac{1}{N-1}\rho\frac{d}{dt}\Big(\int_{\infty}\mathbf{x}\times\boldsymbol{\omega}\Big)dV + \frac{1}{N-1}\rho\frac{d}{dt}\oint_{S_B}\mathbf{x}\times(\mathbf{n}\times\rho\mathbf{u})dS \qquad (1.0.8)$$

where $\boldsymbol{\omega}$ is the vorticity, $\mathbf{x}$ is the position vector from some arbitrarily chosen origin, $N = \nabla\cdot\mathbf{x}$ is the dimension of space and S_B is the body surface and $\mathbf{u}_B$ is the velocity of the moving body. The first term is the vortex impulse, which essentially represents the momentum induced by a vortical structure with vorticity $\boldsymbol{\omega}$ at position $\mathbf{x}$ and the second term represents the inertial force of the virtual fluid displaced by the moving body. The main advantage of this formulation is that the pressure field is not needed to calculate the forces. Only the velocity and vorticity fields are needed, which are easily obtained experimentally. In addition, because the fluid dynamics of oscillating airfoil energy harvesters is dominated by large-scale vortices (i.e. LEVs), it is significantly easier to describe the energy harvesting process in terms of vorticity. The formulation given in Eq. 1.0.8 was derived based on the assumption that the flow field is irrotational far away from the body surface. It has been used with success in cases where the fluid domain is very large such that the irrotational assumption in the far field is valid (Epps, 2010). Noca (1997)

derived a general expression for instantaneous forces in a finite and arbitrarily chosen control volume:

$$\mathbf{F} = -\frac{\rho}{N-1}\frac{d}{dt}\Big(\int_{CV}\mathbf{x}\times\boldsymbol{\omega}\Big)dV + \frac{\rho}{N-1}\frac{d}{dt}\oint_{S_B}\mathbf{x}\times(\mathbf{n}\times\rho\mathbf{u})dS + \oint_S \mathbf{n}\cdot\underline{\boldsymbol{\lambda}}dS \quad (1.0.9)$$

where the tensor $\underline{\boldsymbol{\lambda}}$ is:

$$\underline{\boldsymbol{\lambda}} = \frac{\rho}{2}(\mathbf{u}\cdot\mathbf{u})\underline{\mathbf{I}} - \rho\mathbf{u}\otimes\mathbf{u} - \frac{\rho}{N-1}\Big[\mathbf{u}\otimes(\mathbf{x}\times\boldsymbol{\omega}) + \boldsymbol{\omega}\otimes(\mathbf{x}\times\mathbf{u})\Big] + \frac{1}{N-1}\Big[\mathbf{x}\cdot(\nabla\cdot\underline{\mathbf{T}})\underline{\mathbf{I}} - \mathbf{x}\otimes(\nabla\cdot\underline{\mathbf{T}})\Big] + \underline{\mathbf{T}} \quad (1.0.10)$$

The primary advantage of this formulation is the minimal list of assumptions required for accurate measurement. Noca (1997) showed that this formula is accurate for fully resolved computational results, as well as under-resolved experimental data. That being said, this formulation contains complicated boundary integral terms with unclear physical meanings, which makes it difficult to identify mechanisms responsible for efficient energy harvesting process. One of the motivations of this dissertation is to propose a simplified framework based on the impulse equation where time-resolved experimental data can be used to estimate the aerodynamic forces. The derivation of the impulsed-based force and moment equations from first principles is shown in Appendix A.

In this dissertation, we use wind-tunnel testing and particle image velocimetry (PIV) measurements to conduct extensive investigations of the fluid dynamics of oscillating airfoil energy harvesters. While there are numerous computational fluid dynamics-based studies of oscillating energy harvesters, there is a clear lack of experimental data that can be used for validation and exploring new physical phenomena. We are specifically interested in understanding the process of LEV and TEV formation, LEV spatio-temporal evolution and its detachment, in the range of reduced frequencies relevant to energy harvesting applications. Despite the significance of both LEVs and TEVs, their contributions to aerodynamic force generation and energy harvesting performance are still not fully understood. Con-

sequently, we propose to use the impulse-based force and moment formulation to better understand the effects of LEV and TEV in power production. The impulse approach provides important advantages compared to other traditional approaches such as direct force measurement and conservation of momentum. Particularly, the impulse-based equations are linearly dependent on vorticity (Kang *et al.*, 2018), meaning that the total vortex impulse can be treated as a superposition of impulses of every individual vortex structure in the flow. This provides the impulse approach with great utility for describing power output of an airfoil based on the dynamics of LEV and TEV structures. Upon understanding the role of LEV and TEV in the energy extraction process, we investigate the effects of using inertia-induced airfoil deformation at the leading and trailing edges to control the dynamics of the LEV and TEV in order to enhance the energy harvesting efficiency. The hypothesis is that some degree of deformation at the leading and trailing edges may alter the formation process of both the LEV and TEV and thus power extraction performance. To the best of our knowledge, there exist no experimental data that validate the feasibility of deforming airfoils in the range of reduced frequencies relevant to optimal energy harvesting efficiency

The rest of the dissertation is structured as follows. In Chapter 2, we investigate the effects of reduced frequency on the spatio-temporal evolution of the leading edge vortex. In addition, we provide a simplified version of the impulse-based force equation that contains terms with clear physical meanings. In Chapter 3, we apply the simplified impulse-based approach to estimate the energy harvesting efficiency, as well as to provide new insight into the role played by the LEV and TEV in the energy harvesting process. In Chapter 4, we investigate the feasibility of inertia-based leading and trailing edge deformation in oscillating airfoil energy harvesters. Finally, conclusions of this dissertation and suggestions for future work are given in Chapters 5 and 6, respectively. Detailed uncertainty analysis, derivation of impulse-based equations and a discussion of practical considerations of using experimental data in force calculation are provided in the appendices.

Chapter 2 Leading edge vortex dynamics and impulse-based lift force analysis of oscillating airfoils

Firas F. Siala and James A. Liburdy

Experiments in Fluids
Under Review
Springer Science + Business Media, Berlin, Germany

Abstract

The vortex dynamics and lift force generated by a sinusoidally heaving and pitching airfoil during dynamic stall are experimentally investigated for reduced frequencies of $k = fc/U_\infty = 0.06 - 0.16$, pitching amplitude of $\theta_0 = 75^\circ$ and heaving amplitude of $h_0/c = 0.6$. The lift force is calculated from the velocity fields using the finite-domain impulse theory. The concept of moment-arm dilemma associated with the impulse equation is revisited to shed-light on its physical impact on the calculated forces. It is shown that by selecting an objectively defined origin of the moment-arm, the impulse force equation can be greatly simplified to two terms that have a clear physical meaning: (i) the time rate of change of impulse of vortical structures within the control volume and (ii) Lamb vector that indirectly captures the contribution of vortical structures outside of the control volume. The results show that the trend of the lift force is dependent on the formation of the leading edge vortex, as well as its time rate of change of circulation and chord-wise advection relative to the airfoil. Additionally, the trailing edge vortex, which is observed to only form for $k \leq 0.10$, is shown to have lift-diminishing effects that intensifies with increasing reduced frequency. Lastly, the concept of optimal vortex formation is investigated. The leading edge vortex is shown to attain the optimal formation number of approximately 4 for $k \leq 0.1$, when the scaling is based on the leading edge shear velocity. For larger values of k the vortex growth is delayed to later in the cycle and doesn't reach its optimal value. The result is that the peak lift force occurs later in the cycle. This has consequences on power production which relies on correlation of the relative timing of lift force and heaving velocity.

2.1 Introduction

Flow physics of oscillating surfaces has become a very important area of study for a wide range of applications, such as the development of micro-air vehicles and energy harvesting devices (Tuncer & Platzer, 2000; Zhu, 2011; Mackowski & Williamson,

2015; Siala & Liburdy, 2015). A large contribution to the existing knowledge has come through the studies of flapping flight of insects, birds and bats (Leishman, 1994; Ellington *et al.*, 1996; Ellington, 1999; Madangopal *et al.*, 2005; Platzer *et al.*, 2008; Hubel *et al.*, 2009). The oscillatory/flapping kinematics of these natural fliers may exploit several lift-enhancing mechanisms such as dynamic stall and vortex-wake recapture, among others (Srygley & Thomas, 2002). A common model of oscillatory flight is the combined heaving and pitching motion of an airfoil at large angles of attack, in which the formation and shedding of leading edge vortices (LEVs) exhibit a large impact on the flow behaviour and instantaneous aerodynamic forces (Hubel & Tropea, 2010; Moriche *et al.*, 2017). Although the general role of LEVs is well understood; they produce regions of low pressure on the suction side of the airfoil to generate a large suction force, yet developing fundamental theories that can predict their effects on the transient aerodynamic forces remains to be quite challenging to the aerodynamics community.

Classical unsteady theories of aerodynamics, the most prevalent of which are the models of Wagner (1925) and Theodorsen (1934), have been used extensively with success in problems related to aeroelasticity and fluttering. However, since these models are based on potential flow theory, they do not capture the effects of separated flow and LEVs, thereby limiting their application to small amplitude kinematics where the boundary-layer remains attached throughout the unsteady motion. In recent years, more advanced models based on discrete-vortex methods have been employed to model unsteady flows during dynamic stall (Xia & Mohseni, 2013; Hammer *et al.*, 2014; Liu *et al.*, 2016; Darakananda *et al.*, 2016). In these methods, potential-flow theory is modified to include discrete point vortices to represent free vortical structures and shear layers. Typically, the trajectory of these point vortices is determined by the Kirchhoff velocity (Darakananda *et al.*, 2016) or Brown-Michael equation (Brown, 1954). However, such models are based on some ad-hoc criteria for LEV inception and shedding. For example, the LEV strength must reach an extremum before it is allowed to evolve as a simple point vortex using the Brown-Michael equation. Furthermore, Ramesh *et al.* (2014)

developed the Leading Edge Suction Parameter (LESP), which is equivalent to the first Fourier coefficient (A_0) in unsteady thin airfoil theory, to predict the onset of LEV formation. This method requires calibration using highly resolved simulations to determine a critical LESP value, at which the flow begins to separate from the leading edge. They show that the critical LESP value they determined is universal for a given airfoil geometry and Reynolds number. Once the LEV is formed, its evolution is determined using inviscid flow theory. While this method provides reasonable estimates of aerodynamic force coefficients, it still requires high-cost simulations to pre-determine the onset of flow separation. In addition, the exact contribution of LEVs and other free vortices is not explicitly highlighted, which makes it difficult to develop fundamental theories of vortex dynamics and their role in aerodynamic force production.

An alternative theoretical tool that has been gaining wide attention in recent years is based on the concept of hydrodynamic impulse (Lin & Rockwell, 1996; Epps, 2010; Kim *et al.*, 2013). Originally, the impulse concept was introduced to bypass the integration of total momentum which is not well defined in an infinite region, since in general the momentum integral is only conditionally convergent (Lamb, 1932; Lighthill, 1986*a*; Saffman, 1992; Batchelor, 2000). The impulse-based force equation for an unsteady moving body in unbounded, incompressible flow can be written as follows:

$$\mathbf{F} = -\frac{1}{N-1}\rho\frac{d}{dt}\int_{V_\infty}\mathbf{x}\times\boldsymbol{\omega}dV + \frac{1}{N-1}\rho\frac{d}{dt}\oint_{S_B}\mathbf{x}\times(\mathbf{n}\times\rho\mathbf{u})dS \qquad (2.1.1)$$

where ρ is fluid density, $\mathbf{x}$ is the position vector, $\boldsymbol{\omega}$ is the vorticity vector, $\mathbf{u}$ is the velocity vector, $\mathbf{n}$ is the normal unit vector and $N = \nabla\cdot\mathbf{x}$ is the dimension of space. The first term is evaluated over the entire flow field (V_∞) and represents the rate of change of flow impulse. The second term is evaluated over the body surface (S_B) and is equivalent to the added mass force produced by the moving body. One particular constraint with this formulation is that the entire vorticity field must be captured in the control volume (V_∞). Practically, this limits its use to the early

times of impulsively-started flows, where the entire vorticity field remains inside the control volume.

The use of impulse theory has also gained popularity in constructing semi-empirical low-order models. For example Babinsky *et al.* (2016) and Stevens & Babinsky (2017) have applied a linearized version of the impulse formulation (Kármán, 1938) to experimental data to model the transient lift force of impulsively pitching and surging airfoils. They decomposed the rate of change of impulse into two terms: vortex circulation growth and vortex advection, where both terms are calculated empirically from experimental data. They show that the total lift force at the beginning of the motion is primarily dictated by the LEV growth. Once the LEV stops growing, the LEV advection relative to the trailing edge vortex (TEV) becomes more dominant. Overall, they obtain reasonable lift force estimates by assuming that all relevant vorticity is contained within the LEV and TEV. Furthermore, Wang & Eldredge (2013) used the impulse-matching approach (Tchieu & Leonard, 2011) in conjunction with discrete-vortex methods to model the effects of LEVs on impulsively started flat plates at various angles of attacks. The impulse-matching approach is used as an alternative to the Brown-Michael equation in order to relax the vortex shedding criterion required by the latter method. One limitation associated with this approach that the authors address is the use of the Kutta condition to determine the vortex strength as a function of time. They suggest that calculating the vortex strength empirically might improve the accuracy of their model. Ideally, one may develop universal scaling laws of vortex dynamics for a wide range of operational parameters that can be used as inputs in such models. For example, the idea of optimal vortex formation number (Dabiri, 2009) could potentially serve as a unifying principle in constructing low-order models under the proper conditions. Onoue & Breuer (2016) investigated the LEV formation number of pitching airfoils for a wide range of amplitudes, reduced frequencies and Reynolds numbers. They show that the time-history of LEV circulation growth collapses on a single curve, where the maximum formation number was found to approximately equal to 4, agreeing remarkably well with the theory (Gharib *et al.*,

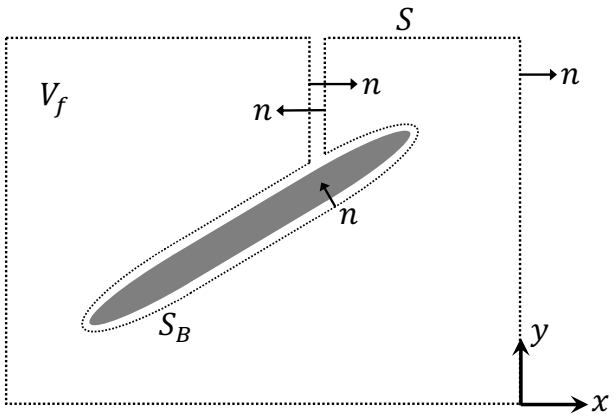

Figure 2.1: Domain of integration for the evaluation of aerodynamic forces on an airfoil.

1998).

Noca (1997) has expanded on the impulse theory and derived the force equation for arbitrary finite domains using the derivative moment transformation (DMT) identity (Wu *et al.*, 2007*b*). The force equation is written as follows:

$$\mathbf{F} = -\frac{1}{N-1}\rho\frac{d}{dt}\int_{V_f}\mathbf{x}\times\boldsymbol{\omega}dV + \oint_S \mathbf{n}\cdot\Big(\frac{\rho}{2}u^2\underline{\mathbf{I}} - \rho\mathbf{u}\otimes\mathbf{u}\Big)dS + \oint_S \mathbf{n}\cdot\boldsymbol{\lambda}_{\mathbf{imp}}dS + \frac{1}{N-1}\rho\frac{d}{dt}\oint_{S_B}\mathbf{x}\times(\mathbf{n}\times\mathbf{u})dS \quad (2.1.2)$$

where V_f is the fluidic volume, S is the exterior surface of the control volume and S_B is the airfoil surface. The term $\boldsymbol{\lambda}_{\mathbf{imp}}$ may be written as follows:

$$\boldsymbol{\lambda}_{\mathbf{imp}} = \frac{\rho}{N-1}\boldsymbol{\omega}(\mathbf{x}\times\mathbf{u}) - \frac{\rho}{N-1}[\mathbf{u}\otimes(\mathbf{x}\times\boldsymbol{\omega})] + \underline{\mathbf{T}} + \frac{1}{N-1}[\mathbf{x}\cdot(\nabla\cdot\underline{\mathbf{T}})\underline{\mathbf{I}} - \mathbf{x}\otimes(\nabla\cdot\underline{\mathbf{T}})] \quad (2.1.3)$$

where $\underline{\mathbf{I}}$ and $\underline{\mathbf{T}}$ represent the identity and stress tensors, respectively. Unsteady force evaluation based on the finite-domain impulse theory has attracted wide

attention among the experimental fluid dynamics community, as it is often not feasible to directly measure the aerodynamic forces on moving airfoils due to challenges in separating the inertial contributions (Rival *et al.*, 2009). This is especially problematic in wind tunnel experiments, where the density of the airfoil can be orders of magnitude greater than the density of air (Totpal, 2017). Other force estimation techniques based on the integral momentum approach requires the evaluation of the pressure field which can be a non-trivial task in experimental fluid dynamics (Van Oudheusden, 2013). Although many researchers have successfully computed the pressure field and obtained reasonable force estimates (Liu & Katz, 2006; Charonko *et al.*, 2010; Dabiri *et al.*, 2014; Villegas & Diez, 2014), these methods provide a global force estimation, where the contributions of the local vortical structures are hidden. Several authors applied Eq. 2.1.2 , or other forms of it, to experimental (Noca, 1997; Baik *et al.*, 2011; DeVoria *et al.*, 2014; Siala *et al.*, 2018) and numerical (Li & Lu, 2012; Mohebbian & Rival, 2012; Kang *et al.*, 2018) data to calculate the unsteady lift force. The impulse approach offers various distinct advantages. Firstly, it does not require the evaluation of the pressure field, which is very practical for experiments based on particle image velocimetry (PIV). Secondly, the force can be easily decomposed into circulatory (rate of change of vortex impulse) and non-circulatory (added mass) contributions, which provides useful insights of the physical mechanisms responsible for force generation. In fact, this decomposition is similar to that found in Therodorsen's model (Theodorsen, 1934), except that it also includes the effects of free vortices. Thirdly, and perhaps most importantly, the impulse-based force equation is linearly dependent on vorticity, which means that the total impulse in the flow field can be treated as a superposition of impulses of every individual vortex structure in the flow. These advantages provide the impulse approach with great utility for theoretical modeling of unsteady airfoils exhibiting dynamic stall, as it is easier to describe these flows in terms of vorticity.

One particular challenge with Eq. 2.1.2 is that it contains cumbersome boundary integral terms with ambiguous physical meanings, which makes it difficult to

identify the mechanisms responsible for the lift production and to construct low-order models. Kang *et al.* (2018) proposed using the minimum-domain impulse theory, which greatly simplifies Eq. 2.1.2 by dropping many of the surface integral terms. The requirement for using their theory is that the control volume must not cut through regions of significant vorticity. They follow the idea of Flood Fill (Torbert, 2016) to choose a different control volume at each instant in time to find a critical vorticity threshold under which the minimum domain theory is valid. While this method is effective, it may be difficult to experimentally pursue, since one is highly limited by the field of view provided by the PIV imaging system.

Inspired by the studies cited above, in this paper we conduct two component PIV measurements to study the vortex dynamics and unsteady lift force production mechanisms of a periodically oscillating airfoil undergoing dynamic stall. The airfoil kinematics is combined heaving and pitching with very large amplitudes of motion. We are specifically interested in operating at low reduced frequencies associated with efficient energy harvesting applications (Zhu, 2011), where there is a dearth of knowledge concerning the evolution of LEV strength, size and trajectory. Furthermore, in the pursuit of loosening the criterion of the minimum domain theory of Kang *et al.* (2018) to provide more flexibility, we provide an alternative method to significantly reduce the impulse-based force equation. The unsteady lift force is then synchronized with the flow field to highlight the contributions of vortical structures. The results of this work will aid in constructing low-order models of the aerodynamic forces generated during dynamic stall for continuously oscillating/flapping airfoils (as opposed to impulsively started flows).

2.2 Methodology

2.2.1 Experimental setup

Experiments were conducted in a closed-loop wind tunnel ($1.37 \times 1.52\ m$) with turbulence intensities below 2%. The airfoil was fabricated using fused deposition modeling out of acrylonitrile butadiene styrene (ABS), and has a chord length,

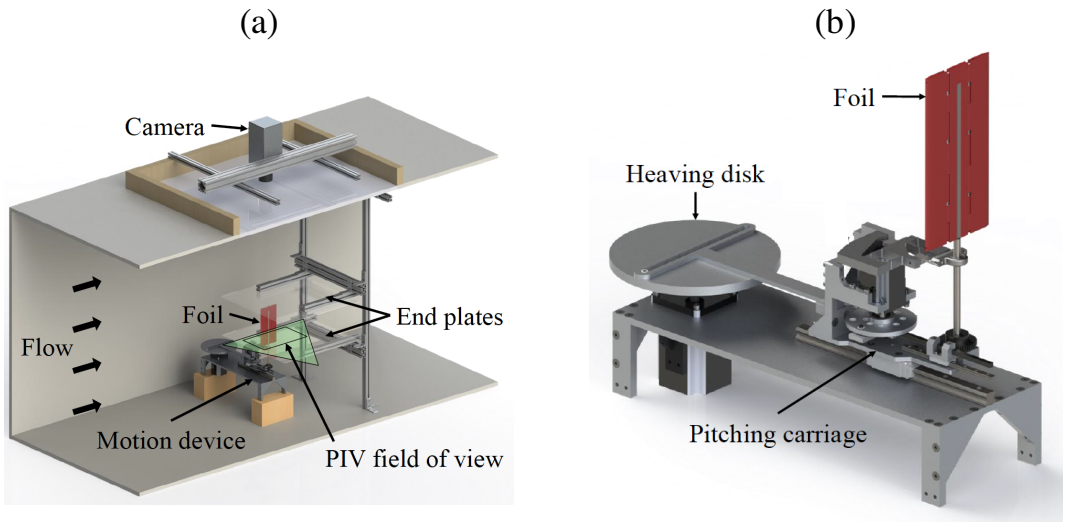

Figure 2.2: (a) Drawing of the experimental setup illustrating the motion device, airfoil orientation and optical system and (b) zoomed-in view of the motion device. Figures are adopted from Totpal (2017).

aspect ratio, and thickness of 125 mm, 2, and $0.05c$, respectively. The leading and trailing edge tips are elliptical with a major to minor axis of 5:1. Stationary end plates were placed approximately 2 mm away from the side-edges to suppress the formation of tip vortices and to simulate two dimensional flow conditions. The airfoil is attached to a motion device using a titanium rod spanning through the mid-chord of the airfoil. The motion device is used to generate the heaving and pitching motion of the airfoil according to the following equations:

$$h(t) = h_0 cos(2\pi f t) \tag{2.2.1}$$

$$\theta(t) = \theta_0 cos(2\pi f t + \Phi) \tag{2.2.2}$$

where h_0 is the heaving amplitude, f the oscillation frequency, θ_0 the pitching amplitude, Φ the phase shift between heaving and pitching and t is time. Heaving was achieved using a scotch-yoke mechanism and the pitching motion used a

combination of a scotch-yoke mechanism and a rack and pinion arrangement. The motion device was controlled using a LabVIEW program. The airfoil motion has been previously verified by Totpal (2017). The experimental setup in the wind tunnel and the motion device are sketched in Fig. 2.2.

Two-component, phase-locked PIV measurements were collected using a dual-head Nd:YAG pulsed laser (EverGreen, 145 mJ/pulse, max repetition rate of 15 Hz) operating at the 532 nm wavelength. A light sheet of approximately 1.5 mm thickness was generated at the mid-span of the airfoil using a LaVision optics module. An in-house designed Laskin nozzle atomizer provided the seeding particles using vegetable oil. Particle images were collected using a CCD camera (Image Pro, LaVision) with a resolution of 1600 $\times$ 1200 pixels. The camera was equipped with a 50 mm focal length lens and a band-pass filter centered at 532 nm. The PIV system was configured to obtain a vector field resolution of 1.8 mm (approximately 70 vectors per chord length). PIV images were processed with DaVis v8.4 software. Particle position displacements were determined using a cross-correlation method on sequential images. The calculations were conducted on two passes of interrogation window size of 64 $\times$ 64 pixels, followed by two passes of interrogation window size of 32 $\times$ 32 pixels, where a 50 % over-lap was used. A high accuracy sub-pixel peak fitting algorithm specific to DaVis® software was used for the final passes. The time between pulses was set such that an average of 8 pixel displacement per interrogation window was achieved in the streamwise direction. Minimum peak validation of 1.2 (ratio of the highest to second highest correlation peaks) and moving-average validation schemes were used to reject outliers, with a vector rejection rate of less than 2%.

The phase-locked velocity fields were calculated by averaging one hundred images at each phase of interest. A total of 116 phases throughout the downstroke motion with an equal spacing of $\Delta t/T = 0.004$ (where T is the oscillation period) were acquired. The PIV system and airfoil motion were synchronized using LabVIEW. The motion device was run for at least 5 minutes prior to collecting PIV measurements to eliminate any initial transient effects.

The use of Eq. 2.1.2 to calculate the aerodynamic forces requires capturing the entire flow field surrounding the airfoil. In order to obtain data in the shadow region caused by the laser illumination, the experiments were repeated at a phase delay of 180° for each phase of interest. The 180° out of phase flow fields were then mirrored and stitched to the rest of the vector field to construct the full flow field surrounding the airfoil. This can be done because the flow, airfoil shape and motion are all symmetric. A similar approach was used by Lua *et al.* (2015). Additionally, a second camera was used to capture the flow field in the downstream region. The two cameras were overlapped by 14 vectors and the overlapped region was smoothed with a 3×3 moving-average filter.

2.2.2 Uncertainty quantification

The particle displacement uncertainty was calculated using the statistical correlation technique developed by Wieneke (2015). Note that this method only estimates the random errors that are associated with camera noise, particle focus and out-of-plane motion, among others (Willert & Gharib, 1991), whereas the systematic errors that are typically influenced by the calibration errors and peak-locking effects are not taken into account. For calibration, we use the pinhole fitting model, and the root mean square of the fit is 0.33 pixels. The peak-locking effect was avoided by using particle image size of approximately 2.1 pixels (estimated from the peak width of the autocorrelation peak of a typical particle image), which is greater than the minimum size of 1 pixel (Wieneke, 2015). The particle displacement uncertainty was then propagated to velocity and vorticity calculations using the technique provided by Sciacchitano & Wieneke (2016). Finally, the uncertainty was propagated to estimate the uncertainty in the lift force. The maximum and mean uncertainties of the velocity components, span-wise vorticity and aerodynamic lift force are listed in Table 2.1 as a percentage of their respective maximum values. We also include uncertainty of free stream velocity measured in the wind tunnel without the airfoil and motion device. All uncertainties are reported using a 95% confidence interval.

Variable	Maximum uncertainty (%)	Mean uncertainty (%)
U_∞	0.3	0.2
u	3.5	1.3
v	5.8	2.1
ω_z	9.1	4.7
F_y	13.6	8.2

Table 2.1: Maximum and mean uncertainty of free stream velocity, velocity components, span-wise vorticity and aerodynamic lift force. All uncertainties are reported using a 95% confidence interval.

As pointed out in the previous section, one of the main motivations of this work is the need for an alternative tool to estimate the transient aerodynamics forces, since direct force measurement of high amplitude oscillating airfoils operating in wind tunnels is usually unfeasible. Unsteady aerodynamic flows indicate that the time scale of airfoil motion is smaller than the time scale of the flow, where the degree of unsteadiness is often described by the reduced frequency ($k = fc/U_\infty$). The difficulty in measuring transient forces of highly unsteady airfoils is due to the inertial forces growing rapidly at high oscillation frequencies (proportional to f^2), whereas the aerodynamic forces grow with U_∞^2. In fact, when $k > 0.08$, the inertial forces become at least an order-of-magnitude larger than the aerodynamic forces, and therefore the accuracy of the force measurements becomes unreliable. For this reason in this study, accurate direct force measurements for $k > 0.08$ are not presented.

In Fig. 2.3 , the transient lift force coefficient ($C_y = 2F_y/\rho U_\infty^2 c$) obtained from the impulse formulation is compared with the results obtained from direct force measurements during the downstroke motion at $k = 0.06$ and $k = 0.08$. It is shown that the force magnitude and trend are well captured by the impulse formulation. The largest discrepancy occurs at the beginning of the downstroke, where the flow remains fully attached to the airfoil surface. Here, the force generation is dominated by the bound vorticity, which is not well resolved by the PIV experiments, and as a consequence, the impulse-based formulation under-predicts

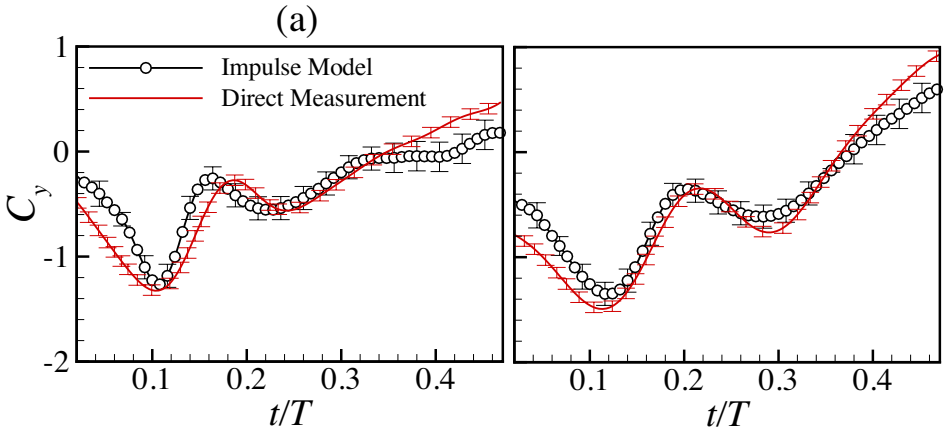

Figure 2.3: Comparison of the transient lift coefficient obtained from the impulse formulation with the results obtained from direct force measurements at (a) $k = 0.06$ and (b) $k = 0.08$; results are given for the half cycle beginning when the foil is at the top heaving position.

the force. Once the flow at the leading edge separates and forms an LEV, the impulse formulation and direct force measurement are in excellent agreement. At this point, it is expected that the contribution of surface vorticity to the lift force becomes negligible (Moriche *et al.*, 2017). The explanation for this has been provided by Ford & Babinsky (2013), who have shown that the bound circulation (due to surface vorticity) of unsteady airfoils at large angles of attack tends toward zero and the total circulation can be considered wholly contained within the LEV. For the motion kinematics used in this study, the flow is observed to be attached to the airfoil surface for only a relatively short period of time, thus providing validity in the use of impulse formation.

2.3 Results

In this section, we present results for reduced frequencies of $k = 0.06 - 0.16$, while holding the heaving amplitude, pitching amplitude, phase shift and pitching axis

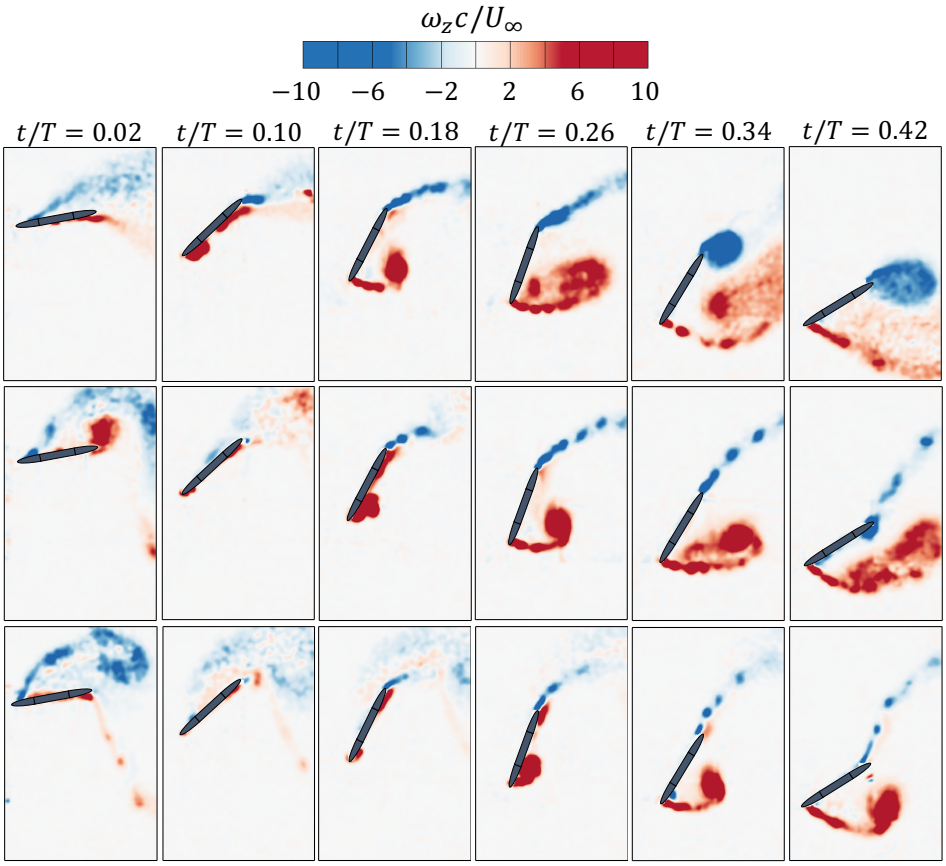

Figure 2.4: Vorticity field for discrete phases during the downstroke. Top row: $k = 0.06$, middle row: $k = 0.10$ and bottom row: $k = 0.14$.

fixed at $h_0/c = 0.6$, $\theta_0 = 75°$, $\Phi = 90°$ and $x_p/c = 0$ (mid-chord), respectively. These parameters have been shown to produce high energy harvesting efficiencies (Zhu, 2011). Due to the symmetry of the problem, the results are only provided for the downstroke motion of the airfoil.

2.3.1 Evolution of vorticity field

Figure 2.4 shows the non-dimensional spanwise vorticity evolution for $k = 0.06$, 0.10 and 0.14. The flow approaches from the left-hand side and the non-dimensional time $t/T = 0$ corresponds to the top heaving position and $t/T = 0.5$ is the bottom heaving position. For $k = 0.06$, the leading edge shear layer on the top surface of the airfoil is shown to be separated due to the LEV shedding during the upstroke motion. Once the angle of attack is large enough (in the negative direction), the shear layer becomes attached to the top surface, while it begins to separate and roll-up into an LEV on the bottom surface at $t/T \approx 0.10$. The shear layer feeds the LEV with vorticity, which results in the increase of LEV strength and size over time. By the time the LEV grows past the trailing edge ($t/T \approx 0.26$), the trailing edge shear layer begins to roll-up into a trailing edge vortex (TEV). Eventually, the LEV and TEV both shed into the wake to form a Karman-like vortex street (i.e. drag producing wake). For $t/T > 0.42$, the flow over the airfoil is completely separated and full stall is attained.

Early in the cycle for $k = 0.10$, it is shown that a coherent positive vortical structure is shed from the trailing edge. This corresponds to the TEV formed during the upstroke. Since the convective time scale of the flow for high reduced frequencies is relatively larger than for lower reduced frequencies, the formation and advection of flow structures occurs at a slower rate for $k = 0.10$ when compared to $k = 0.06$. The leading edge shear layer separates and rolls into an LEV at $t/T \approx 0.18$. The TEV begins to form at $t/T \approx 0.42$, however its size is significantly smaller than for $k = 0.06$. In addition, the TEV is shown to completely roll on top of the bottom surface of the airfoil before convecting into the wake.

For $k = 0.14$, at early times a large negative vortex structure is observed in the near wake of the airfoil. This is the LEV that was shed during the upstroke. The convective time scale at this reduced frequency is significantly smaller than the airfoil oscillation time scale, thereby enabling the airfoil at the beginning of downstroke to capture the LEV from the upstroke. Similarly to $k = 0.06$ and 0.10, the shear layer from the bottom surface eventually rolls into an LEV ($t/T \approx$

0.260). Furthermore, it is shown that by the time the LEV approaches the trailing edge, the airfoil is already at a relatively small geometric angle of attack and so the trailing edge shear layer is not strong enough to roll-up into a TEV.

The conclusions of the above discussion are as follows. First, the inception of the LEV is delayed in time for larger reduced frequencies. As the reduced frequency increases, the time scale of the airfoil motion becomes smaller relative to the flow time scale. This means that the shear layer takes a longer time to react to the change of angle of attack when k is larger, thus delaying flow separation. Second, the growth rate of the LEV decreases with increasing reduced frequency. This is the result of the decrease of the feeding shear layer velocity at higher reduced frequencies. This is explained as follows. The shear layer velocity can be approximated as the vector sum of the local velocity of the leading edge and the component of the free stream in the direction of the airfoil motion (Onoue & Breuer, 2016):

$$U_{SL} = U_{\infty} sin(\theta) - \dot{h} cos(\theta) - \frac{\dot{\theta} c}{2} \tag{2.3.1}$$

where $\dot{h}$ and $\dot{\theta}$ represent the heaving and angular pitching velocities, respectively. As the reduced frequency increases (by either decreasing the free stream velocity or by increasing the oscillation frequency), the shear layer velocity decreases. Lastly, when k is less than 0.12, the trailing edge shear layer rolls into a TEV. Siala *et al.* (2017) have shown that when the LEV reaches the trailing edge, a saddle point is created downstream of the airfoil trailing edge, which forces the trailing shear layer to roll-up into a TEV. This phenomena was also reported by Rival *et al.* (2014) and Widmann & Tropea (2015).

2.3.2 Leading edge vortex dynamics

In this section the LEV spatio-temporal dynamics are evaluated which will aid in understanding the mechanisms responsible for the lift force production. The LEV circulation and its trajectory are computed based on the vortex identification technique proposed by Graftieaux *et al.* (2001). In this method, two scalar functions

Γ_1 and Γ_2 derived from the velocity vector field, are used to identify the vortex core location and its boundary, respectively, and are given by:

$$\Gamma_1(p) = \frac{1}{N}\sum_{i=1}^{N}\frac{((\boldsymbol{x_p} - \boldsymbol{x_i}) \times \boldsymbol{u_i}) \cdot \hat{\boldsymbol{z}}}{||\boldsymbol{x_p} - \boldsymbol{x_i}|| \cdot ||\boldsymbol{u_i}||} \tag{2.3.2}$$

$$\Gamma_2(p) = \frac{1}{N}\sum_{i=1}^{N}\frac{((\boldsymbol{x_p} - \boldsymbol{x_i}) \times (\boldsymbol{u_i} - \overline{\boldsymbol{u}}_{\boldsymbol{p}})) \cdot \hat{\boldsymbol{z}}}{||\boldsymbol{x_p} - \boldsymbol{x_i}|| \cdot ||\boldsymbol{u_i} - \overline{\boldsymbol{u}}_{\boldsymbol{p}}||} \tag{2.3.3}$$

Subscript i denotes any point in the flow field, $\boldsymbol{x_p}$ is the position vector, $\hat{\boldsymbol{z}}$ is the unit vector in the z direction, N is the total number of points in a subregion and $\overline{\boldsymbol{u}}_{\boldsymbol{p}}$ is the average velocity evaluated in a sub-region. We evaluate Γ_1 and Γ_2 at every point in the flow field using a 3×3 sub-region ($N = 9$). The vortex core is identified by $|\Gamma_1| \geq 0.9$ and the vortex boundary is characterized by $|\Gamma_2| \geq 2/\pi$ (Graftieaux *et al.*, 2001). Overall, this procedure has been found to provide reliable and reproducible definitions of vortex structures (Morse & Liburdy, 2009; Baik *et al.*, 2012; Dunne & McKeon, 2015). The LEV circulation is then calculated by integrating the vorticity enclosed by the contour $|\Gamma_2| = 2/\pi$. To calculate the LEV trajectory, the measured velocity vector field is rotated and translated at each instant in time according to the airfoil kinematics given in Eq. 2.2.1 and 2.2.2. This is is done so that the LEV trajectory is calculated in the frame of reference of the airfoil. Then, the location of the largest value of Γ_1 (on the condition that it is greater than 0.9) is tracked for the entire time until the LEV begins to leave the control volume.

In Fig. 2.5a the LEV circulation normalized by the average shear layer velocity and chord length is plotted versus t/T for all reduced frequencies. It is worthwhile to mention that this non-dimensionalization of LEV circulation is analogous to the optimal vortex formation number given by Dabiri (2009). This concept is based on the argument that for a vortex generator with a given length scale and feeding shear layer velocity, the maximum possible vortex formation number is approximately equal to 4. Here, the airfoil can be thought of as a vortex generator

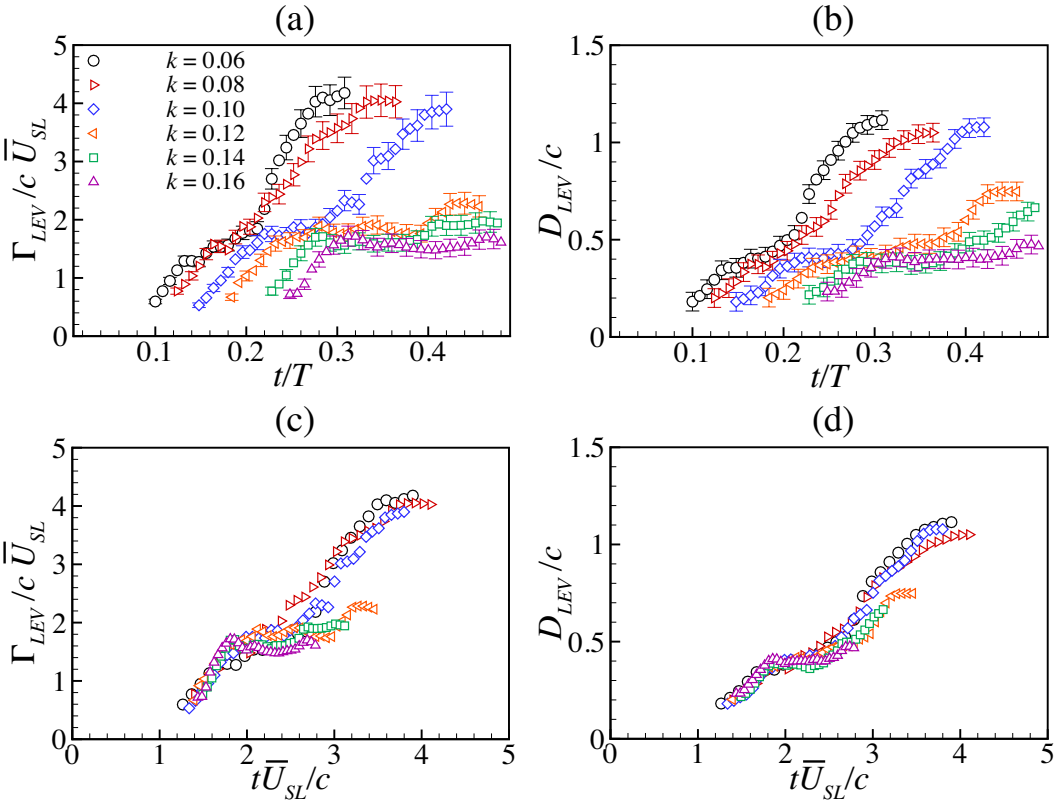

Figure 2.5: Normalized LEV circulation versus (a) t/T and (b) $t\overline{U}_{SL}/c$. Normalized LEV area versus (c) t/T and (d) $t\overline{U}_{SL}/c$. For clarity, only every other data point is plotted.

with a length scale c and average feeding shear layer velocity $\overline{U}_{SL}$. It is shown that for $k \leq 0.10$, the maximum circulation is approximately 3.8-4. In this case, the shear layer feeds the LEV with vorticity until the LEV grows to the size of airfoil chord length (Fig. 2.5b). At this point, there is flow reversal due to TEV formation which interacts with the leading edge feeding shear layer. This results in the separation of the LEV from the shear layer. This mechanism of vortex detachment is similar to what is observed in flows past bluff-bodies (Widmann & Tropea, 2015). Conversely, when $k \geq 0.12$, the relatively small oscillation time

scales of the airfoil results in the maximum LEV circulation (Fig. 2.5a) and size (Fig. 2.5b) to be significantly reduced. That is, the LEV begins to form quite late in the downstroke, and thus the end of downstroke is reached before the LEV reaches its maximum possible circulation and size. The result is much lower peak values of the normalized strength of the LEV at higher reduced frequencies.

The normalized LEV circulation and diameter are plotted versus time using the shear layer-based convective time scale, $c/\overline{U}_{SL}$ in Fig. 2.5c and 2.5d, respectively. For $k \leq 0.12$, the LEV circulation and diameter are shown to collapse to a single curve and their maximum respective values are attained at $t\overline{U}_{SL}/c \approx 4$, agreeing remarkably well with the concept of universal vortex formation time (Gharib *et al.*, 1998). For $k \geq 0.12$, both the circulation and diameter also collapse well with the rest of the data in the early times during the cycle, however as discussed above, their maximum values are much smaller than for $k \leq 0.10$. In addition, there seems to be no universal vortex formation time for these higher reduced frequency values, but rather the maximum formation time is seen to decrease with increasing reduced frequency. Lastly, it may be interesting to note that for all reduced frequencies, the time of LEV inception occurs at $t\overline{U}_{SL}/c \approx 1.4$. This inception timescale was also observed by Siala *et al.* (2017) using the same reduced frequencies but different pitching and heaving amplitudes. This may suggest that the concept of optimal vortex formation may serve as a tool to predict the onset and growth of LEV circulation and size for combined heaving and pitching airfoils, at least for relatively low reduced frequencies which are greatly influenced by the LEV dynamics.

In Fig. 2.6a the chord-normal trajectory of the LEV, Y_{LEV}/c, is plotted versus t/T for all reduced frequencies. After LEV formation, the LEV remains very close to the airfoil surface ($Y_{LEV}/c = 0$) for a very short period of time. Meanwhile, the LEV is shown to convect along the chord at approximately the same rate for all reduced frequencies until it approaches the airfoil mid-chord ($X_{LEV}/c = 0$), as is shown in Fig. 2.6b. Afterwards, the LEV begins to travel away from the airfoil surface, while it remains approximately stationary near the mid-chord for

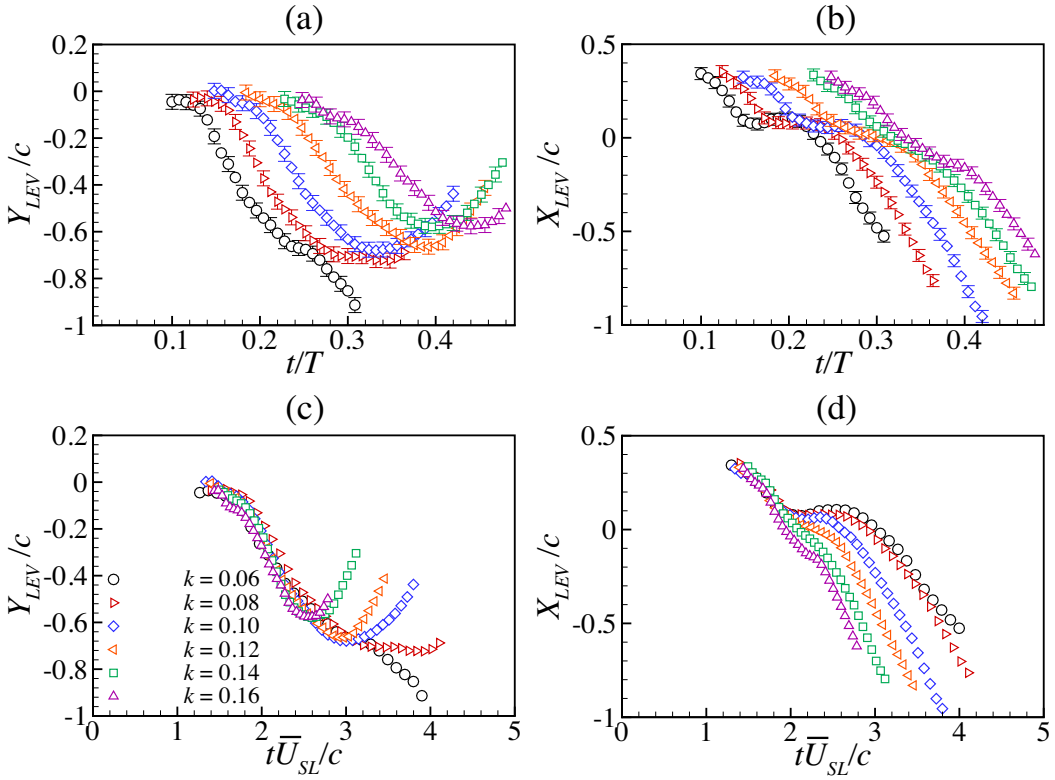

Figure 2.6: (a) LEV normal trajectory versus t/T, (b) LEV axial trajectory versus t/T, (c) LEV normal trajectory versus $t\overline{U}_{SL}/c$ and (d) LEV axial trajectory versus $t\overline{U}_{SL}/c$. For clarity, only every other data point is plotted.

$k \leq 0.10$. For $k \geq 0.12$, however, the LEV does not stop convecting in the streamwise direction, but its rate of advection is slightly reduced. Eventually the rate of LEV chord-wise advection increases again and it approaches a constant value while it is being shed into the wake ($X_{LEV}/c < -0.5$). This is accompanied by a reduction in the rate of chord-normal trajectory, as shown in Fig. 2.6a. In fact, for $k \geq 0.08$, the LEV is shown to move back towards the airfoil surface. Note that this reversed motion of the LEV only occurs once the LEV travels beyond the airfoil mid-chord, $X_{LEV}/c = 0$. Therefore as the airfoil begins to pitch back up in clock-wise direction at $t/T \approx 0.25$, the latter half of the airfoil moves downwards

and hence it gets closer to the LEV. On the other hand for $k = 0.06$, the LEV slows down at $t/T \approx 0.23$ and then moves away quite rapidly again at $t/T \approx 0.26$. We believe this is associated with the fact that at $k = 0.06$, a very large TEV forms relatively early in the cycle, around which the LEV has to travel, thus pushing it away from the airfoil surface. It is possible that the LEV at this reduced frequency eventually moves back towards the airfoil surface after it completely travels around the TEV, but this cannot be confirmed as the field of view is not large enough to capture this process.

In Fig. 2.6c and 2.6d, the chord-normal and chord-wise LEV trajectories of the LEV are plotted versus $t\overline{U}_{SL}/c$. It is shown that the chord-normal LEV trajectories collapse quite well from the inception time up until the reversed motion of LEV. Furthermore, the chord-wise trajectory is shown to collapse only up to $t\overline{U}_{SL}/c \approx 2$. Beyond this time, the trajectory becomes highly dependent on the value of the reduced frequency.

2.3.3 Application of impulse equation to experimental data

Before presenting force results it is necessary to examine the effects of origin location when evaluating the terms. Although the impulse-based force equation is theoretically independent of the origin location ($\mathbf{x}_0$), the presence of errors in the data can be significantly amplified by the origin location. The source of these errors is a result of the pressure removal, in which the local and convective accelerations, as well as the viscous stress are substituted. DeVoria *et al.* (2014) developed a technique that yields the origin location that mitigates the amplified error. This technique utilizes the DMT identity to relate the local and convective accelerations (which are used to remove the pressure term, see DeVoria *et al.* (2014) for a complete discussion) with other terms that contain only the measured velocity. The contribution of the viscous stress is not taken into account in this analysis because its influence on the forces is often negligible (as is shown later). The DMT (which is valid for any vector) is written here for the two vector quantities that are associated with the local and convective accelerations, respectively:

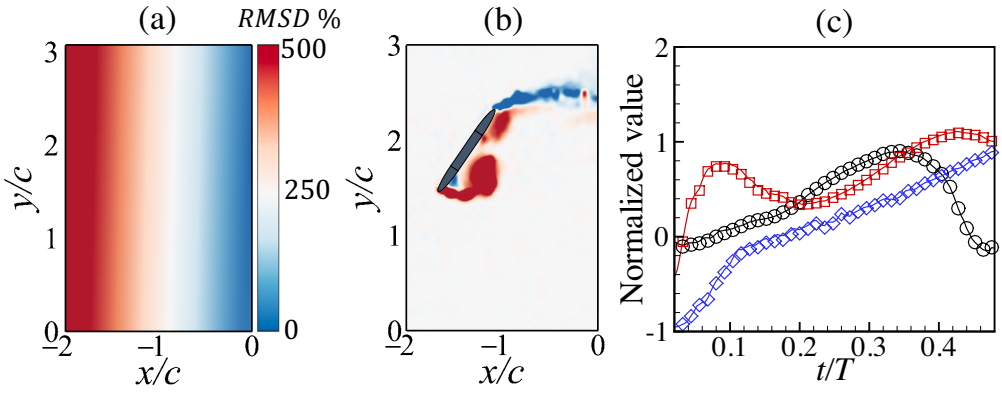

Figure 2.7: (a) Contour of the root mean square deviation between the left- and right-hand side of the sum of Eq. 2.3.4 and 2.3.5, (b) coordinate system and (c) comparison of the sum of the left-hand side (sold lines) with the sum of the right-hand side (symbols) of Eq. 2.3.4 and 2.3.5 using the objectively defined origin. The black, red and blue colors represent $k = 0.06$, 0.10 and 0.14, respectively.

$$(N-1)\int \mathbf{u}dV = \int (\mathbf{x}-\mathbf{x}_0)\times\boldsymbol{\omega}dV - \oint_S (\mathbf{x}-\mathbf{x}_0)\times\mathbf{n}\times\mathbf{u}dS \tag{2.3.4}$$

$$-(N-1)\oint_S \frac{1}{2}(\mathbf{u}\cdot\mathbf{u})\mathbf{n}dS = \oint_S (\mathbf{x}-\mathbf{x}_0)\times\mathbf{n}\times[\mathbf{u}\cdot\nabla\mathbf{u}+\mathbf{u}\times\boldsymbol{\omega}]dS \tag{2.3.5}$$

Note that for the local acceleration condition in Eq. 2.3.4, the velocity time derivative is not used to ensure that the error associated with the temporal discretization does not propagate in defining the origin location. The idea here is to determine the origin location $\mathbf{x}_0$ that best satisfies the left-hand side of both equations (which involve only the measured velocity). Although $S \cup S_B$, the contributions from S_B can be represented by the added mass which is exactly known and thus can be omitted from this evaluation. The objective origin is defined as the one that best satisfies the summation of these equations on a component-wise basis. This is determined as the origin which yields the smallest root mean square deviation (RMSD) over time between the left- and right-hand sides of the summation of Eq. 2.3.4 and 2.3.5. The random velocity errors in the left-hand side leads to negligible

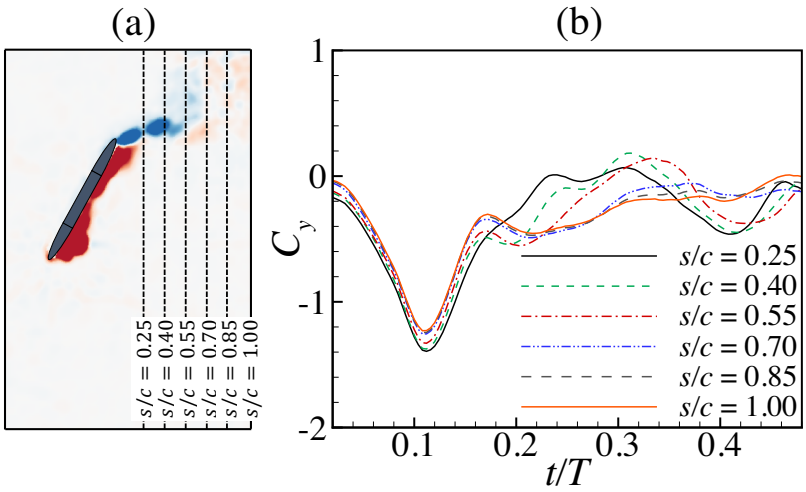

Figure 2.8: (a) A schematic of different control volumes used to test control volume dependence and (b) time-history of the lift force for various control volumes at $k = 0.06$.

error accumulation (DeVoria *et al.*, 2014). In this study the flow is assumed to be two-dimensional and thus N is set to 2. Since we are interested in the lift force, the analysis is conducted for the y component only because the x moment arm plays a much bigger role in the lift production than the y moment arm (Noca, 1997). Equations 2.3.4 and 2.3.5 are non-dimensionlized by $\frac{1}{2}U_\infty^2 Tc$ and $\frac{1}{2}U_\infty^2 c$, respectively. We calculate the RMSD for 3600 origins uniformly distributed over the entire measurement plane. Figure 2.7a shows a contour plot of the RMSD (in percentage of the maximum value of the sum) as a function of the origin location for $k = 0.06$. Figure 2.7b displays the coordinate system that is used. As shown, the RMSD is strongly dependent on the origin of the x-axis, while its dependence on the y-axis is essentially insignificant. It is shown in Fig. 2.7a that the RMSD is minimized at the downstream boundary ($x_0/c = 0$) of the control volume (at this location the RMSD varies from 1.2% of the maximum value to 3.5%, depending on y_0). The contour distribution of the RMSD is found to be essentially identical for all reduced frequencies tested. Figure 2.7c compares the sum of the left-hand

side (solid lines) with the sum of the right-hand side (symbols) of Eq. 2.3.4 and 2.3.5 for $x_0/c = 0$, showing excellent agreement.

In addition, an analysis was conducted to investigate the effects of control volume size on the origin location as well as the calculated transient lift force. Six control volumes were tested, which are shown in Fig. 2.8a. We varied the control volume size by adjusting the distance from the airfoil trailing edge to the downstream boundary (s/c). The largest control volume corresponds to a distance of 1 chord length from the trailing edge to the downstream boundary, whereas the smallest control volume corresponds to a distance of $0.25c$. The cross-stream size of the control volume was found to have a negligible influence on the results. For all control volumes tested, the objective origin was always located at the downstream boundary with RMSD values below 4%. Figure 2.8b demonstrates the effect of control volume size on the calculated lift coefficient ($C_y = 2F_y/\rho U_\infty^2 c$) for $k = 0.06$. The predicted lift coefficient is shown to depend on the control volume size, however the forces begin to converge for $s/c \geq 0.70$. A similar trend is observed for all other reduced frequencies. DeVoria *et al.* (2014) show that the root mean square deviation between the transducer-based measurements and impulse calculation is minimized at approximately $s/c \geq 1$. For the remainder of the paper, we use the largest control volume ($s/c = 1$) to conduct the rest of our analysis.

2.3.4 Reduction of the impulse equation

For convenience, the impulse-based force equation for a two dimensional flow is rewritten:

$$\mathbf{F} = \overbrace{-\frac{1}{N-1}\rho\frac{d}{dt}\int_{V_f}\mathbf{x}\times\boldsymbol{\omega}dV}^{T1} + \overbrace{\oint_S \mathbf{n}\cdot\left(\frac{\rho}{2}u^2\underline{\mathbf{I}}-\rho\mathbf{u}\otimes\mathbf{u}\right)dS}^{T2} + \overbrace{\oint_S \mathbf{n}\cdot\boldsymbol{\lambda}_{\mathbf{imp}}dS}^{T3} + \overbrace{\frac{1}{N-1}\rho\frac{d}{dt}\oint_{S_B}\mathbf{x}\times(\mathbf{n}\times\mathbf{u})dS}^{T4} \quad (2.3.6)$$

As was mentioned previously, the impulse force equation contains complex boundary integral terms that account for the finite control volume. The physical interpretation of these terms is not obvious, and therefore it is difficult to isolate the mechanisms responsible for the lift production. We now show that it is possible to greatly simplify this formulation through the use of the objectively determined origin defined in the previous section.

To calculate the transient lift force, the flow impulse (denoted as $T1$ in Eq. 2.3.6) was fitted to a cubic spline prior to taking the time derivative. The time derivative was calculated using a central difference scheme with $dt = 0.004s$. The results are filtered using an eight-point moving average to remove the high frequency fluctuations related to measurement noise from the force signal. Note that data in the first and last $t/T = 0.01$ of the downstroke are omitted due to unreliable fits. Figure 2.9 shows the total lift coefficient (C_y), as well as the contribution of each individual term of the impulse equation for $k = 0.06$ and 0.14. As shown, the total lift coefficient is dominated by the first two terms, with the first, $T1$, dominant during the first part of the downstroke, and then a combination of $T1$ and $T2$ dominant during the remainder of the downstroke. The third and fourth terms, $T3$ and $T4$, are negligible during the entire cycle. The added mass term ($T4$) is typically negligible for thin airfoils moving in air. The impulse flux force, $T3$, is evaluated on the control volume boundaries, and vortical structures leave

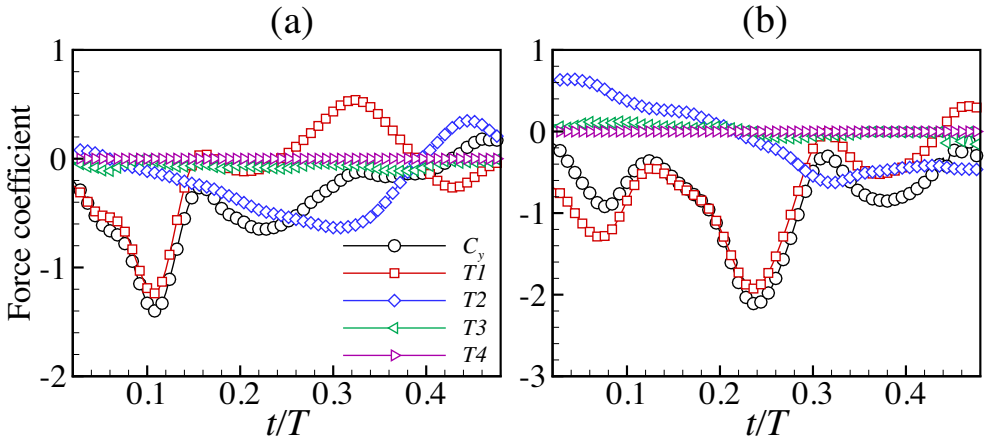

Figure 2.9: Evaluation of the four terms of Eq. 2.3.6 contributing to the lift force in the impulse equation as well as the total lift force for (a) $k = 0.06$ and (b) $k = 0.14$. For clarity, only every other data point is plotted.

the control volume mainly through the downstream boundary. It is apparent that this term is dependent on the streamwise origin location x_0. By choosing an origin located at the downstream boundary, this term becomes negligible (though not exactly zero, because some vortices may leave the upper and lower boundaries of the control volume). These results are consistent with the suggestion by Noca (1997) that the impulse flux force contribution leads to the dilemmic dependence of the impulse force equation on the origin location. By locating the origin at the downstream boundary the contribution of $\mathbf{n}\cdot\mathbf{u}(\mathbf{x}\times\boldsymbol{\omega})$ is significantly reduced. This justification seems to resonate well with the objective origin definition proposed by DeVoria *et al.* (2014).

Based on the above arguments, the force equation can be simplified by retaining $T1$ and $T2$ as follows:

$$\mathbf{F} = -\rho\frac{d}{dt}\int \mathbf{x}\times\boldsymbol{\omega}dA + \rho\oint_S \mathbf{n}\cdot\left(\frac{1}{2}u^2\underline{\mathbf{I}} - \mathbf{u}\otimes\mathbf{u}\right)dS \tag{2.3.7}$$

The first term is the rate of change of impulse, which represents the force pro-

duced by vortical structures within the control volume. This term consists of the contributions of the vortex circulation growth and advection to the transient lift force (Stevens & Babinsky, 2017). Moreover, Saffman (1992) showed that for an impermeable body, the second term on the right-hand side can be written in terms of the Lamb vector such as:

$$\oint_S \mathbf{n} \cdot \Big(\frac{1}{2}u^2\underline{\mathbf{I}} - \mathbf{u} \otimes \mathbf{u}\Big) dS = \int \mathbf{u} \times \boldsymbol{\omega} dA \tag{2.3.8}$$

Note that Saffman (1992) shows that the velocity within a vortex can be written as $\mathbf{u} = \mathbf{u_v} + \mathbf{u_e}$, where $\mathbf{u_v}$ is the velocity induced by the vortex itself (which can be calculated using Bio-Savart law) and $\mathbf{u_e}$ is the external velocity (Kang *et al.*, 2018). The Lamb vector of the self-induced velocity of the vortex, $\int \mathbf{u_v} \times \boldsymbol{\omega} dV$, can be shown to equal zero, meaning that the total vortex force exerted by the vortex on itself is zero. Therefore the only contribution from the Lamb vector is $\int \mathbf{u_e} \times \boldsymbol{\omega} dA$. This can be interpreted as follows. The external velocity, which also includes the induced velocity by other vortical structures either inside or outside of the control volume, interacts with the vorticity of a specific vortex structure (e.g. LEV) within the control volume to produce a force on the airfoil. When the entire vorticity field is contained within the control volume, for example in starting flows, then the vortex force can be shown to equal zero. This suggests that the vortex force term due to vortices outside of the control volume can be thought of as a history effect of the vortex shedding in the far-wake.

Now that the impulse equation has been reduced to terms with clear physical meanings, the mechanisms responsible for the transient lift production can be analyzed. It can be noted that Eq. 2.3.7 is identical to the formulation developed by Kang *et al.* (2018) using the minimum-domain theory.

2.3.5 Transient lift force analysis

The transient lift coefficient is plotted in Fig. 2.10 for low and high reduced frequency ranges, k = 0.06 - 0.10 (Fig. 2.10a) and k = 0.12 - 0.16 (Fig. 2.10b). For

the low reduced frequency range, the lift coefficient is shown to contain two peaks. The magnitude of the secondary peak, which occurs later in the downstroke, is approximately 50% - 55% of the magnitude of the primary peak. The timing of both the primary and secondary peaks is delayed, and their magnitudes increase with increasing reduced frequency. For all reduced frequencies, the lift coefficient approaches positive values (i.e. opposite direction of lift) by the end of the cycle, where the magnitude also increases with increasing reduced frequency. The generation of two lift peaks for heaving and pitching airfoils has been reported in the literature by several researchers (Deng *et al.*, 2014; Karbasian *et al.*, 2016; Totpal *et al.*, 2017). Furthermore, the high reduced frequency cases also show that an additional tertiary lift peak is produced early in the downstroke, whose magnitude relative to the primary peak lift increases with increasing reduced frequency. Similar to the smaller reduced frequency range, the primary and secondary peaks increase in magnitude and are delayed in time as k increases. It is seen that the lift coefficients at high reduced frequencies do not approach positive values at the end of the cycle.

Fig. 2.10c and 2.10d show results using a rescaling of the cycle time that is based on the leading edge velocity as $t\overline{U}_{SL}/c$. Interestingly, the primary force peak force that occurs near $t\overline{U}_{SL}/c \approx 1.75$, is consistent for all reduced frequencies. Also, the value of this convective time scale is slightly after the time at which the LEV is initiated (see Fig. 2.5c). This seems to imply that the roll-up of the leading edge shear layer into an LEV is the dominant mechanism of peak lift production. It also indicates that the leading edge velocity scaling of the time of this peak is explicitly independent of the reduced frequency since this scaling collapses the data over this reduced frequency range. For the lower range of reduced frequencies in Fig. 2.10c the lift coefficient is shown to collapse fairly well up until the local minimum just after the primary peak is produced. For time $t\overline{U}_{SL}/c > 3.7$ the lift coefficients begin to diverge. This corresponds to the time at which the trailing edge shear layer begins to roll-up into a TEV. The results for the larger range of reduced frequencies in Fig. 2.10d show somewhat different trends. For these cases

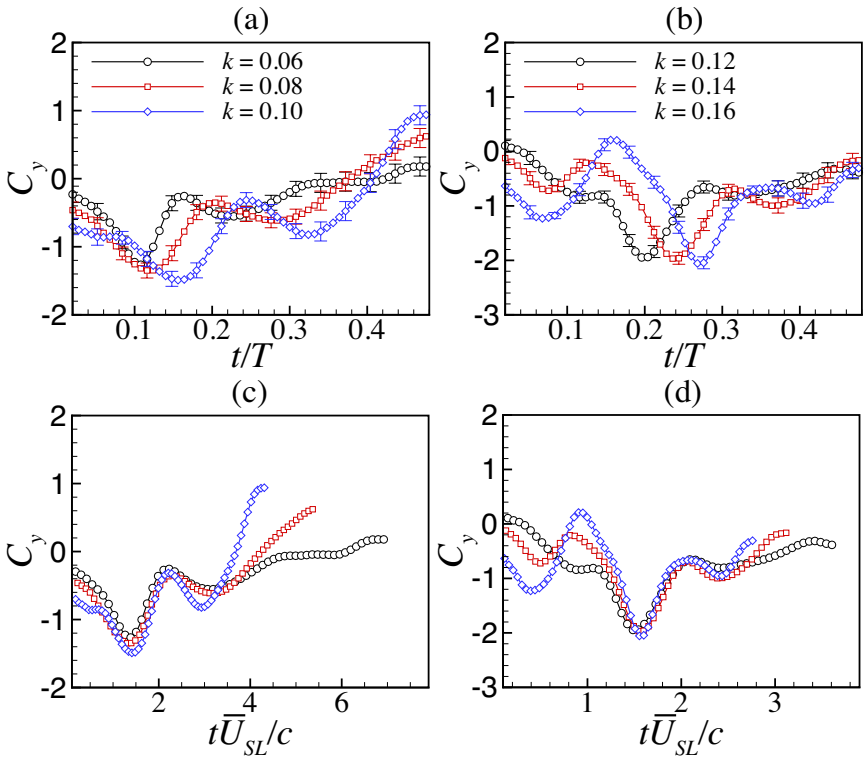

Figure 2.10: Transient lift coefficient versus t/T for (a) k = 0.06-0.10 and (b) k = 0.12-0.16. Transient lift coefficient versus $t\overline{U}_{SL}/c$ for (c) k = 0.06-0.10 and (d) k = 0.12-16.

the TEV does not form and hence the lift coefficients do not significantly diverge at later times during the cycle. Also, for the larger reduced frequencies, the influence of the lagging LEV from the previous cycle near the top heaving position results in a third minor peak at early times in the cycle. The strength of this minor peak increases with increases reduced frequency while occurring earlier at the start of the downstroke. In fact, it is only this early cycle minor peak that distinguishes the effect of increasing reduced frequencies for the high k values.

To better understand the role of vortical structure, in particular the LEV and TEV, in lift force production, it is necessary to synchronize the lift force with the

flow field. Rather than using the vorticity field alone, we use the local integrand of the impulse and vortex forces of Eq. 2.3.7. For the vortex force, the lamb vector is used instead of the flux formulation to visualize its local contribution within the control volume.

Figure 2.11 shows the total lift coefficient (C_y) for $k = 0.06$, as well as the contributions of the impulse ($C_{y,I}$) and vortex ($C_{y,V}$) forces. In addition, contours of vorticity and the integrand of impulse ($F_{y,I}$) and Lamb forces ($F_{y,L}$) for five snapshots during the downstroke motion are provided. Both force integrands are normalized by $2c/\rho U_\infty^2$. In snapshot (1), the LEV had just been formed, and it remains compact and quite close to the airfoil surface. The impulse force contour plot shows that the LEV is primarily producing a negative impulse (in the direction of lift). The total lift here is dominated by the LEV impulse force. While the LEV is shown to produce a vortex force, its contribution is approximately cancelled by the vortex force produced by the trailing edge shear layer, hence $C_{y,V} \approx 0$. Going to snapshot (2), the total lift is shown to drop from $C_y \approx -1.2$ to $C_y \approx -0.5$. This reduction is a consequence of the LEV lifting away from the airfoil surface. As this happens, the LEV begins to produce a positive impulse force (lift-diminishing) that approximately cancels the negative impulse contribution (lift-enhancing), such that $C_{y,I} \approx 0$. Additionally, the LEV is also shown to produce a positive vortex force (lift-diminishing), however, the lift-enhancing effect clearly dominates. The total lift force at this snapshot is primarily due to the vortex force of the LEV.

The fact that the LEV produces lift-enhancing as well as lift-diminishing impulse and vortex forces is quite interesting. Contrary to the conventional belief that LEVs on the suction side only provide lift-enhancing contributions, it is necessary to stress that there is no vortical structure that provides a purely single-sign contribution to the aerodynamic forces. Wu *et al.* (2007*a*) have observed a similar phenomena for drag force analysis for a flow past a cylinder. They explained that this observation is consistent with the fact that attached flows over an airfoil produce boundary layers at the upper and lower surfaces of the airfoil, but only the sum of the total vorticity in the boundary layer (i.e. net circulation) yields the de-

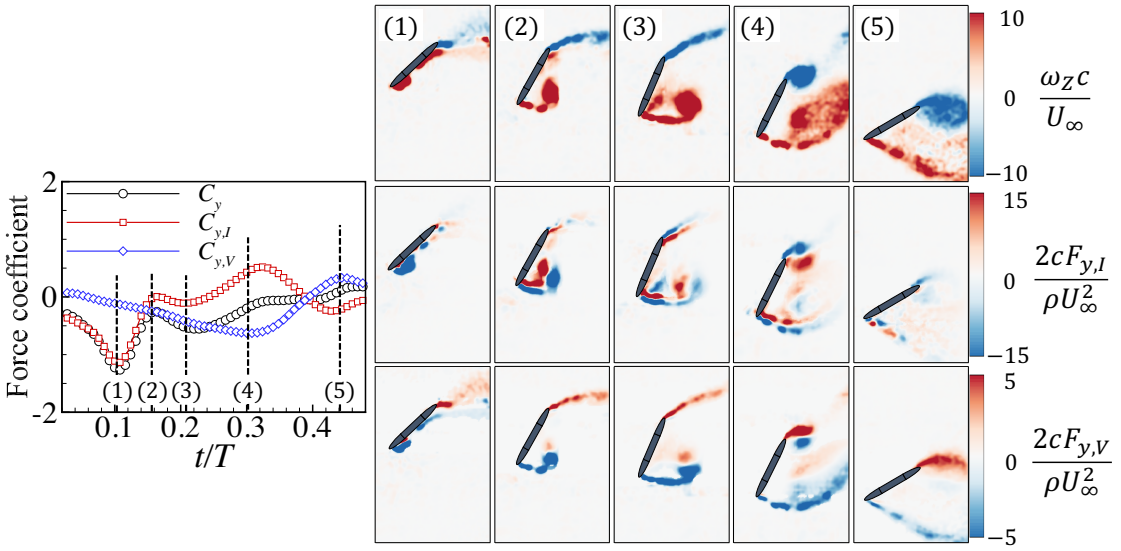

Figure 2.11: Synchronization of the transient lift force with the vorticity field and the local contours of the impulse and vortex forces for $k = 0.06$.

sired lift. Furthermore, an alternative explanation of the significant lift reduction at (2) can be understood by decomposing the force impulse into circulation growth and chord-wise trajectory of the LEV. At this instant in time ($t/T \approx 0.16$), the rate of change of LEV circulation significantly decreases (Fig. 2.5a) and the LEV chord-wise advection approaches zero (Fig. 2.6b). Consequently, the LEV impulse force contribution is greatly decreased. The magnitude of the secondary lift peak in (3) is also shown to be dominated almost entirely by the vortex force produced by the LEV and its shear layer. The formation of the peak itself, however, is a result of the impulse force becoming less negative and ultimately going positive near $t/T \approx 0.25$. This is equivalent to the convective time scale of $tU_{SL}/c \approx 3.7$, at which the TEV begins to form. In snapshot (4), the total lift force is shown to drop to very small values. The LEV here has attained its maximum circulation (see Fig. 2.5a at $t/T \approx 0.30$), and thus no longer contributes to the force impulse. In addition, its advection relative to the TEV is also expected to significantly drop as it approaches the trailing edge of the airfoil (Stevens & Babinsky,

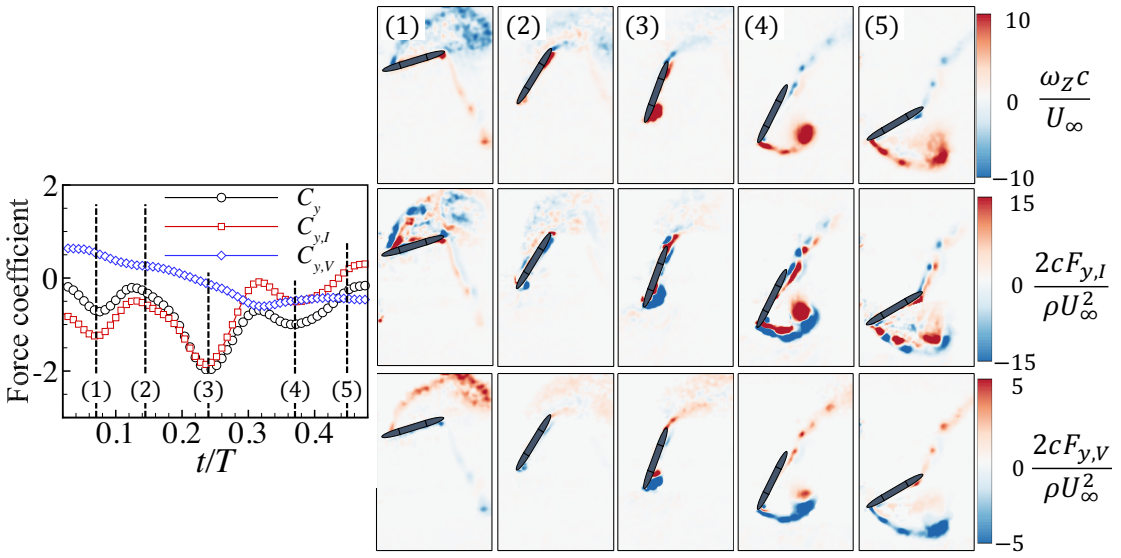

Figure 2.12: Synchronization of the transient lift force with the vorticity field and the local contours of the impulse and vortex forces for $k = 0.14$.

2017). Meanwhile, the rolled-up TEV begins to generate a net positive impulse force (i.e. lift-diminishing), which almost cancels with the vortex force produced by the leading edge shear layer and TEV. Beyond snapshot (4), the LEV begins to convect outside of the control volume, which is reflected by the impulse force going from positive to negative values at snapshot (5). This is accompanied by the change of the sign of the vortex force from positive to negative. At snapshot (5) and beyond, the TEV begins to leave the control volume, and the impulse force decays from negative values to zero, whereas the Lamb force decays from positive values to zero, hence they cancel each other to result in $C_y \approx 0$ by the end of the downstroke. This equal and opposite trend of the Lamb and impulse forces indicates that the Lamb vector is indeed picking up the contribution of the LEV and TEV as they leave the control volume.

As the reduced frequency is increased to $k = 0.14$, the third lift peak is formed early in the cycle, as shown in snapshot (1) for $k = 0.14$ in Fig. 2.12. The negative LEV generated from the previous upstroke is shown to be captured by the airfoil as

it begins heaving/pitching downward. The majority of the impulse force is shown to be sporadically distributed within the separated flow on the upper surface of the airfoil. It should be kept in mind that $F_{y,I}$ is calculated locally and therefore the noise level due to spatial and temporal derivatives may be high. However the integrated value ($C_{y,I}$) clearly dominates the total lift production. Furthermore, the small positive vortex force at this instant is shown to be dominated by the upper-surface shear layer. In snapshot (2), this lift-enhancing effect has subsided and the upper shear layer begins to re-attach to the airfoil surface. The lift here is dominated by the impulse force from the nearly-attached boundary layer. However we anticipate that the accuracy of the force calculation here to be somewhat hindered by the fact that the PIV measurements do not fully resolve the surface vorticity. The mechanisms responsible for the production of lift peaks in snapshots (3) and (4) are identical to the mechanisms identified for the lower reduced frequency values. A notable difference for this large reduced frequency case is the lack of TEV formation. As explained in the previous section, the LEV approaches the trailing edge of the airfoil quite late in the downstroke, where the angle of attack is not large enough to support the roll-up of the trailing edge shear layer into a TEV. Consequently, the lift-diminishing effect of the TEV is avoided.

To conclude the above discussion, the lift-enhancing mechanisms for the low reduced frequency range ($k = 0.06 - 0.10$) are all related to the LEV generation, its growth and its trajectory relative to the airfoil surface. As the reduced frequency is increased to $k = 0.12 - 0.16$, the slower convective time scale of the vortical structures allows the airfoil to capture the influence of the previously shed LEV, whereas the lift-diminishing effect of the TEV is avoided. It is interesting to note the optimal vortex formation generated for the low frequency cases does not correlate with the peak lift. This contradicts the findings of Milano & Gharib (2005), who show that the peak lift force is produced when the LEV formation number reaches approximately 4. However, their results are for a flapping wing (pitching) while translating (not heaving) which does not have the same effect on the trajectory of the leading edge vortex motion relative to the surface. We

believe that this discrepancy of lift force versus formation number is related to the fact that the LEV generated in our experiments begins to lift-off from the airfoil surface much before the optimal formation number is achieved. Therefore the correlation between the optimal vortex formation number and maximum lift production is not only dependent on the LEV size and strength, but also on the LEV trajectory relative to the airfoil. At larger values of k our results show that an optimal formation number is never reached due to the disconnection of the feeding shear layer from the leading edge vortex. For energy harvesting applications where it is important to correlate peak force with peak heaving velocity during the cycle, the delayed leading edge vortex formation associated with higher k values improves power production even though the peak formation numbers are lower. Lastly, for all reduced frequencies, the impulse force produces the general trend of the transient lift, whereas the vortex force simply modifies the lift magnitude. The implication of this is that unlike impulsively moving airfoils where the entire circulatory force is dominated by the impulse force (Stevens & Babinsky, 2017), the contribution of the vortex force must be taken into consideration when constructing low-order lift models of continuously oscillating airfoils.

2.4 Conclusions

Two dimensional particle image velocimetry experiments were conducted to investigate the vortex dynamics and lift force production mechanisms of an oscillating airfoil undergoing dynamics stall. The reduced frequency was varied from $k = 0.06$ to $k = 0.16$, which covers the range associated with high efficiency energy harvesting. The lift force was estimated from the velocity fields and its derivatives using the derivative moment transformation-based impulse force formulation. Additionally, the leading edge vortex strength, size and trajectory were calculated to further investigate their influence on the lift force production.

The moment-arm dilemma associated with the application of the force impulse equation to experimental data was also investigated. It is shown that the origin location that most effectively reduces the amplified error due to the position vector

was always located at the downstream boundary of the control volume. In addition, it was found that the calculated lift forces were consistent when the distance from the airfoil trailing edge to the downstream boundary was greater than $0.85c$. Upon using the objectively defined origin, the impulse force equation was reduced to two dominating terms: the rate of change of the impulse within the control volume and the Lamb vector thereof that picks up the contribution of vortices outside of the control volume.

For $k = 0.06-0.10$, the lift force results show that there are two force peaks that form during the downstroke/upstroke. The primary peak is associated with the formation of the leading edge vortex and the secondary peak is associated with its enhanced time rate of circulation growth and chord-wise advection. Even though the optimal leading edge vortex formation number was attained for these lower reduced frequencies, it was observed that its timing was not well correlated with the timing of maximum lift force. In addition, at this low reduced frequency range, the trailing vortex sheet was observed to roll-up into a trailing edge vortex. The trailing edge vortex was shown to produce lift-diminishing effects, whose intensity increases with increasing reduced frequency. For $k = 0.12 - 0.16$, a third lift peak was shown to form at the beginning of the downstroke due to a vortex capture-like effect from the LEV shed during the previous upstroke. No trailing edge vortex formation was observed at these high reduced frequencies, hence the lift-diminishing effect is avoided.

The results of this study may be of great importance in developing low-order models of transient lift forces produced by oscillating airfoils undergoing dynamic stall. In particular, the overall trend of the lift force was shown to be primarily dependent on the impulse force produced by vortical structures (leading and trailing edge vortices and their associated shear layers) within the control volume. However, the Lamb force, which indirectly captures the influence of the far-field vortical structures may significantly alter the magnitude of lift. The implication of this is that the influence of vortical structures in the far-field must also be considered when constructing low-order models.

Acknowledgments

The authors would like to thank Dr. Ali Mousavian and Cameron Planck for helping with designing the heaving/pitching device and developing the LabView code. Firas Siala acknowledges the financial support from Link Energy Foundation Fellowship. Financial support was provided through the National Science Foundation, Award number 1804964. Also, financial support was provided through the Air Force Office of Scientific Research under the MURI grant FA9550-07-1-0540.

Chapter 3 Power estimation of flapping foil energy harvesters using vortex impulse theory

Firas F. Siala and James A. Liburdy

Renewable Energy
Under Review
Elsevier, Amsterdam, Netherlands

Abstract

This study explores the feasibility of using the vortex impulse approach, based on experimentally generated velocity fields to estimate the energy harvesting performance of a sinusoidally flapping foil. Phase-resolved, two-component particle image velocimetry measurements are conducted in a low-speed wind tunnel to capture the flow field surrounding the flapping foil at reduced frequencies of $k = fc/U_\infty$ = 0.06 - 0.16, pitching amplitude of $\theta_0 = 75°$ and heaving amplitude of $h_0/c = 0.6$. The model results show that for the conditions tested, a maximum energy harvesting efficiency of 25% is attained near $k = 0.14$, agreeing very well with published numerical and experimental results in both accuracy and general trend. The vortex impulse method identifies key contributions to the transient power production from both linear and angular momentum effects. The efficiency reduction at larger values of reduced frequencies is shown to be a result of the reduced power output from the angular momentum. Further, the impulse formulation is decomposed into contributions from positive and negative vorticity in the flow and is used to better understand the fluid dynamic mechanisms responsible for producing a peak in energy harvesting performance at $k = 0.14$. At the larger k values, there is a reduction of the advective time scales of the leading edge vortex (LEV) formation. Consequently, the LEV that is shed during the previous half cycle interacts with the foil at the current half cycle resulting in a large negative pitching power due to the reversed direction of the kinematic motion. This vortex capture process significantly decreases the total cycle averaged power output and energy harvesting efficiency. These results show the link between the kinematic motion and LEV time scales that affect the overall power production.

3.1 Introduction

The rising global trend to reduce dependence on fossil fuels has provided significant motivation toward the development of alternative energy conversion methods

and new technologies to improve their efficiency. Recently, flapping foil energy harvesters have been gaining a wider scope of attention as a means of extracting energy from streams, rivers, tidal flows and wind (Xiao & Zhu, 2014). These devices offer important advantages to the conventional rotary turbines from efficiency, economic and environmental perspectives (Young *et al.*, 2014). For example, these systems can use significantly lower free stream velocities, allowing for a wider range of available resource sites at both large and small scales. Their operation can mitigate the occurrence of centrifugal stresses on the foil resulting in less structural constraints, as well as having reduced noise output and animal interactions Zhu (2011).

The concept of flow energy harvesting using flapping foils was proposed by McKinney & DeLaurier (1981). The motion kinematics of the flapping foil, which is typically modeled as combined sinusoidal heaving and pitching motion at very large angles of attack, results in flow separation and formation of the leading edge vortices (LEVs). LEV structures produce regions of low-pressure on the suction side of the foil and generate a large suction force as long as they remain attached to the foil surface (Polhamus, 1971). It is widely acknowledged that the LEV provides a mechanism for the high energy harvesting capabilities of flapping foils (Xiao & Zhu, 2014). This is in contrast to the traditional wind/hydro-turbines, where the flow must remain attached to the foil surface to achieve high energy harvesting efficiency levels.

The vast majority of published studies on flapping foil energy harvesters have utilized numerical simulations to perform parametric investigations and to optimize the overall performance (Dumas & Kinsey, 2006; Kinsey & Dumas, 2008; Peng & Zhu, 2009; Zhu, 2011). The instantaneous power extracted by the flapping foil from fluid flow is defined as follows:

$$P = F_y \dot{h} + M\dot{\theta} \tag{3.1.1}$$

where F_y is the force in the direction of heaving motion, $\dot{h}$ is the heaving velocity, M is the pitching moment and $\dot{\theta}$ is the pitching velocity. It has been shown that

the rate of energy harvesting is maximized when operating at reduced frequencies of $k = fc/U_\infty = 0.10 - 0.15$ (where f is oscillation frequency, c is foil chord length and U_∞ is free stream velocity), heaving amplitudes of $h_0/c = 0.5 - 1.0$, pitching amplitudes of $\theta_0 = 70^\circ - 90^\circ$ and a phase shift of 90° between the heaving and pitching motions (Kinsey & Dumas, 2008; Zhu, 2011; Kim *et al.*, 2017). Currently, the majority of research studies on flapping energy harvesters are concerned with developing mechanisms to further enhance energy extraction capacity. Such mechanisms include the use of non-sinusoidal motion and structural flexibility of the foil (Xiao *et al.*, 2012; Liu *et al.*, 2013; Lu *et al.*, 2014; Siala & Liburdy, 2015). These mechanisms, as well as others, attempt to control the LEV evolution to enhance the forces and their timing during the flapping cycle. Major contributions to understanding the complexities of LEVs have come from animal and insect flight (Leishman, 1994; Ellington *et al.*, 1996; Madangopal *et al.*, 2005; Platzer *et al.*, 2008). However, energy harvesting typically occurs at relatively low reduced frequencies, where there is a dearth of knowledge concerning LEV evolution and mechanisms responsible for establishing the LEV time scales to compliment the much slower relative oscillation time scales of energy harvesting. Of particular interest is application of the optimal vortex formation by Gharib *et al.* (1998). Dabiri (2009) has shown that there exists a strong correlation between the optimal vortex formation and thrust produced by swimming animals through vortex propulsion. However, it remains unknown whether this correlation also applies to LEV formation and energy harvesting efficiency of flapping foils. In addition to LEVs, operating at such low reduced frequencies may also trigger the formation of other large-scale flow structures such as trailing edge vortices (TEVs) (Siala *et al.*, 2017). To design more effective mechanisms of energy harvesting enhancement, there is a need to investigate the relationship between the dynamics of flow structures and power production in greater depth.

The relationship between flow structures and power production is typically studied qualitatively, where the vorticity field is synchronized with the instantaneous fluid dynamic force and moment (Xie *et al.*, 2014; Kim *et al.*, 2017). The

disadvantage of this method is that it does not allow one to quantify the effects of different flow structures on the total force. In addition, it is often not feasible to experimentally measure the fluid dynamic forces accurately due to challenges in separating the inertial contributions from the total measured force (Rival *et al.*, 2009). This is especially a problem in wind tunnel experiments, where the foil density can be orders of magnitude greater than the density of air. As a result, wind tunnel experiments have been focused on very low reduced frequencies in order to minimize the inertial effects (Totpal *et al.*, 2018). Recently, many authors began using the concept of vortex impulse to estimate the fluid dynamic forces from the measured velocity field (Lin & Rockwell, 1996; Kim *et al.*, 2013; Li & Wu, 2015; Kang *et al.*, 2018; Siala *et al.*, 2018). Originally, this concept was introduced to bypass the integration of total momentum in infinite regions (Lighthill, 1986*a*; Saffman, 1992; Batchelor, 2000). Estimating the fluid dynamic forces using the vortex impulse technique offers several advantages. For example, it only requires the knowledge of the velocity field, where the evaluation of pressure field is not required. This makes it a very attractive tool for the experimental fluid dynamics community since inferring the pressure field from velocity data is often a non-trivial task. In addition, since the impulse equation is linearly dependent on vorticity, it is possible to quantify the contribution of different vortex structures to the total force, which is quite advantageous when, for example, the goal is to design mechanisms that enhance the LEV contribution to force generation and power output.

The objectives of this paper are: (i) to explore the feasibility of using experimentally generated velocity fields to estimate the energy harvesting performance and (ii) to better elucidate the mechanisms of power production of flapping foils. Two-component PIV measurements are conducted to capture the flow field surrounding the flapping foil. The aerodynamic loads and moment are determined using the finite-domain impulse theory (Noca *et al.*, 1999). While the impulse theory has been used extensively in estimating the lift and drag forces, to the best of our knowledge, its application for estimating the pitching moment has not been

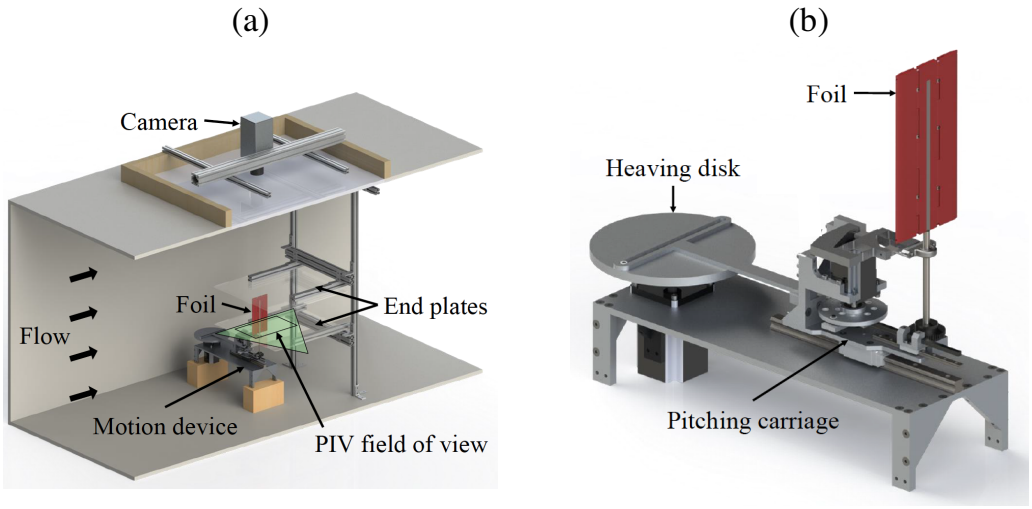

Figure 3.1: (a) Drawing of the experimental setup illustrating the wind tunnel, motion device and PIV system and (b) zoomed-in view of the motion device. Figures are adopted from Totpal (2017).

reported in the literature.

The rest of the paper is organized as follows. In Section 3.2, the details of experimental methodology are presented. In Section 3.3, the techniques of data analysis are provided. Section 3.4 presents results of force and moment analysis and power production. Finally, conclusions and implications of this work are provided in Section 3.5.

3.2 Methodology

The experimental setup in the wind tunnel and a zoomed-in view of the motion device are sketched in Fig. 3.1. The foil was fabricated using fused deposition modeling, and has a chord length, thickness and aspect ratio of 125 mm, 6.25 mm and 2, respectively. The foil is attached to the motion device using a titanium rod spanning through the mid-chord of the foil. The motion device is used to generate

the heaving and pitching motion according to the following equations:

$$h(t) = h_0 cos(2\pi ft) \tag{3.2.1}$$

$$\theta(t) = \theta_0 cos(2\pi ft + \Phi) \tag{3.2.2}$$

where h_0 is the heaving amplitude, θ_0 is the pitching amplitude, Φ is phase shift between heaving and pitching and t is time. In this study, the heaving amplitude, pitching amplitude and phase shift are fixed at $h_0/c = 0.6$, $\theta_0 = 75°$ and $\Phi = 90°$, respectively, whereas the reduced frequency, k, was varied from 0.06 to 0.16 in increments of 0.02. A sketch of the foil motion is shown in Fig. 3.2a. Furthermore, the motion kinematics can be integrated into the effective angle of attack, which is typically defined as follows:

$$\alpha_e = \theta(t) - arctan\left(\frac{\dot{h}(t)}{U_\infty}\right) \tag{3.2.3}$$

The effective angle of attack for one cycle is plotted in Fig. 3.2b for $k = 0.06 - 0.16$.

Phase-resolved particle image velocimetry measurements were conducted at the mid-span with a vector resolution of 1.8 mm (approximately 70 vectors per chord length). End plates were used to mitigate the three-dimensional effects. The phase-averaged velocity fields were obtained by averaging one hundred images at each phase of interest. A total of 116 phases during the downstroke motion with an equal spacing of $\Delta t/T = 0.004$ were acquired. To capture the entire flow field surrounding the oscillating foil, the experiments were repeated at a phase delay of 180° for each of the 116 phases. The 180° out of phase flow fields were then mirrored and stitched to the rest of the vector field to construct the full flow field surrounding the foil, as shown in the previous chapter. Uncertainty analysis based on the statistical-correlation technique developed by Wieneke (2015) yielded an average uncertainty of 1.3% and 2.1% of the local stream-wise and cross-stream velocity component, respectively.

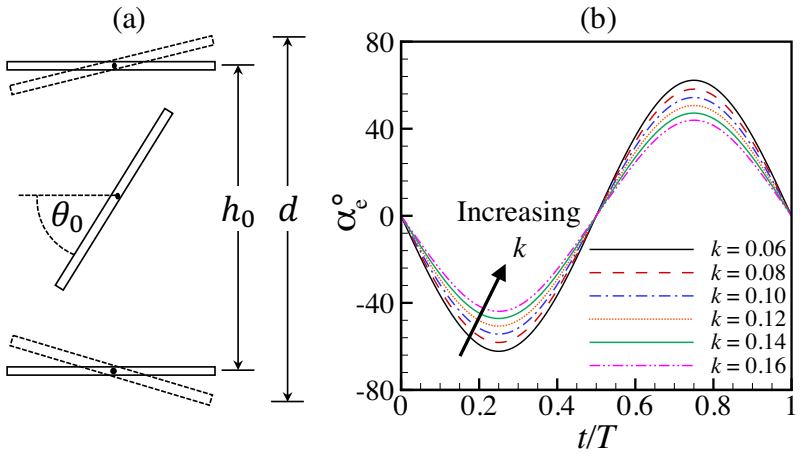

Figure 3.2: (a) Heaving and pitching motion. The foil pitching center is located at $c/2$ and d is the total crossflow distance swept by the foil. (b) Effective angle attack versus time for k = 0.06-0.16

3.3 Data analysis

The total cycle-averaged power coefficient is divided into two components, the power from heaving motion $\overline{C}_{P,h}$ and the power from pitching motion $\overline{C}_{P,\theta}$:

$$\overline{C_P} = \overline{C}_{P,h} + \overline{C}_{P,\theta} \tag{3.3.1}$$

where the cycle-averaged heaving and pitching power coefficients are defined as follows:

$$\overline{C}_{P,h} = \frac{2\overline{F_y \dot{h}}}{\rho U_\infty^3 c} \tag{3.3.2}$$

$$\overline{C}_{P,\theta} = \frac{2\overline{M_z \dot{\theta}}}{\rho U_\infty^3 c} \tag{3.3.3}$$

Furthermore, we define the energy harvesting efficiency, η, as the ratio of power output to the available fluid power in the swept area of the two dimensional foil. Similar to the power coefficient, the total efficiency is decomposed into heaving

and pitching components such as follows:

$$\eta_h = \overline{C}_{P,h}\frac{c}{d} \tag{3.3.4}$$

$$\eta_\theta = \overline{C}_{P,\theta}\frac{c}{d} \tag{3.3.5}$$

where d is the total crossflow length swept by the foil.

The two-dimensional impulse-based aerodynamic force (Noca *et al.*, 1999) can be written as follows:

$$\mathbf{F} = -\rho\frac{d}{dt}\int_A \mathbf{x}\times\boldsymbol{\omega}dA + \rho\int \mathbf{u}\times\boldsymbol{\omega}dA - \rho\oint_S \mathbf{n}\cdot\Big([\mathbf{u}(\mathbf{x}\times\boldsymbol{\omega})]\Big)dS + \oint_S[\mathbf{x}\cdot(\nabla\cdot\mathbf{T})\mathbf{I} - \mathbf{x}(\nabla\cdot\mathbf{T})]dS + \mathbf{F}_{AM} \tag{3.3.6}$$

where $\mathbf{x}$ is the position vector, $\boldsymbol{\omega}$ is the vorticity vector, $\mathbf{u}$ is the velocity vector, $\mathbf{T}$ is the stress tensor, $\mathbf{I}$ is the identity tensor and $\mathbf{n}$ is the normal vector. The first term is integrated over the fluidic area A that is bounded by the control volume surface S and the foil surface, where as the second, third and fourth terms are integrated over the control volume surface S. Although the equation above is theoretically independent of the origin location $\mathbf{x}_0$, Siala & Liburdy (2019*a*) have shown that by choosing an origin located on the downstream boundary of the control volume, the surface integrals can be shown to have negligible contributions, and the two-dimensional force equation can be written as follows:

$$\mathbf{F} = -\rho\frac{d}{dt}\int \mathbf{x}\times\boldsymbol{\omega}dA + \rho\int \mathbf{u}\times\boldsymbol{\omega}dA + \mathbf{F}_{AM} \tag{3.3.7}$$

The advantage of this simplified equation is that it contains only three terms with clear physical meaning. The first term on the right-hand side is referred to as the impulse force and it is associated with the growth and advection of vortical structures in the control volume (Stevens & Babinsky, 2017). The second term on the right-hand side is referred to as the vortex force, which represents the effect

of vortex structures outside of the control volume on the total force (Kang *et al.*, 2018; Siala & Liburdy, 2019*a*). The term F_{AM} is the added-mass force, which represents the force felt by the oscillating foil as it pushes against the adjacent fluid. For thin foils submerged in air, the added-mass force is negligible.

The aerodynamic moment equation can be shown to be written as follows:

$$\mathbf{M} = \rho\frac{1}{2}\frac{d}{dt}\int x^2\boldsymbol{\omega}dA + \rho\int \mathbf{x}\times(\mathbf{u}\times\boldsymbol{\omega})dA - \rho\frac{1}{2}\oint x^2\mathbf{n}\times(\mathbf{u}\times\boldsymbol{\omega})dS \tag{3.3.8}$$

where we refer to the first and second terms on the right-hand side as the impulse moment and vortex moment, respectively. The third term on the right-hand side takes into account the contributions of flow structures passing through the boundary (S) of the control volume. Since we are interested in estimating the moment about the pitching axis of the airfoil, the origin location for the moment equation was set at the pitching axis (mid-chord). The errors from the velocity fields were propagated to the force and moment in order to calculate their uncertainty, which were estimated to be 13.6% and 16.2% of their maximum values, respectively.

One important advantage of the impulse-based force and moment equations is that they are linearly dependent on vorticity, meaning that total force and moment impulse can be treated as a superposition of impulses of every individual vortex structure in the flow. For simplicity, in this study we categorize two different vortical structures: one with positive sign vorticity, and the other with negative sign vorticity. We define the heaving power coefficient of the positive vortical structures noted with "+" as:

$$C_{P,h^+} = \frac{2F_{y^+}\dot{h}}{\rho U_\infty^3 c} \tag{3.3.9}$$

$$C_{P,\theta^+} = \frac{2M_{z^+}\dot{h}}{\rho U_\infty^3 c} \tag{3.3.10}$$

Similarly, the pitching power coefficient of the negative vortical structures noted

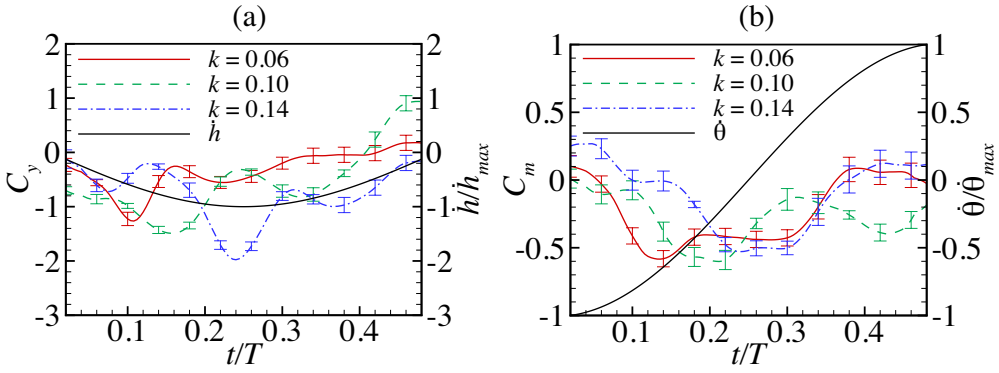

Figure 3.3: (a) Coefficient of force and heaving velocity and (b) coefficient of moment and pitching velocity, for $k = 0.6$, 0.10 and 0.14.

with "-" as:

$$C_{P,h^-} = \frac{2F_{y^-}\dot{h}}{\rho U_\infty^3 c} \tag{3.3.11}$$

$$C_{P,\theta^-} = \frac{2M_{z^-}\dot{h}}{\rho U_\infty^3 c} \tag{3.3.12}$$

Upon analyzing the power production using the above decomposition, one can correlate the vorticity dynamics with the performance more effectively.

3.4 Results

The results of this study determine the overall power production performance based on both efficiency and power coefficient. Experimentally measured velocity fields are used to evaluate the unsteady aerodynamic force and moment during the cycle with results given here for the downstroke motion. The upstroke motion results are a repetition of the downstroke with associated sign reversal. Velocity data are used to identify the dominant flow structures as they relate to the power production.

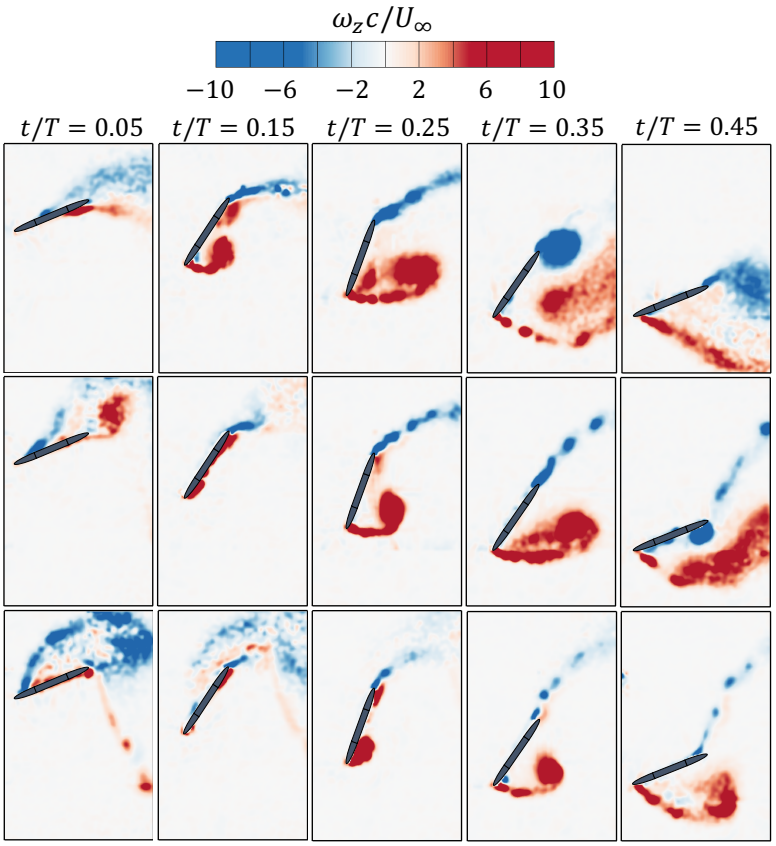

Figure 3.4: Phase-averaged vorticity field for discrete phases during the downstroke. Top row: $k = 0.06$, middle row: $k = 0.10$ and bottom row: $k = 0.14$.

3.4.1 Force and moment estimation

The transient force ($C_y = 2F_y/\rho U_\infty^2 c$) and moment ($C_m = 2M_z/\rho U_\infty^2 c^2$) coefficients are plotted in Fig. 3.3a and 3.3b, respectively, for $k = 0.06$, 0.10 and 0.14. The heaving and pitching velocities are also included. The force coefficient experiences an initial dominant peak followed by a secondary peak. Note that for $k = 0.14$, there is also a preliminary smaller peak that occurs early in the cycle at $t/T \approx 0.05$. The timing of the dominant peak events is shown to delay to later times in the cycle as the reduced frequency increases. Also, increasing the reduced frequency

increases the magnitude of this peak force. In contrast, increasing the reduced frequency has minimal influence on the magnitude of the peak moment coefficient, but it does delay the occurrence of the peak to later times in the cycle. The phase shift of the force and moment coefficients can be understood by analyzing the spatio-temporal evolution of vortical structures in the flow.

In Fig. 3.4, we show the evolution of the phase-averaged vorticity and velocity fields for $k = 0.06$, 0.10 and 0.14. The flow approaches from the left and the non-dimensional time $t/T = 0$ corresponds to the top heaving position. It is quite obvious that the inception of the LEV is delayed when the reduced frequency increases. This is associated with the decrease in the foil oscillation time scale relative to the flow time scale. As a result, the shear layer requires a longer time to react to the change in the geometric angle of attack as k increases, thereby delaying separation. The timing of peak force generation coincides with the time at which the LEV is lifted-off the foil surface, whereas the peak moment occurs slightly later. The peak moment has negative values, indicating that when the LEV forms on the bottom surface of the foil, it creates a downward force on upstream portion of the foil. This induces a counter-clockwise moment about the pitching axis (mid-chord). The magnitude of moment coefficient begins to decrease once the LEV advects downstream beyond the foil center. Subsequently, the trailing edge shear layer rolls-up into a TEV when the LEV approaches the foil trailing edge when $k = 0.06$ and 0.10. For $k = 0.06$, the formation of the TEV ($t/T \approx 0.25$) results in only a slight decrease in the force coefficient, whereas its influence on the moment coefficient is negligible. This is because the TEV advects downstream into the wake shortly after it forms, such that its influence on the foil is not significant. On the other hand for $k = 0.1$, the TEV is shown to completely roll on the bottom surface of the foil by the end of the downstroke motion. Consequently, its influence on the foil is more profound, which is reflected by the rapid decrease in the force and increase in counter-clock wise moment at $t/T \approx 0.4$.

By increasing the reduced frequency to $k = 0.14$, the advective time scale of the flow becomes even larger relative to the oscillation time scale. This results in

the LEV that is shed during the previous upstroke to remain near the foil trailing edge as the foil begins its downward motion ($t/T \approx 0.05$). The foil takes advantage of the proximity of this LEV to produce an early small downward force peak, as is shown in Fig. 3.3a. In addition, as the newly formed LEV approaches the foil trailing edge at $t/T = 0.45$, it is observed that the trailing edge vortex sheet does not roll-up into a large TEV. This is because the LEV approaches the trailing edge rather late in the cycle when the geometric angle of attack is relatively small. As a consequence, the trailing edge shear layer does not roll into a large vortex.

3.4.2 Power output

The total instantaneous power coefficient is shown in Fig. 3.5, along with the heaving and pitching contributions for $k = 0.06$, 0.10 and 0.14. For $k = 0.06$, the total power coefficient (C_P) has three distinct peaks. The first peak is produced at $t/T \approx 0.12$, where both the heaving and pitching motions have a comparable contribution. At this instant, the LEV has just lifted-off the surface of the foil, which results in peak force and moment coefficients as shown in Fig. 3.3. The peak force and moment coefficients both have the same sign as the heaving and pitching velocities, respectively, resulting in a positive power output. Furthermore, there is a secondary peak of C_P that occurs at $t/T \approx 0.22$, due to the heaving power ($C_{P,h}$). The timing of the secondary peak in $C_{P,h}$ coincides with the timing of the secondary force peak in Fig. 3.3. Finally, the third minor peak that occurs at $t/T \approx 0.38$ is associated with only the pitching power ($C_{P,\theta}$). At this time, a small positive (clock-wise) moment peak is generated that has the same sign as the pitching velocity (which is undergoing a pitching reversal beyond $t/T = 0.25$), thereby producing a positive power output. As k is increased to 0.10, the timing of primary power peak is delayed to $t/T \approx 0.16$, which is a consequence of the delay in peak force generation with increasing reduced frequency. As shown, the heaving motion plays a more dominant role in this peak power than the pitching motion. A key difference between $k = 0.10$ and $k = 0.06$ is that the pitching motion produces considerable negative power in the second half of the downstroke.

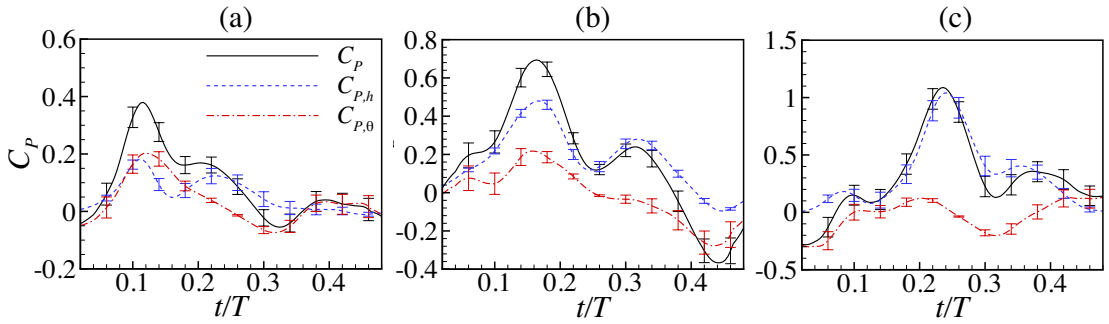

Figure 3.5: Transient power coefficient for (a) $k = 0.06$, (b) $k = 0.10$ and (c) $k = 0.14$.

As discussed above, the TEV for this higher reduced frequency remains in close proximity to the bottom surface of the foil, which results in a relatively large negative moment. Therefore, the product of the negative moment and positive pitching velocity of the foil is negative. Increasing k further to 0.14 the total power is shown to have negative values at the beginning of the downstroke due to the pitching contribution. This is a result of the LEV being shed from the previous upstroke half cycle that is captured by the foil as it begins its downstroke (see Fig. 3.4). In this case, the clock-wise rotating LEV that is advecting near the foil trailing edge along the upper surface generates a large positive moment about the pitching axis, which interacts with counter-clockwise rotating foil to produce a negative power output. At this higher reduced frequency, the pitching power has a negligible contribution to the primary power peak, which is generated at $t/T \approx 0.23$. Although the moment coefficient at this time is maximum, the foil is about to reverse its pitching motion from counter clock-wise to clock-wise rotation, such that the pitching velocity approaches zero (hence $C_{P,\theta} \approx 0$). Beyond $t/T \approx 0.25$ the pitching velocity switches sign from negative to positive, whereas the moment coefficient remains to be negative for a short period beyond this time and thus the product of the two results in a negative pitching power. Eventually, the LEV advects pasts the foil mid-chord and a small positive pitching power is

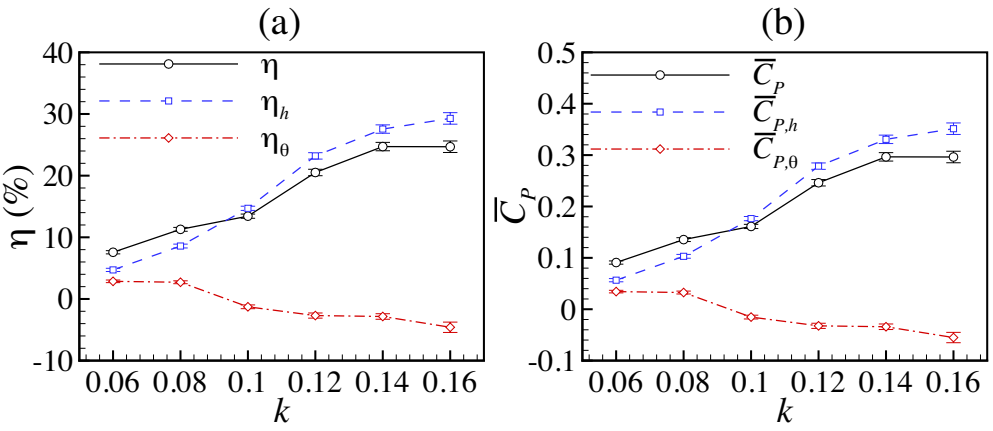

Figure 3.6: (a) Energy harvesting efficiency and (b) mean power coefficient versus reduced frequency. The individual contributions of the heaving and pitching motions are also shown.

produced at $t/T > 0.4$.

The total, heaving and pitching energy harvesting efficiency are shown in Fig. 3.6a. As shown, the total energy harvesting efficiency (η) increases with increasing reduced frequency until a maximum of approximately 25% is attained at $k = 0.14$. Beyond $k = 0.14$, the efficiency begins to decrease. The trend and efficiency values agree very well with other results reported in the literature (Kinsey & Dumas, 2008). For example, Zhu (2011) obtained peak efficiency values of 25% - 30% at $k \approx 0.14$ for a wide range of heaving and pitching amplitudes. Furthermore for the range of reduced frequencies that we tested, the heaving efficiency (η_h) is shown to increase with increasing k, but the rate of increase begins to decrease at $k \geq 0.12$. On the other hand, the pitching efficiency (η_θ) contributes positively to the total energy harvesting efficiency for $k < 0.1$, which then begins to have a negative influence for $k \geq 0.1$. At $k = 0.16$, the pitching efficiency becomes large enough (negatively) such that the total energy harvesting efficiency begins to drop. This trend was also observed by Kim *et al.* (2017). The mean total power coefficient, as well as the heaving and pitching contributions are given in Fig. 3.6b.

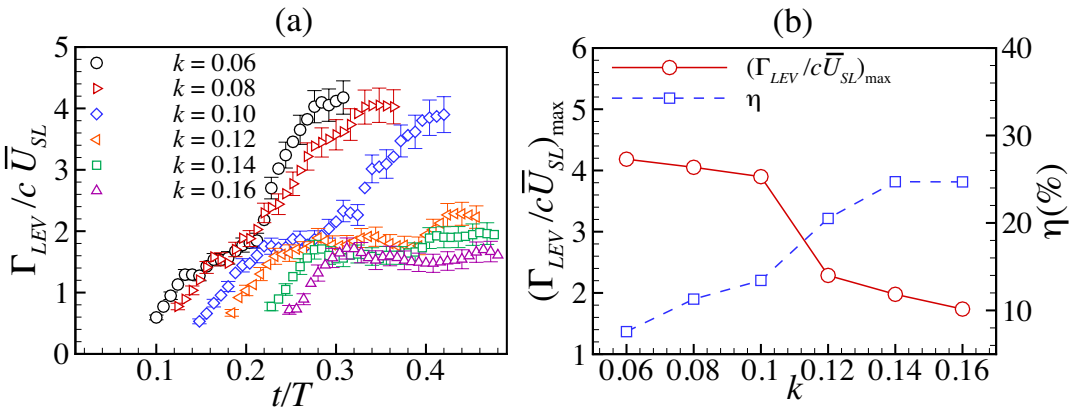

Figure 3.7: (a) Normalized LEV circulation versus time for $k = 0.06 - 0.16$ and (b) maximum LEV circulation and energy harvesting efficiency versus reduced frequency.

The mean power coefficient and energy harvesting efficiency show the same trend, but they differ by a constant factor of c/d for the parameters studied here. The effects of changing c/d on the efficiency by altering the maximum pitching angle are discussed by Totpal *et al.* (2018).

3.4.3 Optimal leading edge vortex formation

Based on the significant role of the LEV formation, we now investigate the relationship between the optimal vortex formation and energy harvesting efficiency. In Fig. 3.7a, the non-dimensional LEV circulation is given as a function of time for $k = 0.06 - 0.16$. The circulation is normalized by the chord length and mean leading edge shear layer velocity. The latter is approximated using the flow velocity using a frame of reference at the foil leading edge tip (Onoue & Breuer, 2016; Siala & Liburdy, 2019*a*). Note that this normalization of the LEV is consistent with the optimal vortex formation number parameter given by Dabiri (2009). The LEV circulation is computed based on the vortex identification technique proposed by Graftieaux *et al.* (2001). In this method, a scalar function, Γ_2, derived from

the velocity vector field is used to identify the vortex boundary. The circulation is calculated by integrating the vorticity contained within the LEV boundary defined by $\Gamma_2 = 2/\pi$. It is shown in Fig. 3.7 that for $k \leq 0.10$, the maximum LEV circulation falls within $3.8 - 4.0$, which is remarkably close to the universal optimal vortex formation number (Gharib *et al.*, 1998). At these reduced frequencies the time scale of LEV growth is relatively small when compared to the oscillation time scale. This allows the LEV to grow to its maximum possible size (as is determined by the chord length) and circulation. This is reflected by the formation of the TEV at these reduced frequencies, which allows the LEV to grow past the trailing edge, thereby forcing the trailing edge shear layer to roll into a large vortex. When k is larger than 0.10, the time scale of the LEV growth is slow compared with the foil oscillation time scale such that the end of a cycle is reached before the LEV attains its maximum possible size and strength. Shown in Fig. 3.7b is the maximum vortex formation number obtained by the LEV and the energy harvesting efficiency as a function of reduced frequency. Clearly the efficiency increases while the LEV formation number decreases. But this negative correlation appears to be driven by the ratio of time scales that influence LEV formation relative to the foil kinematic time scale. The maximum efficiency occurs at $k = 0.14$, where the LEV formation number is approximately equal to 2. Unlike in propulsion applications where the optimal vortex formation in the near-wake results in the greatest thrust, flapping energy harvesting systems rely more on the timing of the LEV formation and detachment. The reduced frequency of $k = 0.14$ seems to result in the best match between the LEV flow and foil oscillation time scales.

3.4.4 Contribution of flow structures to power production

To further elucidate the mechanisms responsible for producing the peak in both the power coefficient and energy harvesting efficiency near $k = 0.14$, we investigate the power output using the decomposition proposed in Section 3.3. In Fig. 3.8, we show the heaving power contribution from the positive, C_{P,h^+} and negative ,C_{P,h^-}, vorticity for $k = 0.10$, 0.14 and 0.16. It is quite evident that for all reduced

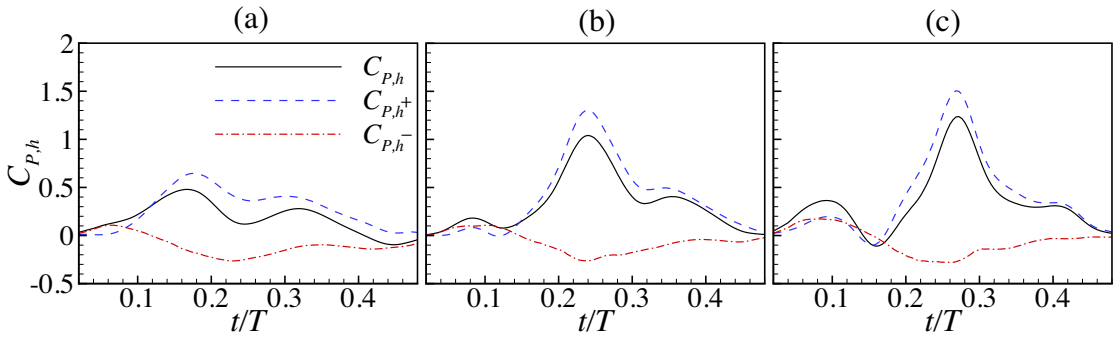

Figure 3.8: Transient heaving power coefficient showing the contributions of positive and negative vorticity for (a) $k = 0.10$, (b) $k = 0.14$ and (b) $k = 0.16$.

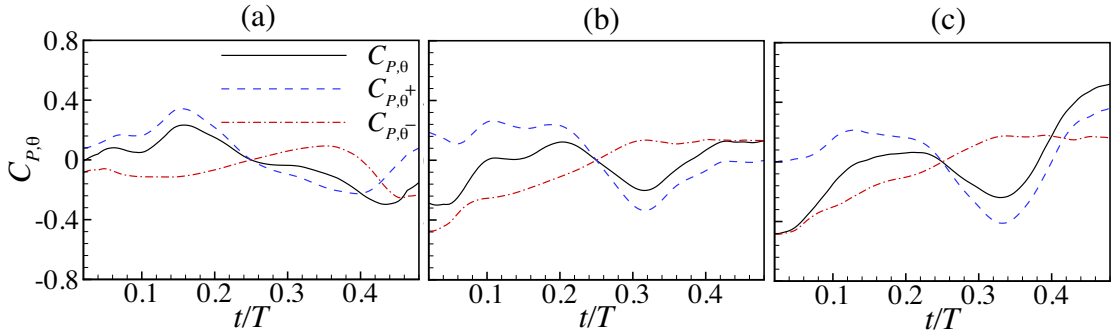

Figure 3.9: Transient pitching power coefficient showing the contributions of positive and negative vorticity for (a) $k = 0.10$, (b) $k = 0.14$ and (b) $k = 0.16$.

frequencies, the power production is dominated by the positive vorticity in the flow (i.e. leading edge vortex and its feeding sheer layer). As discussed previously, the peak in the heaving power is due to formation of the LEV. Furthermore, the heaving power from the negative vorticity has a negative global maximum that occurs at $t/T \approx 0.25$. This is coincident with the time at which the heaving velocity is maximum. Note that the large TEV for $k = 0.10$ that forms at $t/T \approx 0.45$ (see Fig. 3.4) has a negligible contributions to heaving power production, since the heaving velocity of the foil at this phase of the cycle is small.

In Fig. 3.9, the contributions of the positive and negative vorticity to the pitching power coefficient are presented. As shown, the trend in the total pitching power is significantly different for $k = 0.10$ when compared to $k = 0.14$ and 0.16. The difference is dominated by the contribution of negative vorticity, C_{P,θ^-}. For $k = 0.14$ and 0.16, there is a negative pitching power due to negative vorticity at the beginning of the downstroke. This is a consequence of the LEV from the upstroke being "caught" by the foil as it begins pitching downward. For $k = 0.10$, C_{P,θ^-} remains quite small until the TEV formation that occurs towards the end of the cycle (approaching the bottom heaving position) begins to produce relatively large negative pitching power. Furthermore, the positive vorticity contribution also has some distinct differences when comparing $k = 0.10$ to $k = 0.14$ and 0.16. For $k = 0.10$, there is a peak in C_{P,θ^+} that occurs at $t/T \approx 0.16$, which is due to the counter-clock wise moment produced by the LEV. This peak becomes less pronounced at the higher k values, since the LEV formation is shifted towards the mid-stroke, and consequently, the product of moment and pitching velocity is smaller (pitching velocity is zero at the mid-stroke). The large negative peaks of C_{P,θ^-} for $k = 0.14$ and 0.16 that occur at $t/T \approx 0.31$ and $t/T \approx 0.34$, respectively, are produced by the LEV that is still positioned in the up-stream portion of the foil. The negative counter clock-wise moment produced by the LEV is multiplied by the positive pitching velocity of the clock-wise rotating foil, thus producing negative power.

The cycle averaged power coefficient is shown in Fig. 3.10 for both the heaving and pitching contributions. Each is decomposed into contributions from positive and negative vorticty as indicated with the "+" and "-" signs. The negative vorticity contributes negatively to the total heaving power at an approximately constant value of $\overline{C}_{P,h^-} = 0.01$ for all reduced frequencies. On the other hand, the positive vorticity always has a favorable contribution, mainly due to the effects of the LEV. The mean contributions of the positive and negative vorticity on the pitching power is shown in Fig. 3.10b. The negative vorticity is primarily responsible for the significant increase in negative pitching power production. For $k \leq 0.10$ this

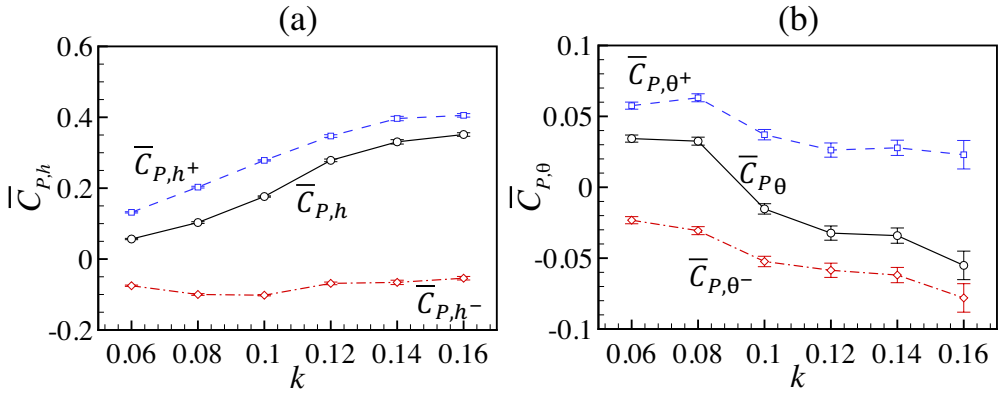

Figure 3.10: Cycle-averaged power contributions of the positive and negative vorticity to the (a) heaving power and (b) pitching power.

negative vorticity is due to the formation of the TEV structure near the end of the down-stroke. Whereas for $k \geq 0.10$ the LEV from the up-stroke is "caught" by the foil during the start of the downward pitching/heave motion and is the primary source of the negative pitching power.

3.5 Conclusions

Two dimensional particle image velocimetry experiments were conducted in a low-speed wind tunnel to investigate the feasibility of estimating the energy harvesting capabilities of a sinusoidally flapping foil energy harvesters using the impulse theory. The reduced frequency was varied from $k = 0.06$ to $k = 0.16$, and the pitching and heaving amplitudes were set at $\theta_0 = 75°$ and $h_0/c = 0.6$, respectively. These results help to identify the relative contributions to power production caused by the dominant flow structures.

The impulse-based aerodynamic force and moment equations were shown to be consistent with other studies in estimating the power produced by the heaving and pitching motions, respectively. The maximum energy harvesting efficiency of approximately 25% was obtained at $k = 0.14$, agreeing very well with results re-

ported in the literature for these conditions. The relationship between the concept of optimal vortex formation number and maximum energy harvesting efficiency was explored. The results show no established relationship between these two, and the maximum energy harvesting efficiency obtained at $k = 0.14$ is shown to be a result of the optimal match between the LEV and foil oscillation time scales.

In order to better understand the trends of energy harvesting efficiency and mean power output, the power production due to the force and moment were decomposed into contributions of positive and negative vorticity in the flow. It was observed that the contribution of the negative vorticity to the pitching motion was primarily responsible for the reduction of the harvesting efficiency and power output for $k > 0.14$. Specifically, due to the slower advective time scale of the LEV at higher k values, the clockwise rotating LEV generated during the previous cycle upstroke motion was shown to be caught by the downstream potion of the foil as it begins pitching/heaving downward. As a result, a large counter clockwise (negative) moment is produced, which interacts with the clock-wise rotating foil to produce a large negative pitching power.

The results of this study show that the impulse-based force calculation provides a means of investigating the mechanisms of power production of flapping energy harvesters in greater depth and detail. Future work will focus on further decomposing the impulse equations into vortex growth and vortex advection components. This may be of great importance to guide future studies in developing more effective kinematic motion in LEV-based energy harvesting systems.

Acknowledgments

The authors would like to thank Ali Mousavian and Cameron Planck for helping with designing the heaving/pitching device and developing the LabView code. Firas Siala acknowledges the financial support from Link Energy Foundation Fellowship. Also, financial support was provided from the Air Force Office of Scientific Research under the MURI grant FA9550-07-1-0540 and the National Science Foundation CBET Award Number 1804964.

Chapter 4 Experimental study of inertia-based passive deformation of a heaving and pitching airfoil operating in the energy harvesting regime

Firas F. Siala, Kiana Kamrani Fard and James A. Liburdy

Physics of Fluids
Under Review
American Institute of Physics, College Park, United States

Abstract

The effects of passive, inertia-induced surface deformation at the leading and trailing edges of an oscillating airfoil energy harvester are investigated experimentally at reduced frequencies of $k = fc/U_\infty = 0.10$, 0.14 and 0.18. Wind tunnel experiments are conducted using phase-resolved, two-component particle image velocimetry to understand the underlying flow physics, as well as to obtain force and pitching moment estimates using the vortex-impulse theory. Results are obtained for leading and trailing edge deformation separately. It is shown that both forms of deformation may alter the leading edge vortex inception and detachment time scales, as well as the growth rate of the circulation. In addition, surface deformation may also trigger the generation of secondary vortical structures, and suppress the formation of trailing edge vortices. The total energy harvesting efficiency is decomposed into contributions of heaving and pitching motions. Relative to the rigid airfoil, the deforming leading and trailing edge segments are shown to increase the energy harvesting efficiency by approximately 17% and 25%, respectively. However, both the deforming leading and trailing edge airfoils operate most efficiently at $k = 0.18$, whereas the peak efficiency of the rigid airfoil occurs at $k = 0.14$. It is shown that the deforming leading and trailing edge airfoils enhance the heaving contribution to the total efficiency at $k = 0.18$ and the negative contribution of the pitching motion at high reduced frequencies can be alleviated by using a deforming trailing edge.

4.1 Introduction

The escalating demand for reducing dependence on fossil fuels has provided significant motivation toward the development of alternative and clean energy harvesting devices. One attractive energy resource is the wind, where typically rotational-based turbines are used to extract the kinetic energy of the flow. However, these traditional turbines possess several undesired economical as well as environmen-

tal impacts (Saidur *et al.*, 2011). An alternative energy harvesting system that provides several advantages to more conventional rotating-based turbines is the oscillating airfoil energy harvester. These systems rely on the use of combined heaving and pitching airfoils to harvest energy at efficiencies ranging from 20% to 40% (Kinsey & Dumas, 2008; Zhu, 2011; Kinsey & Dumas, 2012; Ma *et al.*, 2017). While these oscillatory-based devices have certainly been shown to be quite promising, there is potential for improved efficiency (Young *et al.*, 2014).

The concept of extracting flow energy using oscillating airfoils is inspired by the unsteady flapping flight of insects and birds (Sane, 2003; Ho *et al.*, 2003; Shyy *et al.*, 2007; Chin & Lentink, 2016). The flapping/oscillating motion of these natural fliers induce large-scale unsteady flow separation that causes significant deviations from the well-known static aerodynamic lift curve, in a process known as dynamic stall. During dynamic stall, flow separates at the leading edge of the airfoil surface and subsequently rolls into leading edge vortices (LEVs). Polhamus (1971) has shown that LEVs are beneficial to lift generation by producing a region of low pressure on the suction side of the airfoil, resulting in a strong suction force, as long as the LEV remains attached to the airfoil surface. Unlike rotary turbines where flow around the blades must be attached to the airfoil surface to achieve high efficiency, oscillating energy harvesters exploit the unsteady flow separation and LEV formation to attain high efficiency. Although the role of LEVs in forward flapping flight efficiency (i.e. thrust producing systems such as birds) is well documented (Tuncer & Platzer, 2000; Tuncer & Kaya, 2005), their effects on energy harvesting devices, which tend to operate in different flow regimes, are yet to be thoroughly explored.

The oscillatory/flapping motion of an airfoil operating in the energy harvesting regime is typically modeled as combined sinusoidal heaving and pitching motion. Then, the instantaneous power output of a heaving and pitching airfoil can be expressed as:

$$P = F_y \dot{h} + M_z \dot{\theta} \tag{4.1.1}$$

where F_y is the vertical force (i.e. perpendicular to the free stream flow), M_z is

the aerodynamic moment about the pitching center of the airfoil, $\dot{h}$ is the heaving velocity and $\dot{\theta}$ is the pitching velocity. The vast majority of published studies on oscillating energy harvesters focused on optimizing the motion kinematics, mostly using numerical simulations (Dumas & Kinsey, 2006; Kinsey & Dumas, 2008; Zhu, 2011; Ashraf *et al.*, 2011*a*; Ma *et al.*, 2017) with fewer experimental studies (Kim *et al.*, 2017; Totpal *et al.*, 2018; Siala & Liburdy, 2019*c*). These results show that energy harvesting efficiency is maximized when the airfoil is oscillating at pitching amplitudes of 60°-80°, heaving amplitudes of 0.5c-1.0c (c is airfoil chord length) and reduced frequencies ($k = fc/U_\infty$, where f is oscillation frequency and U_∞ is the free stream velocity) of 0.12-016.

It can be seen from Eq. (1) that there are two main factors influencing the power output: (i) the magnitude of the force F_y and pitching moment M_z and (ii) the correlation between F_y and $\dot{h}$ as well as between M_z and $\dot{\theta}$. Several studies have been conducted in the past few years that investigate different mechanisms that enhance both the peak force and moment, as well as the correlation between the aerodynamic forces and airfoil motion (Ashraf *et al.*, 2011*b*; Le *et al.*, 2013; Xie *et al.*, 2014; Lu *et al.*, 2015). One prominent mechanism is the use of structurally deforming airfoils. Previous studies on insect wings as well as micro-air-vehicles suggest that deformation near the trailing edge leads to the generation of higher thrust and lift forces (Miao & Ho, 2006; Zhao *et al.*, 2011; Nakata *et al.*, 2011; Cleaver *et al.*, 2014). Airfoil surface deformation can either be controlled or passive. In controlled surface flexibility, the deformation of the surface is prescribed and the effects of airfoil inertia and the fluid-structure interactions are neglected. Hoke *et al.* (2015) used a two-dimensional (2D) laminar simulation with prescribed camber deformation to show that the energy harvesting efficiency is increased by 15.8% relative to a fully rigid airfoil. When the camber deformation is prescribed correctly, the timing of LEV formation and hence the correlation between the forces and airfoil motion is enhanced. Furthermore, Liu *et al.* (2013) numerically modeled 2D oscillating airfoil energy harvesters with deforming leading and trailing edges. The motion of the deforming leading and trailing edges was predetermined based

on *a priori* structural analysis. They show that airfoils with a deforming trailing edge enhance the strength of the LEV and resultant peak force magnitudes, whereas deformation at the leading edge controls the timing of LEV formation, and thus the correlation between the aerodynamic forces and airfoil motion. Interestingly, both leading and trailing edge controls shifted the peak efficiency to higher reduced frequencies compared to a rigid airfoil.

Passive surface deformation can be divided into two categories: (i) inertia-induced deformation and (ii) flow-induced deformation. Flow-induced deformation occurs when the airfoil density is comparable with the density of the surrounding fluid. Tian *et al.* (2014) conducted a numerical model based on the immersed boundary method to compare the effects of passive deformation with controlled and rigid airfoils. Their results show that passive, flow-induced surface deformation at the leading edge improved the energy harvesting performance by only 1%, whereas controlled leading edge deformation increased the efficiency by 11.3% compared to a rigid airfoil. With controlled deformation, the leading edge segment was set to deform such that it produced a smaller effective angle of attack compared to a rigid airfoil, which was shown to slow down the formation and detachment of the LEV. Consequently, the flapping airfoil takes advantage of the LEV presence for a longer period of time during the oscillation cycle. Conversely, passive deformation of the leading edge segment was shown to be very small, and as a result, it had minimal impact on the energy harvesting efficiency. Moreover, Liu *et al.* (2017) studied the effects of passive trailing edge segment deformation on the performance. They determined that with appropriate structure-to-fluid density and natural frequency of the trailing edge segment, the efficiency is enhanced by 7.24%. The deforming trailing edge creates a camber that enhances the pressure difference between the upper and lower surfaces of the airfoil. The influence of inertia-induced deformation of the leading edge on the performance was investigated experimentally by Totpal *et al.* (2018) at reduced frequencies of 0.04-0.08. While their results show that leading edge deformation reduces the energy harvesting efficiency by 10% relative to a rigid airfoil at $k = 0.08$, the negative effects of the deformation were shown to

subside as k is increased from $k = 0.04$ to 0.08. It remains unknown whether at larger reduced frequencies, the effects of inertia-induced leading edge deformation become beneficial.

In this paper, we conduct wind-tunnel testing and particle image velocimetry (PIV) measurements to investigate the feasibility of using inertia-induced deformation at the leading and trailing edges of the airfoil in the range of $k = 0.10$ - 0.18. To the best of our knowledge, there exists no experimental data that validate the feasibility of using deforming airfoil surface in the range of reduced frequencies relevant to optimal energy harvesting performance. We are specifically interested in seeing whether the negative effects of inertia-induced deformation subside, and even become favorable at the optimal reduced frequency range. Due to the difficulty of directly measuring the aerodynamic forces in a highly unsteady airfoil motion in wind tunnels, we use the vortex-impulse theory (Wu *et al.*, 2007*b*) to estimate both the force and moment to calculate power output. We have previously used the vortex-impulse theory with success to estimate the aerodynamic forces and energy harvesting performance using velocity data obtained from PIV (Siala & Liburdy, 2019*b*,*c*). Our objective is to first understand the underlying flow physics associated with deforming surfaces, and then to quantify and compare the power output and energy harvesting efficiency of the deforming leading and trailing edge airfoils with a fully rigid one.

The rest of the paper is organized as follows. In section 4.2, the experimental and data analysis techniques are described. In section 4.3, we compare the effects of deforming the leading and trailing edges with a fully rigid airfoil on the vorticity field, LEV evolution and energy harvesting efficiency. In section 4.4, conclusions and implications of this work are provided.

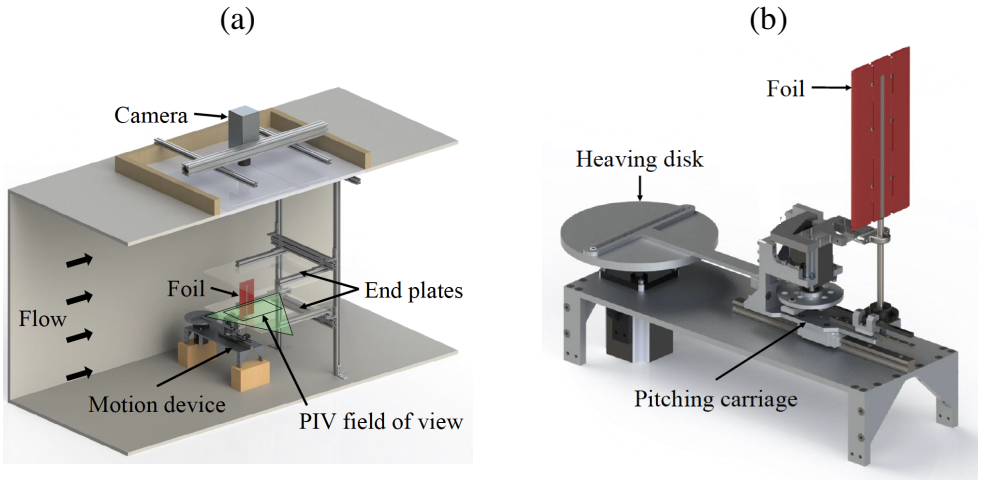

Figure 4.1: (a) Drawing of the experimental setup illustrating the wind tunnel, motion device and PIV arrangement and (b) zoomed-in view of the motion device. Figures are adopted from Totpal (2017) .

4.2 Methodology

4.2.1 Experimental techniques

Fig. 4.1 shows the experimental setup in the wind tunnel and a zoomed-in view of the motion device used to achieve the airfoil motion. The wind tunnel is located at Oregon State University, and is a closed loop with a test section size of 1.37 m x 1.52 m with turbulence intensities below 2%. In addition, stationary end plates were placed approximately 2 mm from the airfoil tips to mimic quasi two-dimensional flow. The motion device consists of a scotch-yoke mechanism to generate the heaving motion and a combination of scotch-yoke and rack-and-pinion mechanisms to generate the pitching motion, according to the following:

$$h = h_0 cos(2\pi f t) \tag{4.2.1}$$

$$\theta = \theta_0 cos(2\pi f t + \Phi) \tag{4.2.2}$$

where h_0 is the heaving amplitude, θ_0 is the pitching amplitude and Φ is the phase-shift between heaving and pitching. The motion device was controlled using a LabVIEW program. The reduced frequency was varied by changing the free stream velocity while keeping the oscillation frequency fixed at 1.4 Hz. The Reynolds numbers ($Re = U_\infty c/\nu$, where ν is the kinematic viscosity) used in this study are 14189, 10135 and 7883 for $k = 0.10$, 0.14 and 0.18, respectively. The effect of Reynolds number at this low range has been found to have minimal impact on the energy harvesting performance (Xiao & Zhu, 2014).

The airfoil used in this study was manufactured in-house using fused deposition modeling and has a chord length, thickness and aspect ratio of 125 mm, 6.25 mm and 2, respectively. The airfoil leading and trailing tips are elliptical with 5:1 major to minor axis ratio. It consists of four acrylonitrile butadiene styrene (ABS) pieces and a machined titanium that is the three quarters the length of the airfoil span. The titanium rod provides structural support along the airfoil span to reduce span-wise flexibility. Two of the ABS pieces are attached to the titanium rod using pressed inserts to form the main body section of the airfoil. The remaining two ABS pieces consist of leading edge (LE) and trailing edge (TE) segments, each with a length of $c/3$. These segments are configurable to either rigidly attach to the airfoil main body, or serve as passively-actuated edges mimicking simplified surface deformation. The passive deformation of the LE/TE was established by inserting a torsion rod into slots along both the main body and LE/TE, forming a hinge. The rod was secured at one end of the body and the other end to the LE/TE, providing a means to allow rotation of the LE/TE. A schematic of the airfoil and the hinge mechanism is shown in Fig. 4.2. Note that in this study, the flexible TE and LE configurations are investigated separately.

Two-component PIV measurements were obtained at the airfoil mid-span using a dual-head Nd:YAG pulsed laser (EverGreen, 145 mJ/pulse, max repetition rate of 15 Hz). A light sheet of approximately 1.5 mm thickness was generated at the mid-span of the airfoil using a LaVision optics module. The wind tunnel was seeded with vegetable oil particles, which were generated using an in-house built

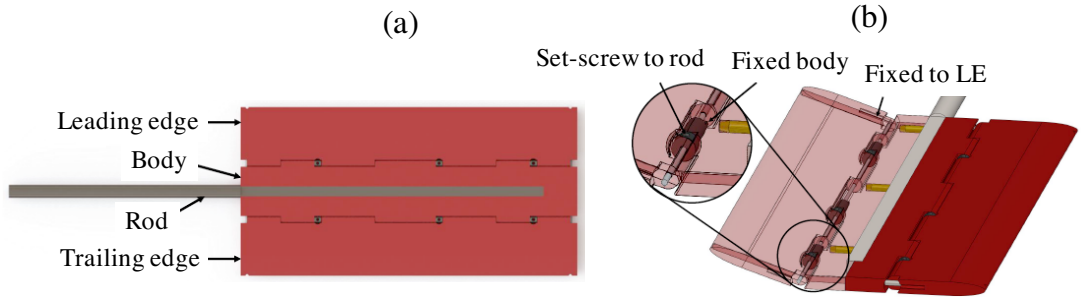

Figure 4.2: (a) Top view of the airfoil and (b) detailed view of the airfoil LE/TE hinge mechanism.

Laskin Nozzle. Particle images were collected using a CCD camera (Image Pro, LaVision) with a resolution of 1600 $\times$ 1200 pixels. PIV images were processed with DaVis v8.4 software. The velocity fields were calculated using two passes of interrogation window size of 64 $\times$ 64 pixels, followed by two more passes of interrogation window size of 32 $\times$ 32 pixels, with an overlap of 50%. The time between the image pair was set such that an average of 8 pixel displacement per interrogation window was achieved in the streamwise direction. Velocity vectors were validated using a minimum correlation peak ratio of 1.2 as well as a moving-average validation scheme, where each velocity vector was replaced by the average of its neighbors if the difference between that velocity vector and its neighbors is greater than two standard deviations of the neighboring vectors. Overall, the percentage of velocity outliers was found to be approximately 2% of the entire velocity field. The velocity measurement uncertainty has been estimated using the correlation statistics technique (Wieneke, 2015). The maximum uncertainty of the streamwise and cross-stream velocity components were found to be 3.5% and 5.8% of their respective maximum values. The velocity errors are then propagated to determine the uncertainty in vorticity and aerodynamic loadings. Detailed analysis of the propagation method can be found in Appendix B.

A total of 126 phases during the downstroke motion with a sampling time of $\Delta t/T = 0.004$ were acquired. For each phase, one hundred images were acquired

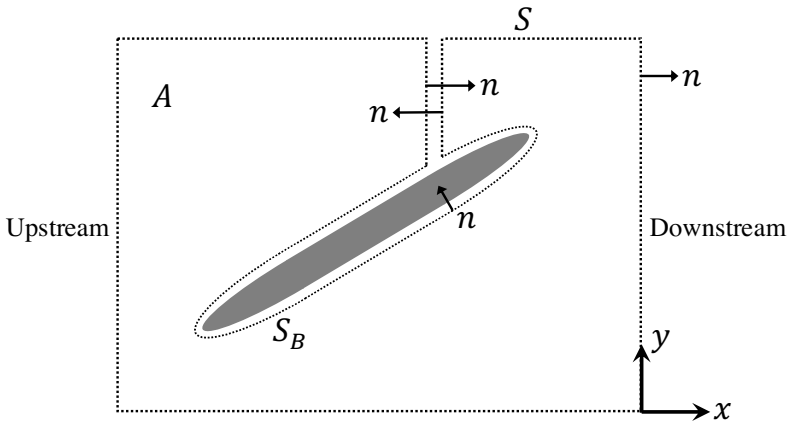

Figure 4.3: Control volume used for impulse-based force and moment calculation.

to calculate the phase-averaged velocity fields. The PIV system and airfoil motion were synchronized using LabVIEW. In order to obtain velocity data in the shadow region caused by the presence of the airfoil, the experiments were repeated at a phase delay of 180° for each phase of interest. The 180° out of phase flow fields were then mirrored and stitched to the rest of the vector field to construct the full flow field surrounding the airfoil. This can be done because the flow, airfoil shape and motion are all symmetric. Additionally, a second camera was used to capture the flow field in the downstream region. The two cameras were overlapped by 14 vectors and the overlapped region was smoothed with a 3×3 moving-average filter.

4.2.2 Vortex-impulse theory: force and moment estimation

As previously mentioned, direct force and moment measurements of highly unsteady airfoils operating with large amplitudes of motion in wind tunnels are often not feasible. The difficulty is due to the airfoil inertial forces being in the same order of magnitude as the aerodynamic forces or larger for reduced frequencies relevant to energy harvesting applications (Totpal, 2017). Since flow over oscillating airfoils operating in high amplitudes of motion is dominated by large scale

vortical structures, it is then ideal to describe the aerodynamic loadings based on the dynamics of these vortical structures. In fact, the vorticity/circulation of these vortical structures indirectly represent the momentum imparted by the moving airfoil to the fluid. Wu (1981) and Lighthill (1986*b*) have independently shown that forces generated by an airfoil can be obtained by taking the time-derivative of the vortex impulse, $\mathbf{P_F}$, which, in two-dimensional flows, is defined as:

$$\mathbf{P_F} = \int \mathbf{x} \times \boldsymbol{\omega} dA \tag{4.2.3}$$

where $\mathbf{x}$ is the position vector and A is the area occupied by the fluid. Lighthill explains that this expression is related to the total impulse (in the classical mechanics sense) required to establish a vorticity field, $\boldsymbol{\omega}$, from rest. For two-dimensional flows, Siala & Liburdy (2019*b*) have shown that the total force acting on the airfoil in a finite control volume can be written as:

$$\mathbf{F} = -\rho \frac{d\mathbf{P_F}}{dt} + \rho \oint_S \mathbf{n} \cdot \Big(\frac{1}{2} [\mathbf{u} \cdot \mathbf{u}] \underline{\mathbf{I}} - \mathbf{uu} \Big) dS \tag{4.2.4}$$

where $\underline{\mathbf{I}}$ is the identity tensor, $\mathbf{n}$ is the normal vector pointing away from the fluid and S is the external surface of the control volume. The second term of Eq. 4.2.4 represents the effects of vorticity shed in the far wake on the forces. For suddenly-accelerated bodies from rest where all the vorticity is captured in the control volume, this term can be shown to equal zero (Saffman, 1992). The finite-domain impulse equation originally derived by Noca (1997) contains other additional terms. However, Siala & Liburdy (2019*b*) have shown that by selecting an origin location of the position vector located anywhere along y-axis of the downstream control volume boundary (see Fig. 4.3), these additional terms that are included in Noca's equation become negligible, thus significantly simplifying the force equation to the expression given in Eq. 4.2.4. This can be done because the force equation is theoretically independent of the origin location. Experimentally, however, it is well known that errors in force calculation can be significantly amplified by the origin location (Noca, 1997). We have determined in our previous study that the

error associated with the origin location can be significantly reduced by setting the origin location at the downstream boundary, located at least one chord length from the trailing edge (Siala & Liburdy, 2019*b*). For a thorough discussion on practical considerations of the impulse-based force method, refer to the studies conducted by DeVoria *et al.* (2014) and Siala & Liburdy (2019*b*). Moreover, because the experiments are conducted in air, the added-mass of the airfoil is determined to be very small and therefore neglected in Eq. 4.2.4. Validation of the force estimation based on the impulse method is provided in Siala & Liburdy (2019*b*).

Similarly, the vortex impulse associated with the aerodynamic moment, $\mathbf{P_M}$, can be defined as:

$$\mathbf{P_M} = \frac{1}{2}\int (\mathbf{x}\cdot\mathbf{x})\boldsymbol{\omega} dA \tag{4.2.5}$$

The aerodynamic moment can then be shown to be written as (Wu *et al.*, 2007*b*; Siala & Liburdy, 2019*c*):

$$\mathbf{M} = \rho\frac{d\mathbf{P_M}}{dt} + \rho\int \mathbf{x}\times(\mathbf{u}\times\omega)dA - \rho\frac{1}{2}\oint(\mathbf{x}\cdot\mathbf{x})\mathbf{n}\times(\mathbf{u}\times\boldsymbol{\omega})dS \tag{4.2.6}$$

Since we are interested in the moment about the pitching center of the airfoil, we fixed the origin location at the pitching axis of the airfoil, which is located at the mid-chord. The maximum uncertainty of the instantaneous force and moment were found to be 10.6% and 13.2% of the peak force and moment, respectively.

4.2.3 Pressure calculation from PIV data

In many cases, the mechanisms of force and moment production can be illuminated by visualizing the pressure field. To do this, we use the algorithm described by Dabiri *et al.* (2014) to calculate the pressure field from phase-averaged velocity data. Briefly, the algorithm is used to perform a direct integration of the pressure gradient term in the Navier-Stokes equations along eight paths through each point in the flow field. The starting point of all eight integration paths is located at the control volume boundary. The median of the pressure value obtained from all

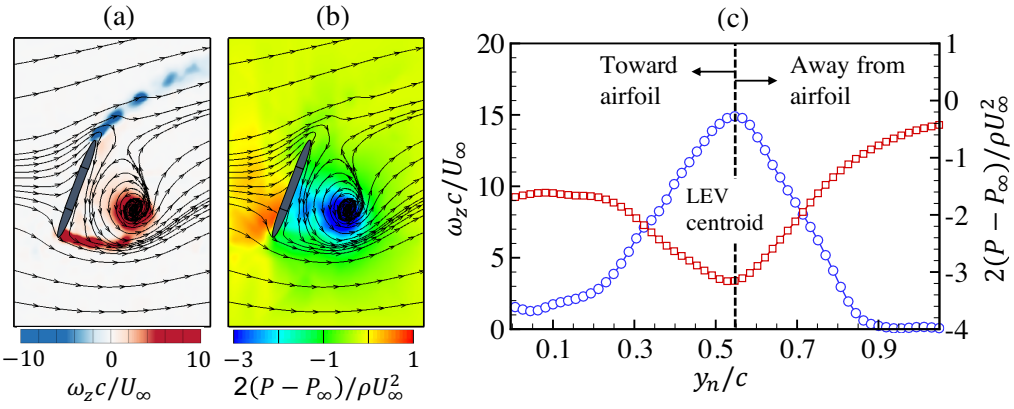

Figure 4.4: (a) Vorticity field and streamlines and (b) pressure field and streamlines for $k = 0.10$ at the mid-downstroke. (c) Wall-normal profile of the vorticity and pressure through the LEV center. The blue circles represent the vorticity and the red squares represent the pressure.

eight integration paths is then used to estimate the pressure at each point in the field. Although the pressure fields obtained using this method are not sufficiently accurate for force evaluation in our current experimental setup, we present the pressure fields for qualitative purposes, to provide more insight in interpretation of the results. The pressure field is qualitatively validated in Fig. 4.4. In Fig. 4.4a and 4.4b, the non-dimensional vorticity and pressure fields, along with the flow streamlines, are shown for $k = 0.10$ for the rigid airfoil case. It is shown that the pressure and vorticity fields are well correlated, with the pressure minima and maxima being generated in the LEV core and on the upper surface of the airfoil (stagnation point), respectively. The wall-normal profiles of the vorticity and pressure are shown in Fig. 4.4c. The wall-normal distance, y_n/c, is equal to zero at the airfoil surface. The profile is drawn through the LEV center, which is detected by the maximum vorticity value. As expected, the peak vorticity and pressure are shown to correlate very well. Going away from the surface, the pressure slowly approaches free stream pressure and the vorticity decays rapidly to $\omega_z c/U_\infty = 0$

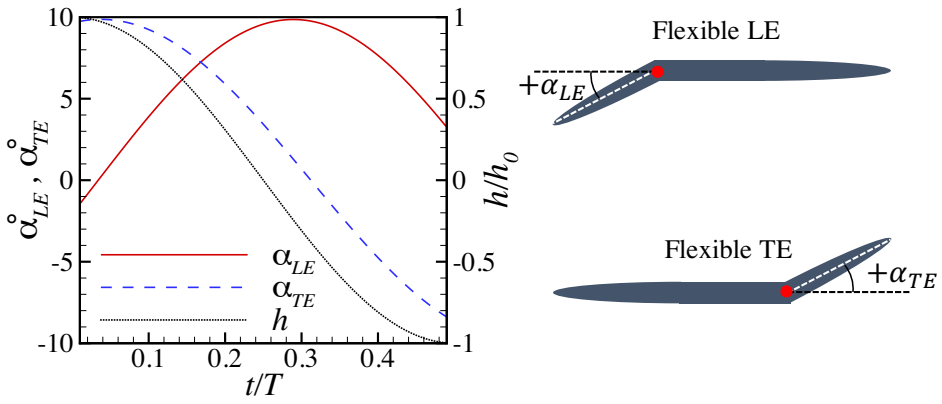

Figure 4.5: Leading and trailing edge deformation angle relative to the airfoil chord as a function of time during the downstroke motion. The heaving motion, h, is also shown for reference. Positive angles indicate that the LE/TE are deformed counter-clockwise relative to the airfoil main body.

4.3 Results

n this section, we present results for rigid, flexible LE and flexible TE airfoils operating at reduced frequencies, k, of 0.10, 0.14 and 0.18, while holding the heaving amplitude, pitching amplitude, phase shift and pitching axis fixed at $h_0/c = 0.6$, $\theta_0 = 75°$, $\Phi = 90°$ and $x_p/c = 0$ (mid-chord). Due to the symmetry of the problem, the results are only provided for the downstroke motion of the airfoil.

4.3.1 Leading and trailing edge deformation motion

Before analyzing their effects on the flow physics, it is important to report the motion of the passive deformation of the leading and trailing edges during the oscillation cycle. Key parameters that determine the degree of deformation are the torsion spring natural frequency and the linear density of the LE/TE. The natural frequency can be defined as $f_N = 1/2\pi\sqrt{\tau/I_m}$, where τ is the spring constant and I_m is the moment of inertia about the hinge. The torsion spring constant was calculated by attaching a known mass to the LE/TE while the wing was static.

Images of the downward deflection were recorded and used to calculate the angle of deflection, $\theta_{LE/TE}$. The torsion spring constant is calculated using $\tau = \frac{T}{\theta_{LE/TE}}$, where T is the torque applied to the LE/TE. Following Liu *et al.* (2017), the natural frequency of the deforming LE/TE is non-dimensionalized as $f_N^* = f_N c/U_\infty$, to obtain f_N^* of 0.6, 0.85 and 1.1 for k of 0.10, 0.14 and 0.18, respectively. Furthermore, the linear density of the LE/TE segments, $\rho_l = s\rho_{LE/TE}$ (where s is airfoil thickness and $\rho_{LE/TE}$ is the density of the LE/TE) is normalized by the fluid density ρ and airfoil chord length c to obtain the structure-to-fluid density ratio $\mu = \rho_l/c\rho$. The structure-to-fluid density used in this study is $\mu = 27.3$, which is significantly higher than the values of $\mu = 0.03$-0.6 used by Liu *et al.* (2017). A large value of the structure-to-fluid density is used in this study to reduce the effects of the flow on deformation and enhance the magnitude of the inertia-based deformation of the LE/TE.

In Fig. 4.5, the deformation angle of the leading and trailing edges are shown in degrees as a function of time during the downstroke motion of the airfoil. Positive angles indicate that the LE/TE are deflected counter-clockwise relative to the airfoil main body. It can be seen that there is an approximately 90° phase-lag between the motion of the LE and TE. The peak positive angle of deformation of the LE occurs approximately during the mid-downstroke, whereas the positive peak deformation angle of the TE occurs as the airfoil undergoes motion reversal at the beginning of the downstroke. Measurement of the deformation angle was conducted with and without free stream flow, and the results were found to be essentially identical. Since we are varying the reduced frequency by changing only the free stream velocity while keeping the oscillation frequency fixed, the deformation angles are the same for $k = 0.10$-0.18. Furthermore, the geometric effective angle of attack induced by the deformation of the leading and trailing edges can be defined as follows:

$$\alpha_{e,LE/TE} = \theta + \beta_{LE/TE} \tag{4.3.1}$$

where $\beta_{LE/TE}$ is the interior angle measured from the lines from the leading edge to

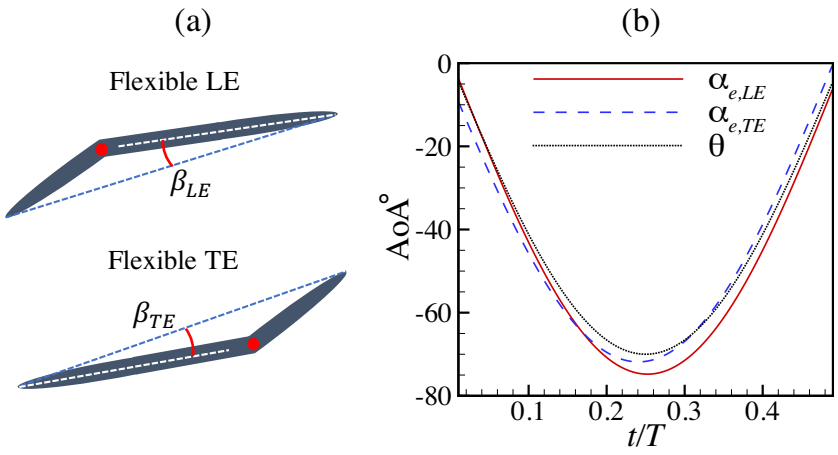

Figure 4.6: (a) Schematic sketch showing the angle β induced by the leading/trailing edge motion and (b) effective angle of attack induced by the leading and trailing edge deformation. For reference, the pitching angle, θ, is also shown.

the trailing edge tips and along the chord of the main airfoil body, as shown in Fig. 4.6(a). In Fig. 4.6(b), the angle of attack (AoA) induced by the leading and trailing edges, as well as the pitching angle are shown during the downstroke. As can be clearly seen, the deformation of the leading edge enhances the AoA compared to a rigid airfoil (whose geometric AoA is simply equal to θ), throughout most of the downstroke. On the other hand, the deforming trailing edge case is shown to enhance the the AoA up until $t/T \approx 0.3$. For $t/T > 0.3$, the motion of the trailing edge segment is reversed, resulting in a smaller AoA compared to the rigid airfoil.

4.3.2 Vorticity field characterization

The vorticity field was calculated from velocity using a central difference scheme. The average uncertainty was found to be approximately 4.7% of the maximum vorticity. Snapshots of the vorticity field evolution for the rigid, flexible LE and flexible TE airfoils operating at $k = 0.10$ are shown in Fig. 4.7. As the airfoil

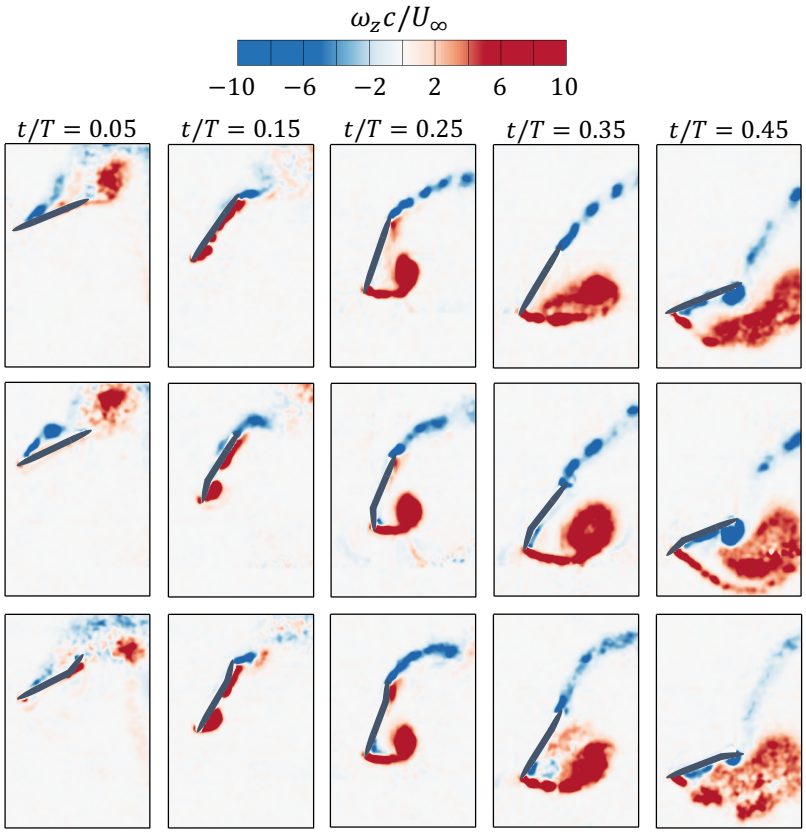

Figure 4.7: Non-dimensional vorticity field at $k = 0.10$ for the rigid (top row), flexible LE (middle row) and flexible TE (bottom row) airfoils during the downstroke motion.

begins its downstroke motion, the flow on the upper surface of the airfoil is still not fully attached due to the flow separation that occurred during the upstroke motion. As time progresses, the flow eventually begins to attach on the upper surface and separates at the leading edge of the bottom surface to form a counter-clockwise rotating LEV. At $t/T = 0.15$, it can be seen that the LEV generated by the flexible LE and TE airfoils is slightly larger than the LEV of the rigid airfoil. At $t/T = 0.25$, the LEV is shown to be lifted-off from the lower airfoil surface for all three cases, while the trailing edge vorticity continues to shed into the wake.

The trailing edge vortex sheet sheds in a similar manner for the rigid and flexible LE cases, whereas for the flexible TE case the vorticity is shown to have a more pronounced curved trajectory. Furthermore, the LEV size keeps increasing as long as the leading edge shear layer keeps feeding the LEV with vorticity. Eventually, the shear layer strength begins to decay and it disconnects from the LEV. At $t/T = 0.35$, the shear layer of the flexible TE airfoil begins to roll into discrete small-scale vortex structures in the from of a Kelvin-Helmholtz-like instability, whereas for the rigid and flexible LE cases the shear layer vorticity appears to be confined in a more continuous vortex sheet. As the airfoil approaches the end of the downstroke at $t/T = 0.45$, the shear layer is shown to be completely disconnected from the LEV for both the rigid and flexible TE cases, whereas it appears to remain loosely connected to the LEV in the flexible LE case. Moreover, as the LEV convects downstream past the airfoil trailing edge, it causes the trailing edge shear layer to form into a large distinct trailing edge vortex (TEV). Several studies have described this process as a bluff-body like vortex shedding, where the flow from the upper surface of the airfoil and LEV forms a saddle point near the trailing edge, which forces the trailing shear layer to roll into a TEV (Rival *et al.*, 2014; Widmann & Tropea, 2015; Siala *et al.*, 2017). On the other hand, the TEV formation is significantly suppressed by the flexible TE airfoil. At $t/T \approx 0.35$, the trailing edge segment begins to deform clockwise relative to the airfoil main body (see Fig. 4.5) and it becomes almost parallel with the streamwise flow at $t/T = 0.45$. As a result, the flow leaving the trailing edge from the upper surface tends to be more aligned with the streamwise flow, thus significantly reducing the velocity gradient near the airfoil trailing edge.

In Fig. 4.8, the vorticity evolution for $k = 0.14$ for all three cases is shown. The evolution process of the LEV remains the same as for $k = 0.10$, with few noticeable differences as described here. Firstly, as the airfoil downstroke begins, significant negative vorticity remains in close proximity to the airfoil. This is associated with the LEV generated from the upstroke motion. With increasing reduced frequency, the flow convection time scale increases relative to the time

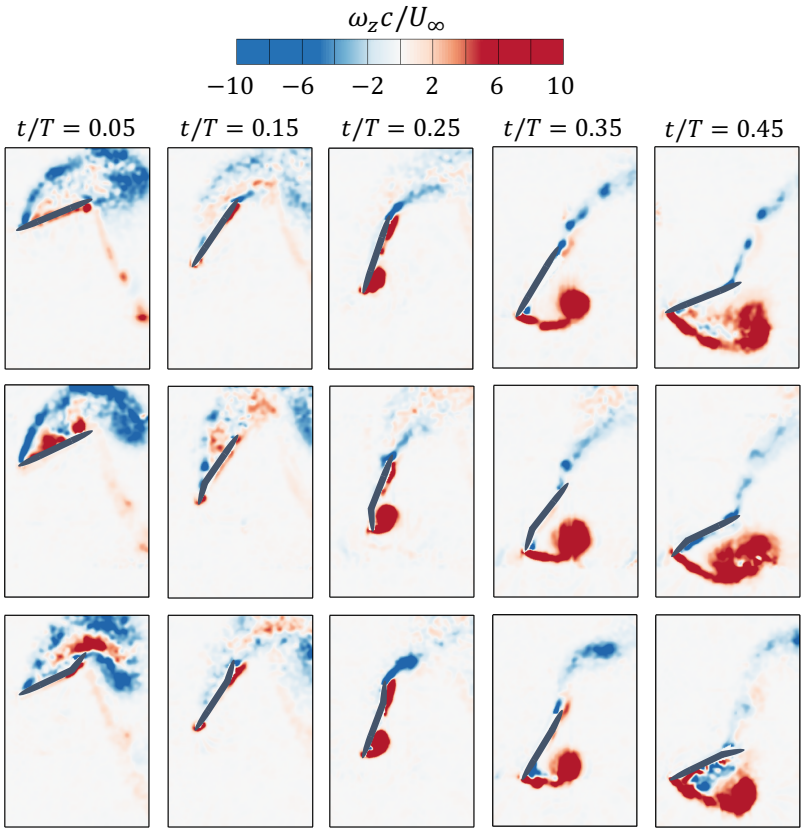

Figure 4.8: Non-dimensional vorticity and velocity fields at $k = 0.14$ for rigid (top row), flexible LE (middle row) and flexible TE (bottom row) airfoils during the downstroke motion. Note that only every other velocity vector is shown.

scale of airfoil motion, and therefore the airfoil captures the LEV during motion reversal before the LEV completely convects into the wake. Secondly, the inception time of the LEV is delayed to later in the cycle at higher reduced frequencies. Furthermore, at $t/T = 0.25$, the LEV is shown to remain attached to the airfoil surface, compared with the earlier detachment for $k = 0.10$. The LEV generated by the flexible LE case is also shown to be slightly larger than the LEV of the rigid and flexible TE case. Compared to $k = 0.10$, the LEV of the flexible TE case grows at a slightly slower rate due to the decrease in the deformation angle of the TE

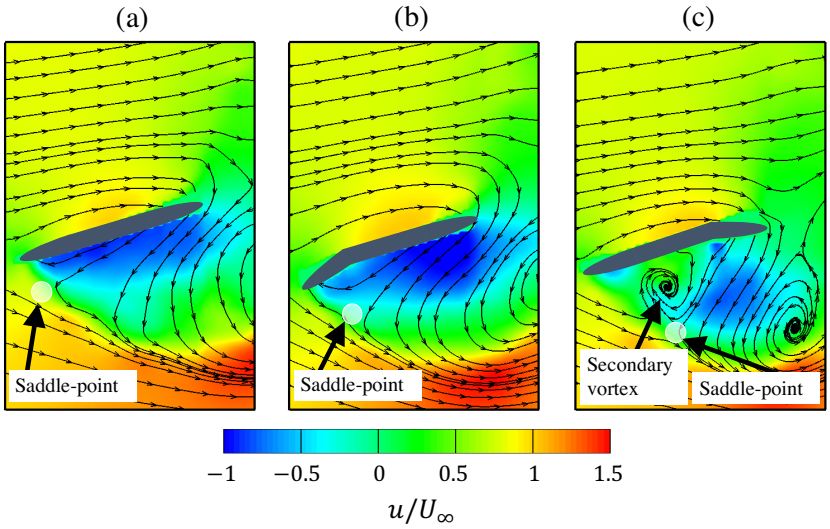

Figure 4.9: Zoomed-in view of the streamwise velocity contours and streamlines at $k = 0.14$ and $t/T = 0.45$ for (a) rigid, (b) flexible LE and (c) flexible TE airfoils.

at this instant, as shown in Fig. 4.6b. As time progresses, the LEV size remains fairly constant for the rigid and flexible TE cases at $t/T > 0.35$, whereas it keeps growing until $t/T = 0.45$ for the flexible LE case. As the airfoil approaches the end of the downstroke, the LEV begins to convect past the airfoil trailing edge, however no TEV formation is observed. This is because by the time the LEV approaches the airfoil trailing edge, the angle of attack of the airfoil is quite small, such that the trailing edge shear layer is not strong enough to roll into a distinct TEV structure. At $k = 0.14$, the vortex shedding in the wake switches from 2P to 2S, where the former represents two pairs of vortical structures (LEV and TEV) shed per oscillation cycle, and the latter represents two single vortices shed per oscillation cycle (one LEV per half cycle) (Williamson & Roshko, 1988). Lastly at $t/T = 0.45$, it can be seen in the flexible TE case that there is a clockwise rotating vortex entrapped between the airfoil and the LEV. Because the TE segment is almost aligned with the streamwise flow, the flow from the upper surface of the airfoil loses a significant amount of its streamwise momentum as it turns around

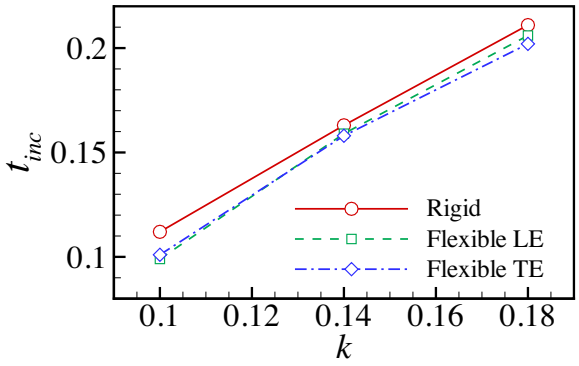

Figure 4.10: Estimate of the LEV inception time (normalized by oscillation period) versus reduced frequency for the rigid, flexible LE and flexible TE airfoils.

the trailing edge. In fact, much of the flow reversal around the trailing edge for the flexible TE case is caused by flow entrainment of the LEV. The evidence for this is supported by Fig. 4.9 where the streamwise velocity contours are shown for the three different cases at $t/T = 0.45$. As the relatively slow moving flow reversal travels upstream toward the airfoil leading edge, it eventually interacts with the separated leading edge shear layer to form a saddle-point. At the saddle point, the flow traveling upstream from the trailing edge bifurcates and it either gets entrained by the shear layer or it travels upstream and upward toward the airfoil surface. Since flow reversal of the flexible TE case has relatively small streamwise momentum and therefore cannot travel upstream for long, it eventually begins to roll to form a clockwise rotating secondary vortex.

4.3.3 Inception of the leading edge vortex

We have briefly mentioned above that increasing the reduced frequency delays the inception/formation of the LEV. The mechanism leading to LEV inception occurs at the boundary-layer scale, which we cannot resolve using the current experimental set-up. However we can approximate the time scale of the inception visually, by noting the time at which a small vorticity bubble begins to form on the airfoil. Fig.

4.10 shows the approximated LEV inception time scale, t_{inc} (normalized by the oscillation period), versus reduced frequency for the rigid, flexible LE and flexible TE airfoils. As can be clearly seen, the inception time seems to be approximately linearly increasing with k, where the deforming leading and trailing edge airfoils slightly reduce the inception time of the LEV. This delay in LEV inception is actually a result of the decrease in vorticity flux at the airfoil surface with increasing k. The vorticity flux from the airfoil surface is proportional to the shear layer velocity near the airfoil leading edge, U_{SL} (Wong & Rival, 2015). The rate of vorticity/circulation growth of the LEV can be approximated as (Eldredge & Jones, 2019):

$$\frac{d\Gamma_{LEV}}{dt} = -\frac{1}{2}U_{SL}^2 \tag{4.3.2}$$

where Γ_{LEV} is the LEV circulation. We can approximate the shear layer velocity as the vector sum of the local velocity of the leading edge and the component of the free stream velocity in the direction of airfoil motion:

$$U_{SL} \approx U_\infty sin(\theta) - \dot{h}cos(\theta) - \frac{\dot{\theta}c}{2} \tag{4.3.3}$$

In Fig. 4.11a, the flow velocity at the leading edge normalized by the maximum airfoil tip velocity is shown for $k = 0.10$, 0.14 and 0.18. As can be clearly seen, the shear layer velocity decreases with increasing k. Consequently, the smaller vorticity flux at higher k values delays the LEV inception time. It is also interesting to point out that the LEV inception time scale shown in Fig. 4.10 coincides with the time at which the non-dimensional leading edge velocity is approximately equal to 0.5 for all the reduced frequencies that we test. Furthermore, we can also approximate the leading edge tip velocity for the flexible LE airfoil, $U_{SL_{Flexible}}$, as follows:

$$U_{SL_{Flexible}} \approx U_\infty sin(\theta) - \dot{h}cos(\theta) - \frac{\dot{\theta}c}{2} - \frac{c\dot{\alpha}_{LE}}{3} \tag{4.3.4}$$

where the additional term, $c\dot{\alpha}_{LE}/3$, represents the leading edge tip velocity. The

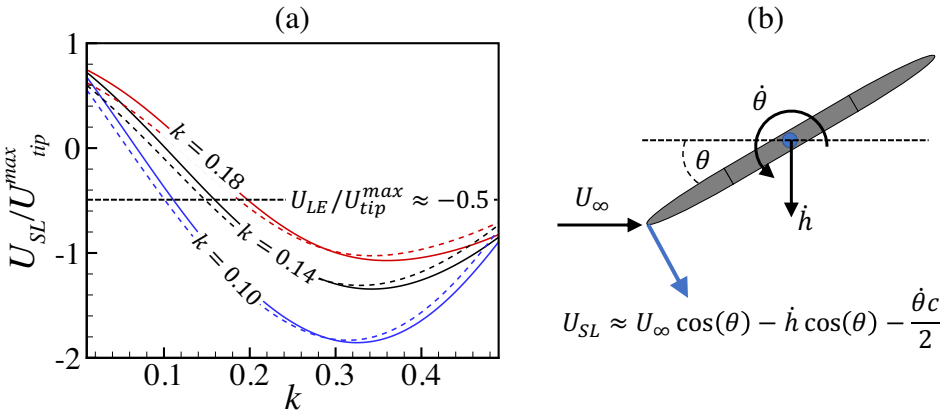

Figure 4.11: (a) Normalized shear layer velocity at the leading edge for $k = 0.10$-0.18. The solid lines represent the velocity of the rigid airfoil and the dashed lines represent velocity of the flexible LE airfoil. (b) Sketch of the velocity vectors used to approximate U_{SL}

approximate shear layer velocity of the flexible LE airfoil is also shown in Fig. 4.11a (dashed lines). We can see that the motion of the deforming leading edge segment slightly increases the shear layer velocity during the first half of the down-stroke. Interestingly, the timing of the non-dimensional velocity $U_{SL}/U_{tip}^{max} \approx -0.5$ also coincides with the timing of the LEV inception for the flexible LE. Note that while the flexible TE has a rigid leading edge, its LEV inception time is also shown to decrease relative to the rigid airfoil. We believe that this is associated with the enhanced effective camber provided by the deformed trailing edge, which could accelerate the flow at the leading edge to yield a larger U_{SL} than the rigid airfoil.

The implication of this discussion is that the non-dimensional shear layer velocity can be used to approximate the inception time of the LEV, which may be of great importance in developing potential flow-based models of oscillating airfoils undergoing dynamic stall (Ramesh *et al.*, 2014).

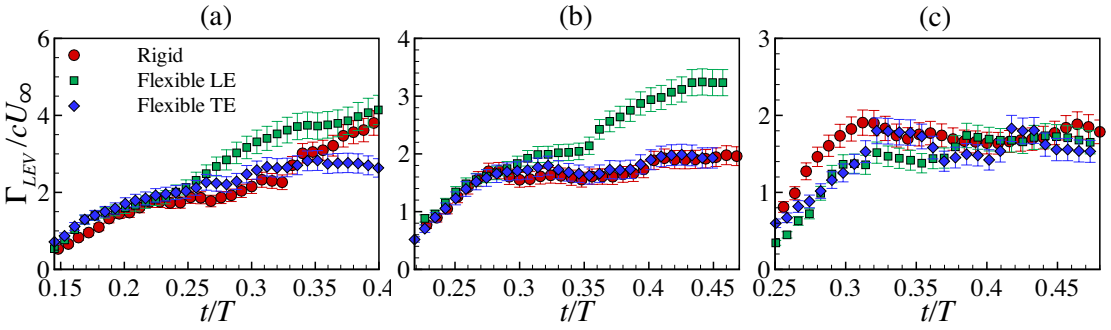

Figure 4.12: Time-history of the non-dimensional LEV circulation for rigid, flexible LE and flexible TE airfoils at (a) $k = 0.10$, (b) $k = 0.14$ and (c) $k = 0.18$. For clarity, only every other data point is shown.

4.3.4 Effects of surface deformation on leading edge vortex evolution

It is well known that the circulation generated by airfoils is a manifestation of the momentum imparted to the flow field and therefore is directly related to the production of aerodynamic forces. Here, we analyze the role of deforming LE and TE on the time-history of LEV circulation. To determine the boundaries of LEVs, we use the γ_2 method proposed by Graftieaux *et al.* (2001), which is given by:

$$\gamma_2(P) = \frac{1}{S_A}\int_{M\in S_A} \frac{[\mathbf{PM}\times(\mathbf{U_M}-\overline{\mathbf{U}}_\mathbf{P})]\cdot n_z}{||\mathbf{PM}||\cdot||\mathbf{U_M}-\overline{\mathbf{U}}_\mathbf{P}||}dS_A \tag{4.3.5}$$

where S_A is the area of integration, $\mathbf{P}$ is any point in the flow field, $\mathbf{M}$ is any point within the integration area, $\overline{\mathbf{U}}_\mathbf{P}$ is the average velocity within the integration area, $\overline{\mathbf{U}}_\mathbf{M}$ is the velocity of point M in the integration area, $\mathbf{PM}$ is the distance between $\mathbf{P}$ and $\mathbf{M}$ and n_z is the normal vector in the z direction. The vortex boundary is given by $|\gamma_2| = 2/\pi$. The LEV circulation, Γ_{LEV}, can then be computed by integrating the vorticity enclosed by the contour level of $|\gamma_2| = 2/\pi$:

$$\Gamma_{LEV} = \int_{|\gamma_2|=2/\pi} \omega_z dA \tag{4.3.6}$$

where ω_z is the spanwise vorticity. As stated previously, it is not possible to determine the LEV strength as soon as it initiates due to the inability to resolve the boundary-layer scale with the current experimental setup, and therefore we only report the circulation once sufficient development occurs for the γ_2 method to capture the LEV. LEVs are then tracked until they begin to convect downstream outside of the control volume.

The LEV circulation, non-dimensionalized by the free stream velocity and airfoil chord length, is shown in Fig. 4.12 for $k = 0.10$, 0.14 and 0.18. As the LEV forms, it grows in strength as it entrains vorticity from the leading edge shear layer. Therefore, the shear layer strength is a crucial parameter in determining the LEV circulation, as well as the rate of circulation growth. It is shown for $k = 0.10$ that the LEV of the flexible LE airfoil grows, on average, at a faster rate than the LEV of the rigid and flexible TE airfoils. This is attributed to the stronger shear layer generated by the larger camber created by the deforming LE segment. Furthermore, the LEV keeps increasing in strength until it is detached from the feeding shear layer. Different mechanisms of LEV detachment in flapping airfoils have been proposed by Widmann & Tropea (2015). In one of the mechanisms, which they refer to as bluff-body-like vortex detachment, the flow reversal from TEVs that travels upstream towards the leading edge interacts with the feeding shear layer to decrease its velocity, such that it no longer keeps up with the downstream convecting LEV. At $k = 0.10$, where TEVs do form, the LEV for both the rigid and flexible LE keeps increasing in strength until it reaches a maximum value of approximately $\Gamma_{LEV}/cU_\infty \approx 4$ at $t/T \approx 0.40$. This time approximately coincides with the formation time of the TEV, which indicates that bluff-body-like vortex detachment is the mechanism responsible of LEV detachment from its shear layer for the rigid and flexible LE airfoils. On the other hand, the flexible TE airfoil is shown to peak at $t/T \approx 0.35$, at a much lower circulation value of $\Gamma_{LEV}/cU_\infty \approx 3$. Because the flexible TE case suppresses the formation of the TEV, there must be another mechanism that is responsible for cutting-off the vorticity supply to the LEV. We suspect that the LEV is detached as a result

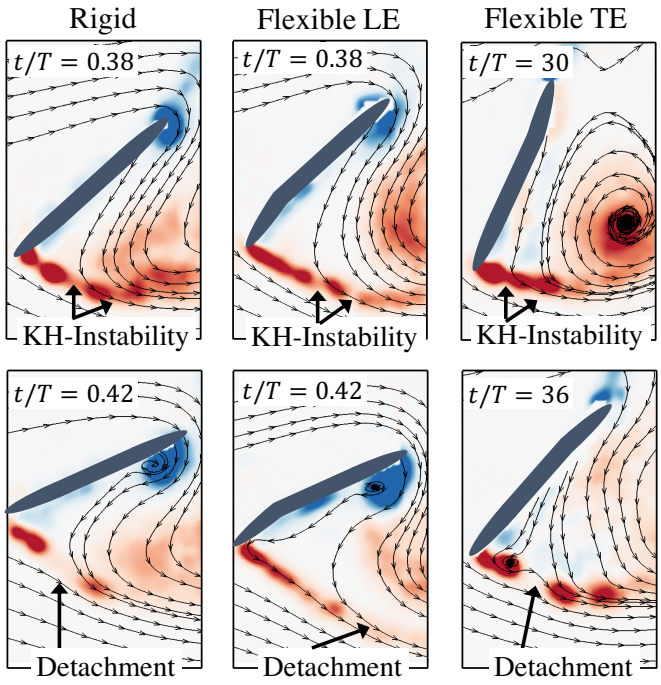

Figure 4.13: Detachment process of the LEV from its feeding shear layer at $k = 0.10$. (Top) Zoomed-in view of vorticity field shortly prior to LEV detachment and (bottom) zoomed-in view of vorticity field after LEV detachment.

of the interaction of the boundary layer with the feeding shear layer, in a process known as the boundary layer eruption (Doligalski *et al.*, 1994; Widmann & Tropea, 2015). In this process, the interaction of the LEV with the airfoil surface induces an adverse pressure gradient in a local region inside the boundary layer. As a result, the fluid elements in this region are compressed in the streamwise direction and consequently, a thin fluid layer is squeezed up from the interior of the boundary layer that erupts the shear layer, eventually cutting off the vorticity supply to the LEV. With the current experimental setup, we are unable to resolve this mechanism since it occurs at the boundary layer scale. However, regardless of the exact mechanism of LEV detachment, one can anticipate the onset of LEV detachment by closely examining the behavior of the feeding shear layer. Shortly

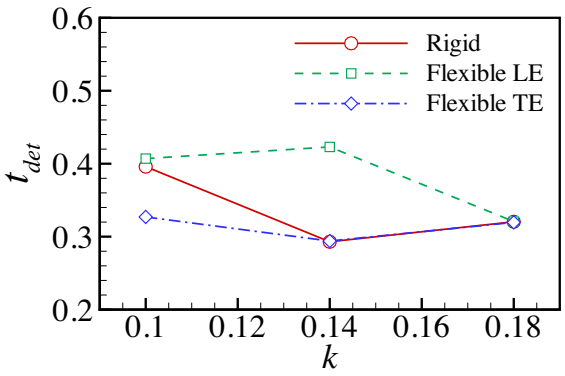

Figure 4.14: Estimate of the LEV detachment time (normalized by oscillation period) versus reduced frequency for the rigid, flexible LE and flexible TE airfoils.

prior to detachment, a Kelvin-Helmholtz-like (KH) instability in the shear layer is observed, where the shear layer begins to roll into discrete vortical structures and eventually gets disconnected from the LEV. This process is demonstrated in Fig. 4.13.

By increasing the reduced frequency to $k = 0.14$ (shown in Fig. 4.12b), the LEV circulation for the flexible TE and rigid airfoils follow the same trend, where they both peak at $\Gamma_{LEV}/cU_\infty \approx 2$ at $t/T \approx 0.30$. On the other hand, the flexible LE airfoil is shown to increase the LEV circulation until $t/T \approx 0.45$, with a maximum circulation of $\Gamma_{LEV}/cU_\infty \approx 3$. We believe that this is again related to the enhanced shear layer strength of the flexible LE airfoil. Future studies that include high-resolution investigation of the shear layer velocity will be conducted to better understand the shear-layer enhancement process. Finally in Fig. 4.12c, the LEV circulation is shown for $k = 0.18$. For all three cases, the time-history of LEV circulation is shown to follow a similar trend to $k = 0.14$ (except for the flexible LE case), where surface deformation has no effect on the circulation. For all cases, the LEV reaches a peak value of approximately $\Gamma_{LEV}/cU_\infty \approx 2$ at $t/T \approx 0.325$. For completeness, the time scale of LEV detachment from its feeding shear layer is plotted in Fig. 4.14 as a function of the reduced frequency. The detachment time scale, t_{det}, is defined as the time at which the LEV circulation becomes constant.

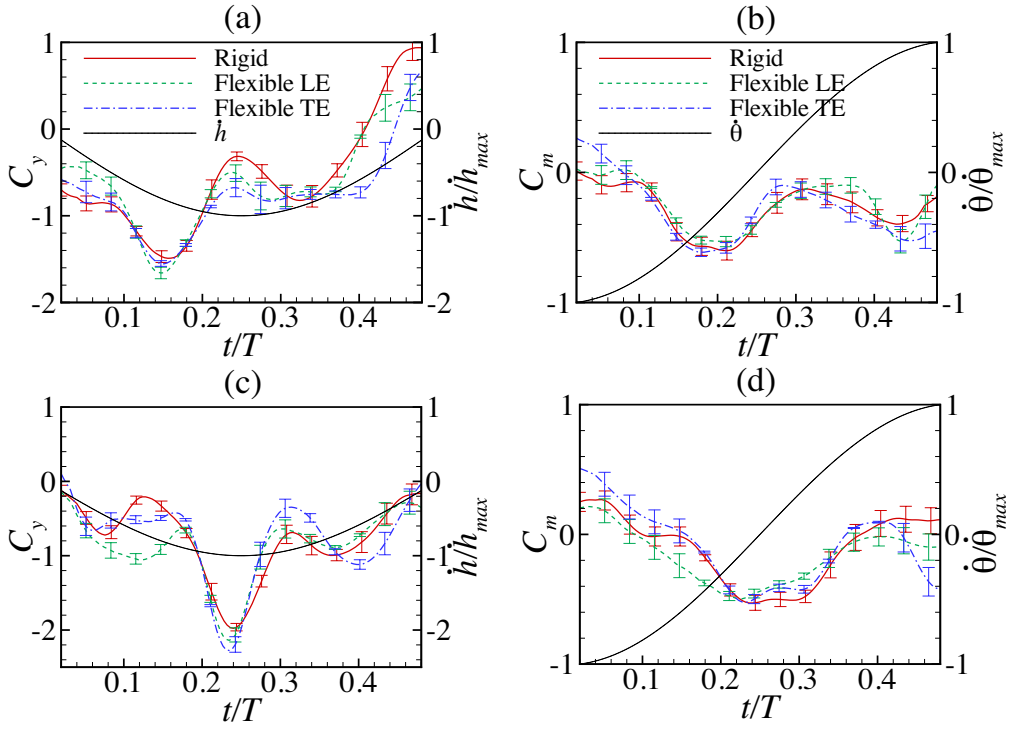

Figure 4.15: Vertical force and pitching moment coefficients for (a,b) $k = 0.10$ and (c,d) $k = 0.14$. The dotted line represents the heaving and pitching velocities.

4.3.5 Impulse-based force and moment evaluation

The vertical component of force coefficient ($C_y = 2F_y/\rho U_\infty^2 c$) and spanwise moment coefficient ($C_m = 2M_z/\rho U_\infty^2 c^2$) are shown in Fig. 4.15 for $k = 0.10$ and 0.14. The heaving and pitching velocities of the airfoil are also shown. For $k = 0.10$, the flexible LE and TE airfoils are shown to increase the peak force by 14.7% and 12.7% relative to the rigid airfoil, respectively. The peak moment coefficient occurs slightly after the peak forces are produced. After its formation, the LEV remains near the upstream portion of the airfoil, which results in generating a negative, counter-clockwise pitching moment. The peak moment coefficient does not seem to be greatly influenced by the airfoil deformation. The force and moment coefficients

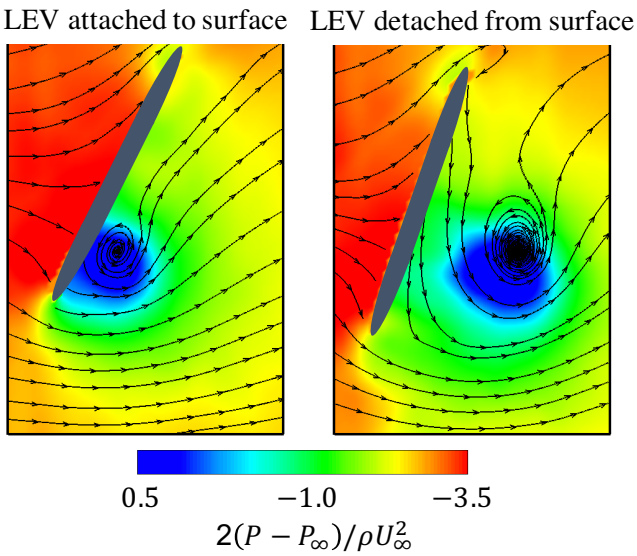

Figure 4.16: Zoomed-in view of the pressure contour and streamlines at $k = 0.10$ showing an attached and detached LEV from the airfoil surface.

then begin to decrease as a result of the LEV lifting-off from the airfoil surface. Even though the LEV strength and size are actually increasing during this phase, its influence on the force and moment subsides as the low pressure region that it creates moves away from the airfoil surface. To illustrate this effect, the pressure field is provided in Fig. 4.16 for the rigid airfoil.

Furthermore, at approximately the mid-downstroke, the flexible TE airfoil is shown to produce the largest force, followed by the flexible LE and then the rigid airfoils. After reaching a local minima, both the force and moment coefficients begin to slightly increase. Siala & Liburdy (2019*b*) have previously shown that this increase in the forces is associated with the advection of the LEV along the airfoil chord. Shortly after the secondary peak, the force coefficient for the rigid and flexible TE drops rapidly, eventually switching sign at $t/T \approx 0.40$ (negative lift). On the other hand, the drop in lift force is shown to delay to $t/T \approx 0.42$ for the flexible TE airfoil. This is because the flexible TE airfoil suppresses the

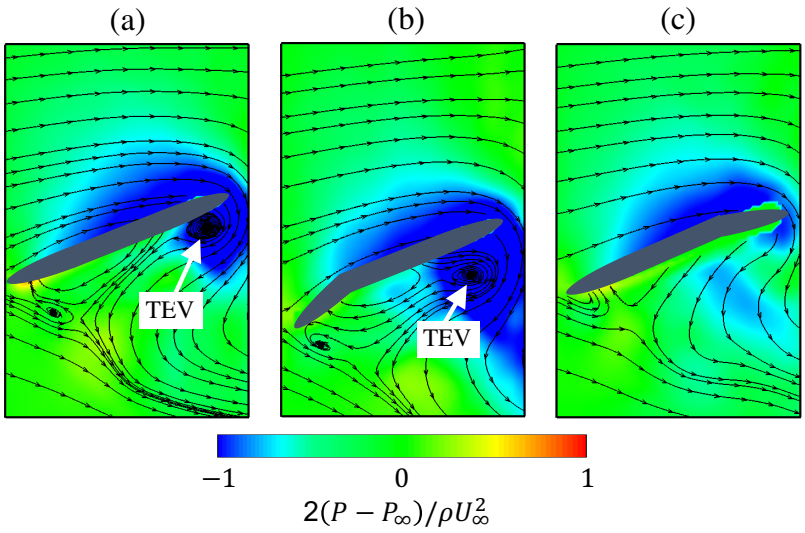

Figure 4.17: Zoomed-in view of the pressure distribution and streamlines for $k = 0.10$ at $t/T = 0.45$ for (a) rigid, (b) flexible LE and (c) flexible TE airfoils.

formation of TEV, thereby delaying its negative effects on the force coefficient. Moreover, the moment coefficients for the rigid and flexible LE airfoils approach $C_m \approx 0$ towards the end of the cycle, whereas for the flexible TE case, the moment coefficient remains relatively large and negative. Again, this is a result of the large TEV forming and rolling on the lower surface of the trailing edge for the rigid and flexible LE case. The pressure distribution for all three cases at $t/T = 0.45$ is shown in Fig. 4.17. For the rigid and flexible LE airfoils, the low pressure region created by the rolled TEV seems to be well balanced by the low pressure region on the upper surface of the airfoil, thus creating a relatively small pressure differential across the two surfaces. Conversely, the low pressure region on the top surface of the flexible TE airfoil is much lower than the pressure on the bottom surface. Since the low pressure region is concentrated in the downstream half of the airfoil, a negative counter-clockwise moment is generated.

As k is increased to 0.14, it can be seen that the peak force coefficient is delayed to slightly before mid-downstroke for all three cases. Similar to $k = 0.10$, the peak

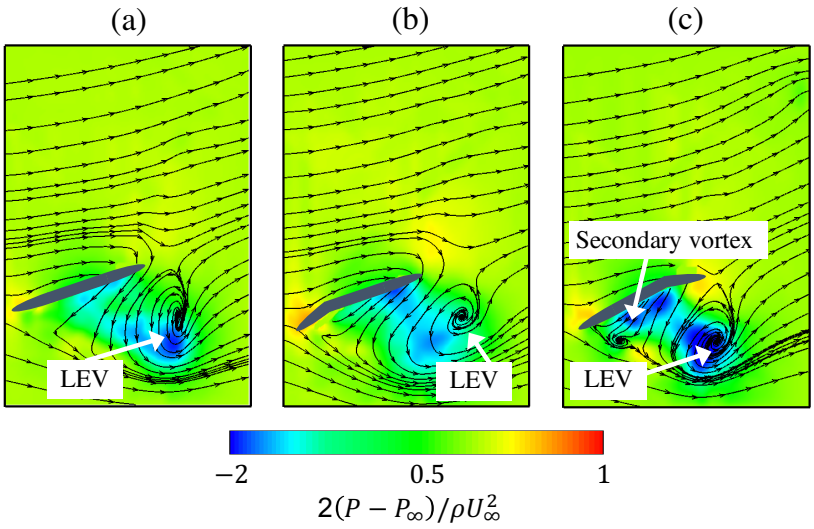

Figure 4.18: Pressure distribution and streamlines for $k = 0.14$ at $t/T = 0.45$ for (a) rigid, (b) flexible LE and (c) flexible TE airfoils.

force is shown to be enhanced by the surface deformation, with the flexible TE airfoil generating a slightly larger peak than the flexible LE airfoil. At this reduced frequency, the magnitude of peak force plays a much larger role in power generation than for $k = 0.10$, since its timing is well correlated with the timing of maximum heaving velocity. Furthermore, the effect of airfoil deformation remains minimal and less obvious on the peak moment coefficient. It can be anticipated that the magnitude of peak moment does not play an important role in power generation, since at this k value, it occurs when the pitching velocity is quite small. Toward the end of the downstroke, it can be seen that the flexible TE case generates a large negative moment relative to the rigid and flexible LE cases. This can be explained by examining the pressure distribution around the airfoil in Fig. 4.18. As a result of the secondary vortex that forms by the flexible TE airfoil near the leading edge, a low pressure zone is created that results in a negative counter-clockwise moment about the pitching axis. This low pressure region is not produced by the rigid and flexible LE airfoils.

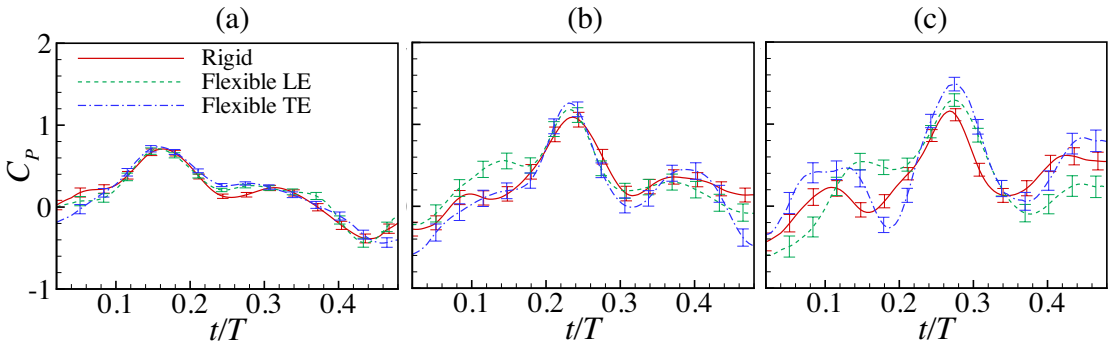

Figure 4.19: Power coefficient of the rigid, flexible LE and flexible TE airfoils for (a) $k = 0.10$, (b) $k = 0.14$ and (c) $k = 0.18$.

4.3.6 Energy harvesting performance

In Fig. 4.19, we report the instantaneous power coefficient of the rigid, flexible LE and flexible TE airfoils for $k = 0.10$, 0.14 and 0.18. The power coefficient is defined as:

$$C_P = \frac{P}{1/2\rho U_\infty^3 c} \tag{4.3.7}$$

where P is given in Eq. 4.1.1. At $k = 0.10$, the effect of leading/trailing edge deformation on power output is shown to be insignificant. For all cases, the power output has a positive sign throughout the majority of the downstroke, and becomes negative when $t/T > 0.4$. As k is increased to 0.14 and 0.18, the airfoil deformation begins to have a more pronounced effect. Early in the downstroke, the power output for all cases is shown to be negative, because the moment coefficient and pitching velocity have a negative correlation. Significantly enhanced peak powers are generated for all cases compared to $k = 0.10$, with the flexible TE and LE airfoils producing a slightly higher maximum power than the rigid airfoil.

The energy harvesting efficiency is defined as the ratio of mean power output

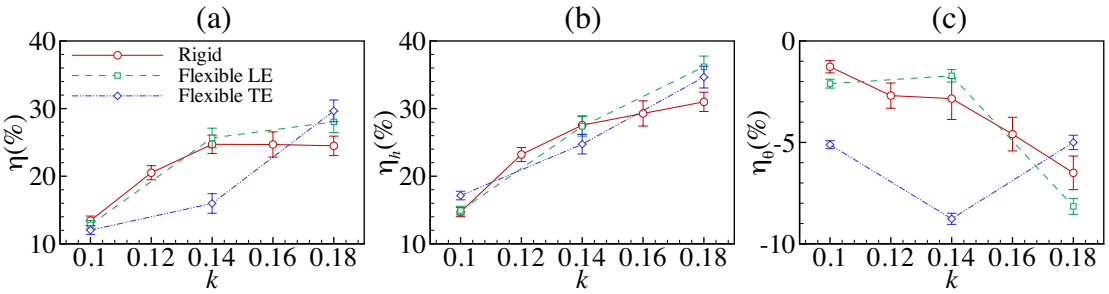

Figure 4.20: (a) Total energy harvesting efficiency, (b)heaving contribution and (c) pitching contribution versus reduced frequency.

to the available fluid power in the swept area of the airfoil:

$$\eta = \frac{\overline{P}}{1/2\rho U_\infty^3 d} \tag{4.3.8}$$

where $\overline{P}$ is the cycle-averaged power and d is the total crossflow distance swept by the airfoil. In addition, the energy harvesting efficiency can be decomposed into contributions of heaving and pitching motions as follows:

$$\eta_h = \frac{\overline{F_y \dot{h}}}{1/2\rho U_\infty^3 d} \tag{4.3.9}$$

$$\eta_\theta = \frac{\overline{M_z \dot{\theta}}}{1/2\rho U_\infty^3 d} \tag{4.3.10}$$

The total energy harvesting efficiency, and the contributions of the heaving and pitching motions are shown in Fig. 4.20 as a function of reduced frequency. Note that two additional points are included for the rigid airfoil at $k = 0.12$ and $k = 0.16$ from a previous study (Siala & Liburdy, 2019*c*). At $k = 0.10$, it is shown in Fig. 4.20(a) that airfoil deformation at the leading and trailing edges slightly decrease the total energy harvesting efficiency compared to the rigid airfoil. The rigid airfoil produces power at an efficiency of 13.5%, whereas the flexible LE and

TE operate at $\eta = 12.9\%$ and $\eta = 12.4\%$, respectively. While the contribution of heaving motion of the flexible TE airfoil is larger than the rigid and flexible TE airfoils, its pitching contribution is slightly more negative, as shown in Fig. 4.20(b) and 4.20(c), respectively. This is consistent with the results obtained by Totpal *et al.* (2018), who have shown that at low reduced frequencies, surface deformation decreases the energy harvesting efficiency. As k is increased to 0.14, the total energy harvesting efficiency for the rigid and flexible LE airfoils increase up to $\eta = 25.1\%$ and 25.9%, whereas the efficiency of the flexible TE airfoil is increased to only $\eta = 16.5\%$. The slow rate of increase in η with increasing k of the flexible TE is a result of the large negative pitching efficiency that it produces, as shown in Fig. 4.20(c). This is a result of the secondary vortex that is formed by the flexible TE airfoil, which generates a relatively large negative moment while it has a large positive pitching velocity. When k is increased to 0.18, the total efficiency for the rigid airfoil begins to slowly decrease. Although the heaving contribution increases when k is increased, the negative pitching contribution is increased from $\eta_\theta = -2.6\%$ to $\eta_\theta = -6.5\%$. This trend of negative increase in pitching contributions at high reduced frequencies has been reported by multiple authors in the literature (Kim *et al.*, 2017; Liu *et al.*, 2017). Furthermore, the flexible LE airfoil is shown to have a greater heaving contribution when compared to the rigid, while its pitching contribution is more negative than the rigid airfoil. On the other hand, the negative contribution of the pitching motion of flexible TE airfoil is shown to drop from $\eta_\theta = -8.1\%$ to $\eta_\theta = -4.9\%$ at $k = 0.14$ and $k = 0.18$, respectively, which results in a greater overall efficiency at $k = 0.18$ compared to the flexible LE airfoil. The shift to higher reduced frequency for peak efficiency for both flexible LE and TE compared to the rigid airfoil has also been observed by Liu *et al.* (2013).

4.4 Conclusions

The effects of inertia-induced deformation of the leading and trailing edges of the airfoil on the flow physics and power extraction performance of an oscillating energy

harvester were experimentally studied using wind tunnel testing. Two-dimensional particle image velocimetry measurements were conducted at reduced frequencies of $k = 0.10$, 0.14 and 0.18, with pitching and heaving amplitudes fixed at $\theta_0 = 75°$ and $h_0 = 0.6c$, respectively. The velocity data from the particle image velocimetry measurements were used to analyze the dynamics of the leading edge vortex, as well as to calculate force and pitching moment using the vortex-impulse theory.

The results show that the evolution of the leading edge vortex is altered by using a deforming airfoil surface. The timing of the leading edge vortex inception was shown to be slightly shifted to earlier times during the oscillation cycle, thereby slightly shifting the force peaks to earlier times relative to the rigid airfoil. The deforming leading edge directly influences the initiation of the leading edge vortex by altering the flow conditions at the airfoil leading edge tip. On the other hand, the deforming trailing edge is believed to increase the effective camber of the airfoil, which also alters the flow at the leading edge. It is argued that for both cases, the vorticity flux from the leading edge is increased as a result of the enhanced flow at the leading edge of the airfoil. In addition, it was shown that the inception time of the leading edge vortex for both the rigid and flexible leading edge airfoils coincides with the time at which the non-dimensional shear layer velocity reaches a value of approximately 0.5. Furthermore, the time-history of the leading edge vortex was analyzed. The results show that deformation at the leading edge of the airfoil enhances the growth rate and maximum strength of the LEV at $k = 0.10$ and $k = 0.14$ compared to the rigid and flexible trailing edge airfoils, while for $k = 0.18$, the LEV circulation for all three cases is essentially identical. For both the flexible leading edge and rigid airfoils, the trailing edge shear layer was observed to roll-up into a large trailing edge vortex at $k = 0.10$, which is responsible for cutting-off the vorticity supply from the shear layer to the leading edge vortex, in a mechanism known in the literature as bluff-body vortex detachment. Conversely, the motion of the flexible trailing edge suppresses the formation of the trailing edge vortex, and the leading edge vortex is believed to be detached from its shear layer via the boundary layer eruption mechanism. When $k > 0.10$, none of the airfoils generate

a trailing edge vortex, and the boundary layer eruption mechanism is proposed to be responsible for cutting off the vorticity supply to the leading edge vortex.

The instantaneous power output and energy harvesting efficiency of the deforming leading and trailing edge airfoils were compared with the rigid airfoil. At $k = 0.10$, no performance enhancement was observed by the flexible leading and trailing edge airfoils compared to the rigid airfoil. However, they are shown to be more effective at $k = 0.18$, where the energy harvesting efficiency was shown to increase to 30% and 28%, respectively, compared to the 24% efficiency of the rigid airfoil. The rigid airfoil efficiency is shown to peak at $k = 0.14$, whereas both deforming airfoils peak at $k = 0.18$, agreeing quite well with results reported in the literature.

The results of this study experimentally validate the feasibility of using deforming airfoil surface to enhance the performance of oscillating energy harvesters. Future work will be conducted at larger reduced frequencies to determine the optimal operating reduced frequency of the flexible leading and trailing edge airfoils.

Acknowledgments

The authors would like to acknowledge the financial support provided by the Air Force Office of Scientific Research Under the MURI grant FA9550-07-1-0540 and the National Science Foundation CBET Award Number 1804964. Firas Siala also acknowledges the financial support from Link Energy Foundation Fellowship.

Chapter 5 Conclusions

This work focused on experimental investigations of the unsteady aerodynamics of a heaving and pitching airfoil operating in the energy harvesting regime. Two-dimensional particle image velocimetry (PIV) measurements were conducted in a recirculating wind tunnel at reduced frequencies of 0.06-0.18 with pitching and heaving amplitudes fixed at $\theta_0 = 75^\circ$ and $h_0 = 0.6c$, respectively. The velocity field data obtained from PIV was used to thoroughly study the flow physics qualitatively as well as quantitatively. A reduced-order model was developed from the vortex-impulse theory that can effectively estimate the aerodynamic loadings and hence energy harvesting performance of the oscillating airfoil using flow field data obtained from PIV. In addition, the feasibility of using inertia-induced surface deformation as a mechanism of energy harvesting enhancement was explored.

In Chapter 2, a reduced form of the vortex-impulse equation ~~was~~ developed and used to better understand force production mechanisms of an airfoil undergoing deep dynamic stall. It ~~was~~ shown that the finite-domain impulse-based force equation can be significantly simplified by selecting the origin location of the position vector to be located anywhere along downstream control volume boundary. By doing so, several complex surface integral terms were shown to become negligible and the impulse-based force equation was reduced to only two terms with a clear physical meaning: (i) the time rate of change of the impulse and (ii) the Lamb vector/Kutta Joukowski force that indirectly captures the effect of vortices in the far wake. The force estimate obtained from the model was validated against direct force measurement at low reduced frequencies. The results show that for $k = 0.06$-0.10, the time-history of the force contains two force peaks that form during the downstroke/upstroke motion of the airfoil. The primary peak is shown to be associated with the formation of the leading edge vortex (LEV) and its detachment from the airfoil surface and the secondary peak is generated as a result of its enhanced

chord-wise advection. As the reduced frequency is increased to $k \geq 0.12$, the time scale of airfoil motion decreases relative to the advective time scale, which allows the airfoil to capture the LEV that was shed in the previous cycle as it begins its downstroke/upstroke. Consequently, a third peak in the force is produced at these higher k values at the beginning of each stroke. Furthermore, it was demonstrated that when $k \leq 0.10$, the LEV grows quite rapidly and its maximum size scales with the airfoil chord length. As it grows past the airfoil trailing edge, the trailing edge shear layer was shown to roll-up into a large trailing edge vortex (TEV), resulting in a rapid drop in the aerodynamic force. The flow reversal from the TEV toward the airfoil leading edge cuts-off the vorticity supply from the leading edge shear layer to the LEV, resulting in a vortex shedding behaviour akin to bluff-bodies. On the other hand when $k \geq 0.12$, the relative rapid motion of the airfoil limits the growth of the LEV and consequently the end of the stroke is reached before the LEV approaches the airfoil trailing edge. As a result, the TEV formation is suppressed and the vortex detachment of the LEV from its shear layer is argued to be a result of the eruption of the boundary layer.

In Chapter 3, the energy harvesting performance was investigated. In order to calculate the power output and energy harvesting efficiency, the aerodynamic moment equation based on the vortex-impulse theory was derived. The maximum energy harvesting efficiency of approximately 25% was obtained at $k = 0.14$, agreeing very well with published numerical results. The relationship between the concept of optimal vortex formation number and maximum energy harvesting efficiency was then explored. The results show no established relationship between the two, and the maximum energy harvesting efficiency obtained at $k = 0.14$ was shown to be a result of the optimal match between the time scales of the LEV and airfoil oscillation. Furthermore, in order to better understand the effects of vortex structures on the energy harvesting performance, the power equation was decomposed into contributions of positive and negative vorticity (where the positive vorticity is associated with the counter-clockwise rotating LEV during the downstroke). It was demonstrated that the contribution of the negative vortic-

ity to the aerodynamic moment was primarily responsible for the reduction of the energy harvesting efficiency and power output for $k > 0.14$. Specifically, due to the larger advective time scale of the LEV at higher k values, the negative vorticity of the LEV generated during the upstroke was shown to be caught by the downstream portion of the airfoil as it begins its downstroke. As a result, a large counter-clockwise (negative) moment is produced, which interacts with the clock-wise rotating airfoil to produce a large negative power.

In Chapter 4, the effects of inertia-induced deformation of the leading and trailing edges of the airfoil on the flow dynamics and energy harvesting performance were investigated. The passive deformation of the leading/trailing edges was established by inserting a rod into slots along both the main airfoil body and the leading/trailing edge segments, forming a hinge. The rod was secured at one end on the body and the other end to the leading/trailing edge, providing a means to allow deformation of the leading/trailing edge. The results show that the LEV inception, growth and detachment are all affected by using a deforming airfoil surface. The deforming leading edge airfoil directly influences ~~feeding~~ shear layer and consequently the evolution of the LEV is altered. On the other hand, the deforming trailing edge introduces a camber that indirectly influences the flow conditions at the leading edge. Both forms of deformation were shown to increase the maximum energy harvesting efficiency at higher reduced frequencies. Relative to the rigid airfoil, the deforming leading and trailing edges increased the maximum efficiency by 17% and 25%, respectively. The performance enhancement was shown to be a result of increased effective angle of attack induced by the deforming surfaces. In addition, both forms of deformation were shown to operate most efficiently at $k = 0.18$ as opposed to $k = 0.14$ for the rigid airfoil. For the deforming leading edge, the performance enhancement was shown to be associated with enhanced heaving contribution, while the trailing edge deformation was shown to alleviate the negative pitching moment at $k = 0.18$, resulting in greater efficiency than the rigid airfoil.

Chapter 6 Implications and Future Work

The results presented in this dissertation can be of great importance in developing theoretical models of transient force production of oscillating airfoils undergoing deep dynamic stall. While there is an extensive amount of studies conducted that attempt to model the unsteady forces based on discrete vortex models (Ramesh *et al.*, 2014; Darakananda *et al.*, 2016; Prier, 2018; Wang & Eldredge, 2013) and classical unsteady thin airfoil theory (Brunton & Rowley, 2010; Li & Wu, 2015), various *ad-hoc* criteria and assumptions for the LEV inception time and detachment are used that limit their use to only specific cases. We believe that some of these assumptions can be loosened by some aspects that we have learned from this research.

Firstly, the inception/initiation of the LEV can potentially be determined based on solely the airfoil kinematics and free stream flow. Currently, the most widely used initiation criterion is based on the Leading Edge Suction Parameter (LESP) developed by Ramesh *et al.* (2014). The LESP is equivalent to the first Fourier coefficient A_0 in unsteady thin airfoil theory. Briefly, Ramesh *et al.* (2014) show that there exists a critical LESP value that is universal for a given airfoil geometry and Reynolds number which dictates the time at which the LEV formation is initiated. While this method is indeed effective, it requires high resolution simulations to pre-determine the onset of flow separation, because the critical LESP value is achieved when an unstable wall friction coefficient along the airfoil chord length is detected. Most PIV-based experiments cannot fully resolve the near wall boundary-layer due to laser reflection off the surface. We have shown in Chapter 4 that there seems to be a critical non-dimensional value of the shear layer velocity (approximated from the flow conditions at the leading edge tip of the airfoil), where the flow separation begins to occur. This can potentially be used to determine the onset of LEV initiation. That being said, there certainly needs to be more work

done in validating this concept using various airfoil kinematics and flow conditions. In addition, the shear layer must be resolved in order to accurately measure its velocity.

Secondly, we have shown that the time evolution of the LEV collapses on a single curve for a range of reduced frequencies when the LEV circulation and time are normalized by the chord length and shear layer velocity. This suggests that this scaling method may potentially serve as a tool to predict the evolution of LEVs for a wide range of reduced frequencies. However, more work is needed to verify this for a wider range of airfoil kinematics. Furthermore, the collapse of the circulation is only truly universal (for the kinematics conditions we tested) when the LEV detachment occurs as a result of TEV formation (i.e. bluff-body detachment). We have shown that when boundary-layer eruption occurs at $k \geq 0.12$, the LEV stops growing and no longer follows the curve of the lower reduced frequency range. We believe that it is possible to obtain a criterion that determines when boundary-layer eruption occurs. By acknowledging that the boundary-layer eruption mechanism occurs as a result of the increased streamwise pressure gradient near the airfoil surface (due to the interaction of the LEV with the surface), then it may be possible to determine a critical pressure gradient at which boundary-layer eruption occurs. The critical non-dimensional pressure gradient may potentially be obtained as follows. Near the airfoil surface, the pressure gradient can be written as:

$$\frac{dp}{dx} = \nu \frac{\partial^2 u}{\partial y^2} \tag{6.0.1}$$

By scaling the velocity as $u \sim \Gamma_{LEV}/(2\pi R)$, diffusive length scale as $y \sim L_y - R$ (where R is the LEV radius and L_y the normal distance from the LEV center to the airfoil surface) and the pressure gradient as $dp/dx \sim \rho U_{SL}^2/c$, the dimensionless pressure gradient becomes:

$$\frac{dp^*}{dx^*} = \frac{\hat{T}_{max}}{Re_{SL}} \frac{c^2}{\pi\kappa(L_y - R)^2} \tag{6.0.2}$$

where $\hat{T}_{max} = (\Gamma_{LEV}/cU_{SL})_{max}$ is the maximum circulation at the instant of LEV detachment from its shear layer, Re_{SL} is the Reynolds number based on the shear layer velocity and $\kappa = 2R/c$. Equation 6.0.2 may identify a transition criterion based on LEV formation and growth that results in a critical value of the non-dimensional pressure gradient. It is also revealed in this criterion that large chord lengths, c, increase the dimensionless pressure gradient and thereby trigger boundary-layer eruption. This is consistent with the findings of Widmann & Tropea (2015). In addition, this critical value of non-dimensional pressure gradient provides a means to examine relative parameters of LEV growth on the detachment process. For instance, the interpretation of the parameter $\hat{T}_{max}/Re_{SL}$ is that as the shear layer Reynolds number increases relative to the strength of the LEV (which if strong, viscous effects near the surface become critical), the shear layer is able to feed vorticity to the LEV at a relatively fast rate, such that the LEV will grow to the trailing edge, resulting in bluff-body detachment.

Lastly, we have shown in shown in Chapter 2 that the aerodynamic forces are dominated by the rate of change of vortex impulse and the Lamb vector that represents the contributions of the shed vortical structures in the far wake. The model, however, is only valid under the following conditions:

- For vertical/lift force calculation, the origin location of the position vector must be placed along the downstream boundary.
- The control volume is large enough in the cross-stream direction such that the majority of vorticity leaves the control volume through the downstream boundary.
- The downstream boundary of the control volume must be located at least 1 chord length away from the airfoil trailing edge.
- Significant amount of flow separation is present.

The first condition is thoroughly discussed in Chapter 2 for vertical/lift force calculation. However, for drag calculation, which we do not consider in this dissertation,

another objective origin location that minimizes the amplified error due to the position vector may be required. Furthermore, the second condition is required so that all the impulse flux terms in the original impulse equation (Noca, 1997) are only computed at the downstream boundary (which will go to zero if the origin location is placed at the downstream boundary). The reasoning of the third condition is currently not clear. However, we speculate that the control volume should be large enough such that the LEV remains inside the control volume while it is growing in size and strength. If an LEV leaves the control ~~white~~ it is still growing, then it may be possible that the Lamb vector force does not pick up the contributions of rate of change of circulation on the force. It was demonstrated in Chapter 2 that the force calculations begin to converge as the downstream boundary of the control volume approaches a value of one chord length away from the airfoil trailing edge. Finally, the fourth condition is required because the vorticity must be well resolved in order for the impulse-based calculations to be accurate. When the flow is fully-attached such that all the vorticity is confined in the boundary-layer (which is not easy to capture using PIV), the impulse-based approach will yield inaccurate results. While there are studies in the literature that prove that surface vorticity plays a negligible role in force production of an airfoil undergoing deep dynamic stall (Moriche *et al.*, 2017), there are times during the beginning of oscillation cycle (albeit a small percentage of the total time) where the flow seems to be fully-attached. Our direct force measurements at $k = 0.06$ an 0.08 show that the impulse-based force evaluation under-predicts the force when the flow is fully attached. However, calculating the mean forces, power output and energy harvesting efficiency using the impulse-based model and direct force measurements essentially yields similar results. That being said, it is encouraged to determine a method to either better resolve the surface vorticity or directly calculate the bound circulation contribution to the forces. The former can be done by using a transparent airfoil to limit laser reflection off the surface such that the flow near the wall can be better resolved. Directly measuring the bound vorticity, however, is not a trivial task and is currently under extensive research (Corkery *et al.*, 2019).

APPENDICES

Appendix A Derivation of the impulse-based force and moment equations

In this section, we will show a step-by-step derivation of the impulse-based force and moment equations. Both equations are derived based on the standard conservation of momentum and conservation of angular momentum equations, combined with various vector calculus identities. Throughout the derivation, we assume that the flow is incompressible, the body surface is impermeable and the control volume is stationary.

A.1 Impulse-based force equation

Consider the follow form of the conservation of momentum equation for a finite, stationary control volume (CV), bounded by an exterior surface S, as shown in Fig. A.1:

$$\mathbf{F} = -\rho\frac{d}{dt}\int_{CV}\mathbf{u}dV - \oint_S \mathbf{n}\cdot(\rho\mathbf{u}\otimes\mathbf{u})dS + \oint_S \mathbf{n}\cdot(-p\underline{\mathbf{I}} + \underline{\mathbf{T}})dS \tag{A.1.1}$$

The first term can be written in terms of the vorticity using the *derivative-moment transformation* (DMT) identity (Wu *et al.*, 2007*b*):

$$\int_{CV}\mathbf{u}dV = \frac{1}{N-1}\int_{CV}\mathbf{x}\times(\nabla\times\mathbf{u})dV - \frac{1}{N-1}\oint_S \mathbf{x}\times(\mathbf{n}\times\mathbf{u})dS - \frac{1}{N-1}\oint_{S_B}\mathbf{x}\times(\mathbf{n}\times\mathbf{u})dS \tag{A.1.2}$$

where S_B represents the surface of the body located within the control volume CV. By recognizing that $\boldsymbol{\omega} = \nabla\times\mathbf{u}$, Eq. A.1.2 can be re-written as follows:

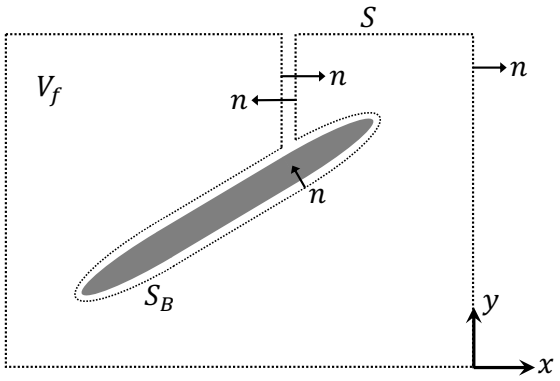

Figure A.1: Control volume used to derive impulse-based equations.

$$\int_{CV} \mathbf{u} dV = \frac{1}{N-1} \int_{CV} \mathbf{x} \times \boldsymbol{\omega} dV - \frac{1}{N-1} \oint_S \mathbf{x} \times (\mathbf{n} \times \mathbf{u}) dS - \frac{1}{N-1} \oint_{S_B} \mathbf{x} \times (\mathbf{n} \times \mathbf{u}) dS \quad \text{(A.1.3)}$$

The first term of Eq. A.1.1 can be replaced by Eq. A.1.3 to yield the following:

$$\mathbf{F} = -\frac{\rho}{N-1} \frac{d}{dt} \int_{CV} \mathbf{x} \times \boldsymbol{\omega} dV + \frac{\rho}{N-1} \frac{d}{dt} \oint_S \mathbf{x} \times (\mathbf{n} \times \mathbf{u}) dS + \frac{\rho}{N-1} \frac{d}{dt} \oint_{S_B} \mathbf{x} \times (\mathbf{n} \times \mathbf{u}) dS - \oint_S \mathbf{n} \cdot (\rho \mathbf{u} \otimes \mathbf{u}) dS + \oint_S \mathbf{n} \cdot (-p\underline{\mathbf{I}} + \underline{\mathbf{T}}) dS \quad \text{(A.1.4)}$$

The time derivative of the second term can be taken inside the integral:

$$\frac{\rho}{N-1} \frac{d}{dt} \oint_S \mathbf{x} \times (\mathbf{n} \times \mathbf{u}) dS = \frac{1}{N-1} \oint_S \mathbf{x} \times \big(\mathbf{n} \times \rho \frac{\partial \mathbf{u}}{\partial t}\big) dS \quad \text{(A.1.5)}$$

The time derivative of the velocity in Eq. A.1.5 can be evaluated through the use of the Navier-Stokes equations:

$$\rho\frac{\partial \mathbf{u}}{\partial t} = -\nabla p - \rho\mathbf{u}\cdot\nabla\mathbf{u} + \nabla\cdot\underline{\mathbf{T}} \tag{A.1.6}$$

In addition, another useful vector identity can be used to manipulate the convective acceleration term $(\mathbf{u}\cdot\nabla\mathbf{u})$ is:

$$\mathbf{u}\cdot\nabla\mathbf{u} = \nabla\big(\frac{1}{2}\mathbf{u}\cdot\mathbf{u}\big) - \mathbf{u}\times\boldsymbol{\omega} \tag{A.1.7}$$

Now insert Eq. A.1.7 into Eq. A.1.6:

$$\rho\frac{\partial \mathbf{u}}{\partial t} = -\nabla p - \rho\nabla\big(\frac{1}{2}\mathbf{u}\cdot\mathbf{u}\big) + \rho\mathbf{u}\times\boldsymbol{\omega} + \nabla\cdot\underline{\mathbf{T}} \tag{A.1.8}$$

Equation A.1.8 can now be inserted in Eq. A.1.5 to yield the following:

$$\frac{1}{N-1}\oint_S \mathbf{x}\times\big(\mathbf{n}\times\rho\frac{\partial\mathbf{u}}{\partial t}\big)dS = \frac{1}{N-1}\oint_S \mathbf{x}\times\Big(\mathbf{n}\times[-\nabla(p+\frac{\rho}{2}\mathbf{u}\cdot\mathbf{u}) + \rho\mathbf{u}\times\boldsymbol{\omega} + \nabla\cdot\underline{\mathbf{T}}]\Big)dS \tag{A.1.9}$$

The integral that involves the pressure can be transformed using another useful identity provided by (Noca, 1997), which he refers to as the pressure identity:

$$\oint_S \mathbf{x}\times\Big(\mathbf{n}\times[-\nabla(p+\frac{\rho}{2}\mathbf{u}\cdot\mathbf{u})]\Big)dS = (N-1)\oint_S \mathbf{n}\cdot(p+\frac{\rho}{2}\mathbf{u}\cdot\mathbf{u})\underline{\mathbf{I}}dS \tag{A.1.10}$$

Now, insert Eq. A.1.10 back into Eq. A.1.9:

$$\frac{1}{N-1}\oint_S \mathbf{x}\times\big(\mathbf{n}\times\rho\frac{\partial\mathbf{u}}{\partial t}\big)dS = \oint_S \mathbf{n}\cdot(p+\frac{\rho}{2}\mathbf{u}\cdot\mathbf{u})\underline{\mathbf{I}}dS + \frac{1}{N-1}\oint_S \mathbf{x}\times\Big(\mathbf{n}\times[\rho\mathbf{u}\times\boldsymbol{\omega} + \nabla\cdot\underline{\mathbf{T}}]\Big)dS \tag{A.1.11}$$

The last term of Eq. A.1.11 is separated as follows:

$$\frac{1}{N-1}\oint_S \mathbf{x}\times\big(\mathbf{n}\times[\rho\mathbf{u}\times\boldsymbol{\omega}+\nabla\cdot\underline{\mathbf{T}}]\big)dS = \frac{1}{N-1}\oint_S \mathbf{x}\times\big(\mathbf{n}\times[\rho\mathbf{u}\times\boldsymbol{\omega}]\big)dS + \frac{1}{N-1}\oint_S \mathbf{x}\times\big(\mathbf{n}\times\nabla\cdot\underline{\mathbf{T}}\big)dS \quad \text{(A.1.12)}$$

The first term on the right hand side is now re-written as:

$$\rho\oint_S \mathbf{x}\times\big(\mathbf{n}\times[\rho\mathbf{u}\times\boldsymbol{\omega}]\big)dS = \rho\oint_S[\mathbf{n}\cdot\boldsymbol{\omega}\otimes(\mathbf{x}\times\mathbf{u})-\mathbf{n}\cdot\mathbf{u}\otimes(\mathbf{x}\times\boldsymbol{\omega})]dS \quad \text{(A.1.13)}$$

Similarly, the second term on the right hand side of Eq. A.1.12 is re-written as:

$$\oint_S \mathbf{x}\times\big(\mathbf{n}\times\nabla\cdot\underline{\mathbf{T}}\big)dS = \oint_S[\mathbf{n}\cdot(\mathbf{x}\cdot\nabla\cdot\underline{\mathbf{T}})\underline{\mathbf{I}}-(\mathbf{x}\cdot\mathbf{n})\nabla\cdot\underline{\mathbf{T}}]dS \quad \text{(A.1.14)}$$

Now, Eq. A.1.13 and Eq. A.1.14 are inserted into Eq. A.1.11:

$$\frac{1}{N-1}\oint_S \mathbf{x}\times\big(\mathbf{n}\times\rho\frac{\partial\mathbf{u}}{\partial t}\big)dS = \oint_S \mathbf{n}\cdot(p+\frac{\rho}{2}\mathbf{u}\cdot\mathbf{u})\underline{\mathbf{I}}dS + \frac{\rho}{N-1}\Big[\oint_S[\mathbf{n}\cdot\boldsymbol{\omega}\otimes(\mathbf{x}\times\mathbf{u})-\mathbf{n}\cdot\mathbf{u}\otimes(\mathbf{x}\times\boldsymbol{\omega})]dS+\oint_S[\mathbf{n}\cdot(\mathbf{x}\cdot\nabla\cdot\underline{\mathbf{T}})\underline{\mathbf{I}} - (\mathbf{x}\cdot\mathbf{n})\nabla\cdot\underline{\mathbf{T}}]dS\Big] \quad \text{(A.1.15)}$$

We can obtain the final impulse-based force equation by inserting Eq. A.1.15 into Eq. A.1.4, where the pressure terms will cancel out:

$$\mathbf{F} = -\frac{\rho}{N-1}\frac{d}{dt}\int_{CV}\mathbf{x}\times\boldsymbol{\omega}dV + \frac{\rho}{N-1}\frac{d}{dt}\oint_{S_B}\mathbf{x}\times(\mathbf{n}\times\mathbf{u})dS + \oint_S \mathbf{n}\cdot\underline{\boldsymbol{\lambda}}dS \quad \text{(A.1.16)}$$

where the tensor $\underline{\boldsymbol{\lambda}}$ is:

$$\underline{\boldsymbol{\lambda}} = \frac{\rho}{2}(\mathbf{u}\cdot\mathbf{u})\underline{\mathbf{I}} - \rho\mathbf{u}\otimes\mathbf{u} - \frac{\rho}{N-1}\Big[\mathbf{u}\otimes(\mathbf{x}\times\boldsymbol{\omega}) + \boldsymbol{\omega}\otimes(\mathbf{x}\times\mathbf{u})\Big] + \frac{1}{N-1}\Big[\mathbf{x}\cdot(\nabla\cdot\underline{\mathbf{T}})\underline{\mathbf{I}} - \mathbf{x}\otimes(\nabla\cdot\underline{\mathbf{T}})\Big] + \underline{\mathbf{T}} \quad \text{(A.1.17)}$$

Note that N represents the number of dimensions of space (i.e. for 2D flows, $N = 2$ and for 3D flows, $N = 3$). The derivation of the more general impulse-based force equation that does not assume stationary control volume and impermeable airfoil surface is provided by Noca (1997).

A.2 Impulse-based moment equation

The conservation equation of angular momentum for a finite, stationary control volume bounded by an exterior surface S can be written as follows:

$$\mathbf{M} = -\rho\frac{d}{dt}\int_{CV}\mathbf{x}\times\mathbf{u}dV - \oint_S \mathbf{x}\times[\mathbf{n}\cdot(\rho\mathbf{u}\otimes\mathbf{u})]dS + \oint_S \mathbf{x}\times[\mathbf{n}\cdot(-p\underline{\mathbf{I}}+\underline{\mathbf{T}})]dS \quad \text{(A.2.1)}$$

Similar to the the force equation, the goal is to transform the first term of Eq. A.2.1 into a term that contains the vorticity using the DMT identity (Wu *et al.*, 2007*b*):

$$\int_{CV}\mathbf{x}\times\mathbf{u}dV = -\frac{1}{2}\int_{CV}(\mathbf{x}\cdot\mathbf{x})\boldsymbol{\omega}dV + \frac{1}{2}\oint_S(\mathbf{x}\cdot\mathbf{x})(\mathbf{n}\times\mathbf{u})dS + \frac{1}{2}\oint_{S_B}(\mathbf{x}\cdot\mathbf{x})(\mathbf{n}\times\mathbf{u})dS \quad \text{(A.2.2)}$$

Next insert Eq. A.2.2 into Eq. A.2.1:

$$\mathbf{M} = \frac{\rho}{2}\frac{d}{dt}\int_{CV}(\mathbf{x}\cdot\mathbf{x})\boldsymbol{\omega}dV - \frac{\rho}{2}\frac{d}{dt}\oint_S(\mathbf{x}\cdot\mathbf{x})(\mathbf{n}\times\mathbf{u})dS + \frac{\rho}{2}\frac{d}{dt}\oint_{S_B}(\mathbf{x}\cdot\mathbf{x})(\mathbf{n}\times\mathbf{u})dS - \oint_S \mathbf{x}\times[\mathbf{n}\cdot(\rho\mathbf{u}\otimes\mathbf{u})]dS + \oint_S \mathbf{x}\times[\mathbf{n}\cdot(-p\underline{\mathbf{I}}+\underline{\mathbf{T}})]dS \quad \text{(A.2.3)}$$

Using the Navier-Stokes equation (Eq. A.1.6), the second term can be re-written in the following form:

$$\frac{1}{2}\oint_S(\mathbf{x}\cdot\mathbf{x})\Big(\mathbf{n}\times\rho\frac{\partial\mathbf{u}}{\partial t}\Big)dS=\frac{1}{2}\oint_S(\mathbf{x}\cdot\mathbf{x})\Big(\mathbf{n}\times[-\nabla(p+\frac{\rho}{2}\mathbf{u}\cdot\mathbf{u})+\rho\mathbf{u}\times\boldsymbol{\omega}+\nabla\cdot\underline{\mathbf{T}}]\Big)dS \tag{A.2.4}$$

The integral that contains the pressure can be transformed to the following form:

$$\frac{1}{2}\oint_S(\mathbf{x}\cdot\mathbf{x})\Big(\mathbf{n}\times[-\nabla(p-\frac{\rho}{2}\mathbf{u}\cdot\mathbf{u})]\Big)dS=\oint_S\mathbf{x}\times\mathbf{n}\cdot(-p-\frac{\rho}{2}\mathbf{u}\cdot\mathbf{u})\underline{\mathbf{I}}dS \tag{A.2.5}$$

By inserting Eq. A.2.5 into Eq. A.2.4, and then into Eq. A.2.3 to get the following moment equation:

$$\begin{aligned}\mathbf{M}=&\frac{\rho}{2}\frac{d}{dt}\int_{CV}(\mathbf{x}\cdot\mathbf{x})\boldsymbol{\omega}dV-\frac{1}{2}\oint_S(\mathbf{x}\cdot\mathbf{x})\Big(\mathbf{n}\times[\rho\mathbf{u}\times\boldsymbol{\omega}+\nabla\cdot\underline{\mathbf{T}}]\Big)dS\\&+\frac{\rho}{2}\frac{d}{dt}\oint_{S_B}(\mathbf{x}\cdot\mathbf{x})(\mathbf{n}\times\mathbf{u})dS+\oint_S\mathbf{x}\times\mathbf{n}\cdot(p+\frac{\rho}{2}\mathbf{u}\cdot\mathbf{u})\underline{\mathbf{I}}dS\\&-\oint_S\mathbf{x}\times[\mathbf{n}\cdot(\rho\mathbf{u}\otimes\mathbf{u})]dS+\oint_S\mathbf{x}\times[\mathbf{n}\cdot(-p\underline{\mathbf{I}}+\underline{\mathbf{T}})]dS\end{aligned} \tag{A.2.6}$$

Note that the pressure terms can now be cancelled. Eq. A.2.6 is now re-arranged as follows:

$$\begin{aligned}\mathbf{M}=&\frac{\rho}{2}\frac{d}{dt}\int_{CV}(\mathbf{x}\cdot\mathbf{x})\boldsymbol{\omega}dV-\frac{\rho}{2}\oint_S(\mathbf{x}\cdot\mathbf{x})\Big(\mathbf{n}\times(\mathbf{u}\times\boldsymbol{\omega})\Big)dS-\frac{1}{2}\oint_S(\mathbf{x}\cdot\mathbf{x})\Big(\mathbf{n}\times(\nabla\cdot\underline{\mathbf{T}})\Big)dS\\&+\oint_S\mathbf{x}\times(\mathbf{n}\cdot\underline{\mathbf{T}})dS+\frac{\rho}{2}\frac{d}{dt}\oint_{S_B}(\mathbf{x}\cdot\mathbf{x})(\mathbf{n}\times\mathbf{u})dS+\rho\oint_S\mathbf{x}\times\mathbf{n}\cdot\Big[\Big(\frac{1}{2}\mathbf{u}\cdot\mathbf{u}\Big)\underline{\mathbf{I}}-\mathbf{u}\otimes\mathbf{u}\Big]dS\end{aligned} \tag{A.2.7}$$

Saffman (1992) has shown that the next to the last term can be written in terms of the lamb vector $(\mathbf{u}\times\boldsymbol{\omega})$:

$$\rho\oint_S\mathbf{x}\times\mathbf{n}\cdot\Big[\Big(\frac{1}{2}\mathbf{u}\cdot\mathbf{u}\Big)\underline{\mathbf{I}}-\mathbf{u}\otimes\mathbf{u}\Big]dS=\rho\int_{CV}\mathbf{x}\times(\mathbf{u}\times\boldsymbol{\omega})dV \tag{A.2.8}$$

Next, we combine the viscous and shear stress terms together:

$$\boldsymbol{\tau} = \oint_S \mathbf{x} \times (\mathbf{n} \cdot \underline{\mathbf{T}}) dS - \frac{1}{2} \oint_S (\mathbf{x} \cdot \mathbf{x}) \Big(\mathbf{n} \times (\nabla \cdot \underline{\mathbf{T}}) \Big) dS \tag{A.2.9}$$

Finally, the impulse-based moment equation can be written by combining Eq. A.2.9 and Eq. A.2.8 with Eq. A.2.7:

$$\mathbf{M} = \frac{\rho}{2} \frac{d}{dt} \int_{CV} (\mathbf{x} \cdot \mathbf{x}) \boldsymbol{\omega} dV + \rho \int_{CV} \mathbf{x} \times (\mathbf{u} \times \boldsymbol{\omega}) dV - \frac{\rho}{2} \oint_S (\mathbf{x} \cdot \mathbf{x}) \Big(\mathbf{n} \times (\mathbf{u} \times \boldsymbol{\omega}) \Big) dS + \frac{\rho}{2} \frac{d}{dt} \oint_{S_B} (\mathbf{x} \cdot \mathbf{x})(\mathbf{n} \times \mathbf{u}) dS + \boldsymbol{\tau} \tag{A.2.10}$$

Note that the second to last term represents the effect on the body motion on the aerodynamic moment.

Appendix B Uncertainty analysis

B.1 PIV uncertainty

The errors in determining the exact location of seed particle images taken using PIV may have a large impact on the calculated velocity vectors. Raffel *et al.* (2018) have shown that these errors arise from multiple sources, such as seeding density, particle image diameter, out-of-plane particle motion, background noise and large flow gradients. In this dissertation, we follow the correlation statistics method provided by Wieneke (2015) to estimate the uncertainty in velocity measurements. The idea of this method is to utilize the differences between the cross-correlation function that is obtained experimentally with the one that would be obtained under ideal situations (i.e. with no experimental errors). In an idealized situation of an exact particle position measurement, the particle images captured by the PIV camera match perfectly with each other, producing a symmetric correlation peak. However in real measurements, the paired images do not exactly match, and the disparity is reflected in a non-symmetric correlation peak. The position displacement vectors can then be derived from a statistical analysis of how each pixel contributes to the cross-correlation peak shape. The algorithm for this technique is implemented in DaVIS v8.4, and the details are provided by Wieneke (2015).

B.1.1 Characterization of the wind tunnel free stream flow

A typical profile of the free stream velocity in the wind tunnel is shown in Fig. B.1a. The maximum velocity uncertainty for all cases tested is approximately 0.3% of the free stream velocity. In Fig. B.1b, a contour plot of the turbulence intensity is provided, showing a maximum intensity of approximately 1%, with the majority of field of view having an intensity less than 0.5% of the free stream velocity. The

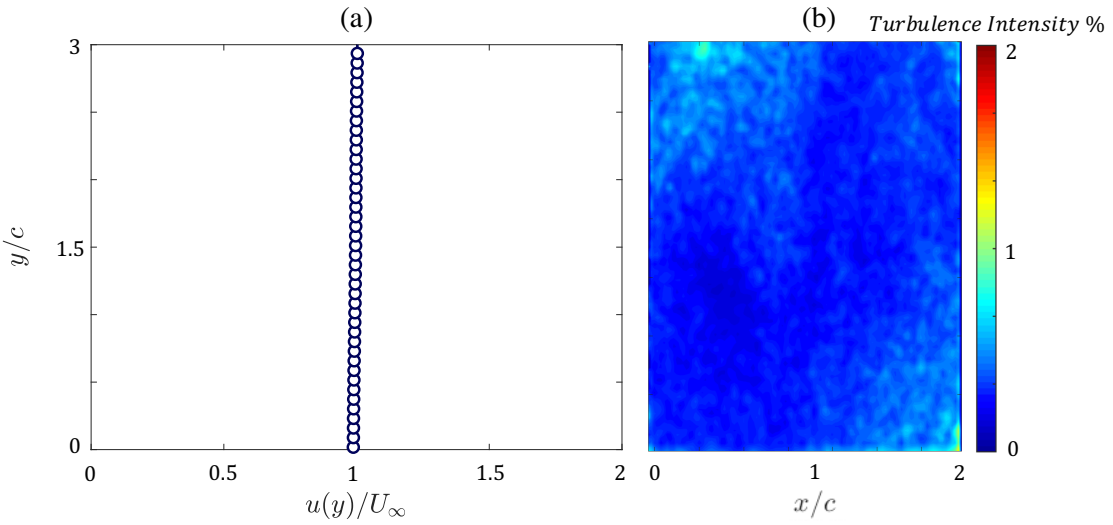

Figure B.1: (a) Typical velocity profile of the free stream flow in the wind tunnel and (b) contour plot of the turbulence intensity of the free stream flow.

turbulence intensity (TI) of a two-dimensional flow is calculated as follows:

$$TI = \frac{\sqrt{\frac{1}{2}(u'^2 + v'^2)}}{U_\infty} \times 100 \tag{B.1.1}$$

where u' and v' are the root-mean-square of the axial and normal velocity components, respectively. The velocity fluctuations are calculated using the classical Reynolds decomposition, where 500 time-resolved images (captured at a sampling frequency of 15 Hz) are used to calculate the mean flow.

B.1.2 Velocity field uncertainty

The velocity uncertainty is calculated using DaVIS v8.4. In Fig. B.2, we show a contour plot of the normalized velocity magnitude and its corresponding uncer-

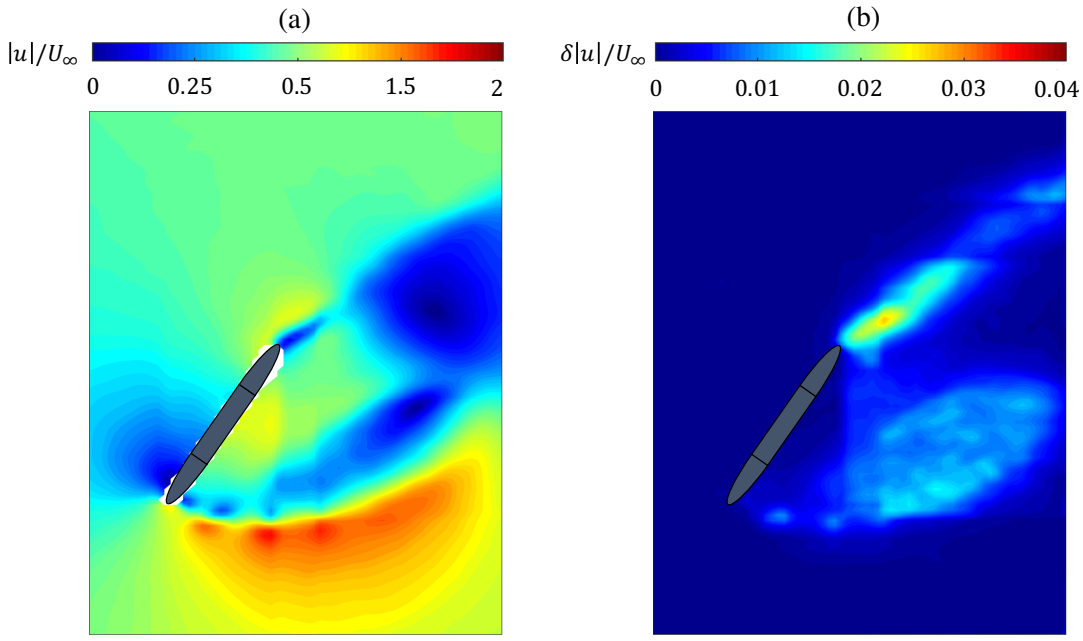

Figure B.2: (a) Normalized velocity magnitude and (b) corresponding uncertainty map.

tainty ($\delta|u|$) map. The velocity magnitude is defined as follows:

$$|u| = \sqrt{u^2 + v^2} \tag{B.1.2}$$

The largest estimated uncertainty in the velocity magnitude was found to be approximately 2.3% of the free stream velocity.

B.1.3 Vorticity field uncertainty

Here, we show how the measurement uncertainty in velocity can be propagated to the spanwise vorticity. The uncertainty propagated to any function F can be calculated as follows:

$$\delta F = \sqrt{\sum_J \left(\frac{\partial F}{\partial L_J}\delta L_J\right)^2} \tag{B.1.3}$$

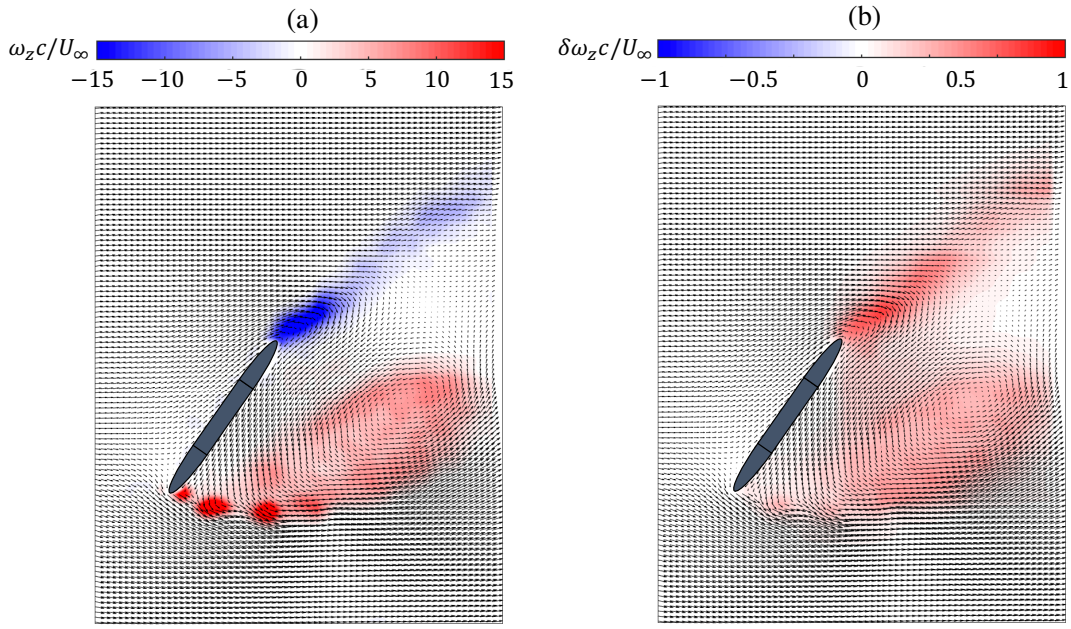

Figure B.3: (a) Normalized vorticity field showing LEV formation and trailing edge vorticity shedding and (b) corresponding uncertainty map.

where L_J is a set of variables on which the function F is dependent and δL_J represents the uncertainty of these variables. The vorticity is calculated from velocity using a central difference scheme:

$$\omega_z = \frac{1}{2h}(v_{i+1,j} - v_{i-1,j} - u_{i,j+1} + u_{i,j-1}) \tag{B.1.4}$$

where h is the grid-spacing which is the same in both directions of the domain. By combining Eq. B.1.3 and Eq. B.1.4, it can be shown that the uncertainty in the spanwise vorticity can written as:

$$\delta\omega_z = \frac{1}{2h}\sqrt{\delta v_{i+1,j}^2 + (-\delta v_{i-1,j})^2 + (-\delta u_{i,j+1})^2 + \delta u_{i,j-1}^2} \tag{B.1.5}$$

where δu and δv represent the uncertainty in the axial and normal velocity components, respectively. A typical vorticity field showing the LEV formation and

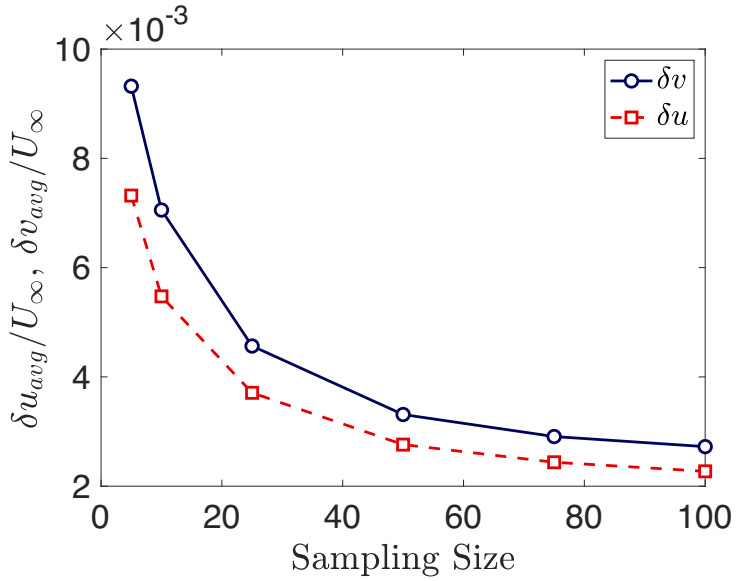

Figure B.4: Normalized average uncertainty of the axial and normal velocities as a function of sampling size.

trailing edge vorticity shedding and its corresponding uncertainty map are shown in Fig. B.3a and Fig. B.3b, respectively. The maximum observed vorticity uncertainty is approximately 9% of the maximum vorticity. Note that the discretization error due to spatial resolution of the central difference scheme is in the order of h^2. In this study, the dimensionless grid spacing $h^* = h/c$ is in the order of $\mathcal{O}(10^{-2})$, such that h^{*2} will be in the order of $\mathcal{O}(10^{-4})$. Because this is significantly smaller than the velocity uncertainty, the discretization error has been omitted in the calculation of vorticity uncertainty.

B.1.4 Effect of sampling size on the uncertainty

The effect of number of PIV images that is used for phase-averaging at each phase of interest on the velocity uncertainty and LEV vorticity is reported in this section. Fig. B4 shows the average calculated uncertainty of the axial and normal velocities

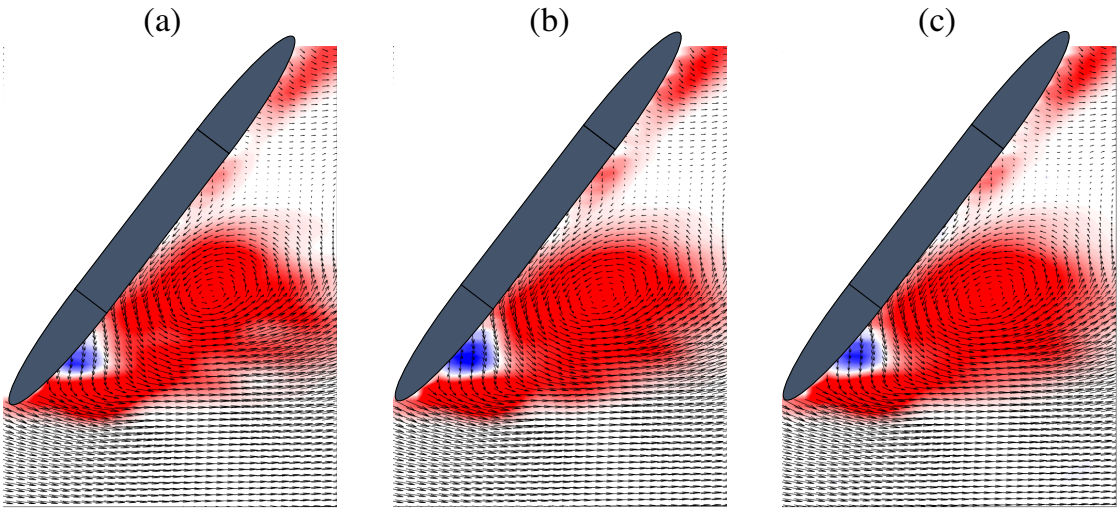

Figure B.5: Flow field calculated using (a) 10 images, (b) 50 images and (c) 100 images.

(normalized by the free stream velocity) in a typical velocity field as a function of the sampling size. As shown, the uncertainty decreases with increasing sampling size, and becomes approximately constant at a sampling size of 75. The maximum uncertainty in the axial and normal velocities observed in all experiments are 3.5% and 5.8% of the free stream velocity, respectively.

In Fig. B5, we show the variation in LEV vorticity for sampling sizes of 10, 50 and 100. It is quite clear that the velocity fields calculated using 50 and 100 phase-averaged images produce a more coherent LEV than the velocity field calculated using 10 images. Qualitatively, it is shown that when the sampling size is increased from 50 to 100 images, the LEV does not significantly change. Finally, it is important to quantify the effect of sampling size on LEV circulation and its uncertainty. The LEV circulation is calculated as follows:

$$\Gamma_{LEV} = \sum_{j} \omega_{z_j} dA_j \tag{B.1.6}$$

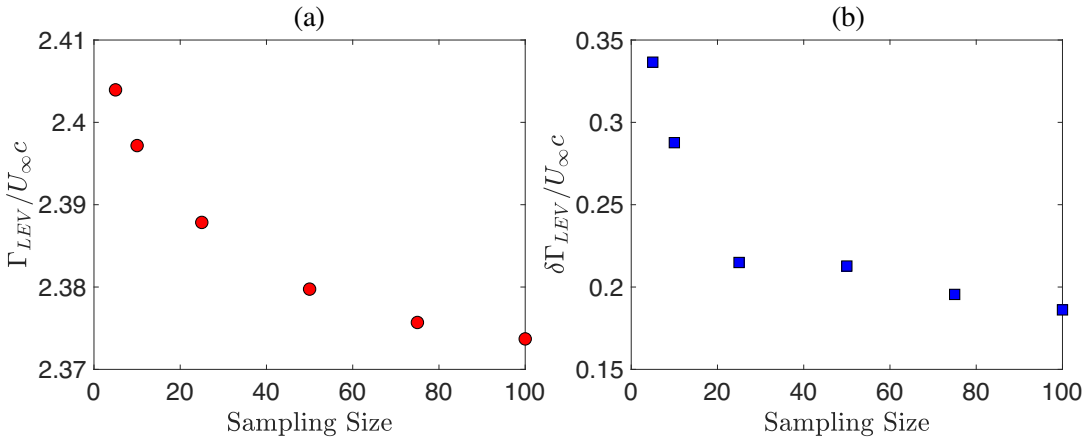

Figure B.6: (a) Normalized LEV circulation versus sampling size and (b) uncertainty in LEV circulation versus sampling size.

where dA is the differential area ($dA = h^2$) and the sum over the index j includes every data point in the two-dimensional vorticity field. Note that the summation is performed only within the LEV boundaries, as detected by the Γ_2 method described in Chapter 2. Using Eq. B.1.3, the uncertainty in LEV circulation can be written as follows:

$$\delta\Gamma_{LEV} = h^2 \sqrt{\sum_j \delta\omega_{z_j}^2} \tag{B.1.7}$$

The dependency of the normalized LEV circulation (the LEV shown in Fig. B.5) on the sampling size is shown in Fig. B.6a. As the sampling size increases the LEV circulation decreases, and it becomes approximately constant at a sampling size of 75. The reduction in circulation with increasing sampling size is a result of the vorticity field becoming smoother as the sampling size increases (i.e. the velocity gradients become smoother). Figure B.6b shows the uncertainty of LEV circulation with varying sampling size. As expected, the uncertainty decreases as the sampling size increases. While these uncertainties are specific to the LEV shown in Fig. B.5, a similar trend is observed for different experimental conditions at different phases during the oscillation cycle. The maximum uncertainty of LEV

circulation was determined to be approximately 6.7% of the circulation value.

B.2 Uncertainty in force and moment estimation

In this section, the analysis of uncertainty propagation from the velocity and vorticity fields to the lift force and aerodynamics moment is provided. The simplified force equation (see Chapter 2) is re-written here for convenience:

$$F_y = -\rho \frac{d}{dt} \int_{CV} x\omega_z dA + \rho \int_{CV} u\omega_z dA \tag{B.2.1}$$

and the simplified aerodynamic moment equation (see Chapter 3) is:

$$M_z = \frac{\rho}{2} \frac{d}{dt} \int_{CV} (x^2 + y^2)\omega_z dA + \rho \int_{CV} (yv\omega_z - xu\omega_z) dA \\ - \frac{\rho}{2} \oint_S (x^2 + y^2)(n_y v\omega_z - n_x u\omega_z) dS \tag{B.2.2}$$

First, we will look at the uncertainty of the rate of change of the impulse force ($F_{I,y}$) and impulse moment ($M_{I,z}$). These are the first terms of equations B.2.1 and B.2.2, respectively. The time derivatives were calculated using a central difference scheme, with a temporal discretization error in the order of $\mathcal{O}(10^{-5})$ and therefore its effect on the force and moment can be assumed to be negligible. In addition, the truncation error from the area integral can be shown using a two-dimensional taylor-series expansion to be in the order of $\mathcal{O}(10^{-8})$ and therefore it is also negligible. The uncertainty of both these terms can then be written as follows:

$$\delta F_{I,y} = \frac{\rho h^2}{2\Delta t} \sqrt{\sum_j x_j^2 \delta\omega_{z,j}^2} \tag{B.2.3}$$

$$\delta M_{I,z} = \frac{\rho h^2}{2\Delta t} \sqrt{\sum_j (x_j^2 + y_j^2)^2 \delta\omega_{z,j}^2} \tag{B.2.4}$$

The uncertainty in the contribution of the Lamb vector to the force ($F_{L,y}$, second term of Eq. B.2.1) and moment ($M_{L,z}$, second term of Eq. B.2.2) is:

$$\delta F_{L,y} = \rho h^2 \sqrt{\sum_j \omega_{z,j}^2 \delta u_j^2 + \sum_j u_j^2 \delta \omega_{z,j}^2} \tag{B.2.5}$$

$$\delta M_{L,z} = \rho h^2 \sqrt{\sum_j y_j^2 \omega_{z,j}^2 \delta v_j^2 + \sum_j y_j^2 u_j^2 \delta \omega_{z,j}^2 + \sum_j x_j^2 \omega_{z,j}^2 \delta u_j^2 + \sum_j x_j^2 u_j^2 \delta \omega_{z,j}^2} \tag{B.2.6}$$

Finally, the uncertainty in Lamb vector contribution to the surface integral ($M_{L,S,z}$, last term of Eq. B.2.2) is:

$$\begin{aligned}\delta M_{L,S,z} = \frac{h\rho}{2} \sqrt{\sum_m (x_m^2 + y_m^2)^2 v_m^2 \delta \omega_{z,m}^2 + \sum_m (x_m^2 + y_m^2)^2 \omega_{z,m}^2 \delta v_m^2} \\ + \sum_n (x_n^2 + y_n^2)^2 u_n^2 \delta \omega_{z,n}^2 + \sum_n (x_n^2 + y_n^2)^2 \omega_{z,n}^2 \delta u_n^2\end{aligned} \tag{B.2.7}$$

where m and n correspond to the summation along the x and y directions, respectively. The total uncertainty in the force and moment can then be written as:

$$\delta F_y = \sqrt{\delta F_{I,y}^2 + \delta F_{L,y}^2} \tag{B.2.8}$$

$$\delta M_z = \sqrt{\delta M_{I,z}^2 + \delta M_{L,z}^2 + \delta M_{L,S,z}^2} \tag{B.2.9}$$

B.3 Uncertainty in power output

The power output of an oscillating airfoil is written as:

$$P = F_y \dot{h} + M_z \dot{\theta} \tag{B.3.1}$$

The uncertainty in power output can be written as:

$$\delta P = \sqrt{F_y^2 \delta \dot{h}^2 + \dot{h}^2 \delta F_y^2 + M_z^2 \delta \dot{\theta}^2 + \dot{\theta} \delta M_z^2} \tag{B.3.2}$$

The uncertainty of the heaving and pitching velocities were found to be in the order of $\pm 10^{-3}$ m/s and $\pm 10^{-3}$ rad/s (Totpal, 2017).

Appendix C Full velocity field construction

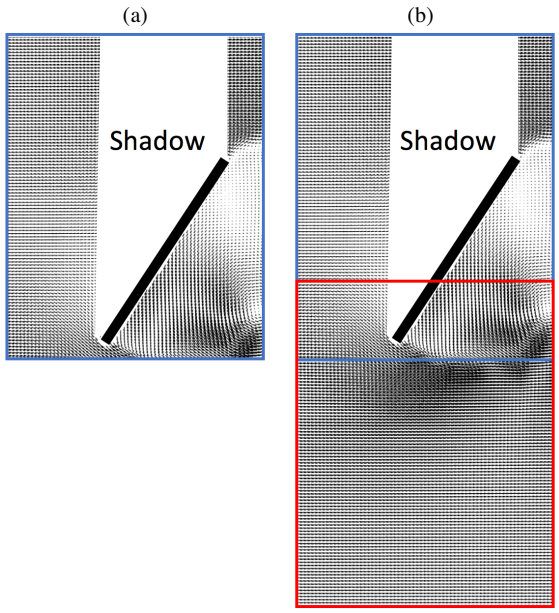

Figure C.1: (a) Velocity field obtained by a single camera and (b) velocity field obtained by two cameras.

The use of the impulse-based force and moment equations requires the knowledge of the velocity field that surrounds the entire airfoil. The airfoil kinematics used in this study are based on relatively large amplitudes of motion, such that a single PIV camera is not sufficient to capture the entire flow field. A sample velocity field captured by a single PIV camera is shown in Fig. C.1a. To resolve this issue, a second camera was used to capture the lower half of the downstroke motion of the airfoil. Figure C.1b shows the field of view (FOV) captured by both PIV cameras (one FOV is colored by a blue rectangle and the other is colored by a red rectangle). Note that there is an overlap of 22 vectors between the two FOVs. The

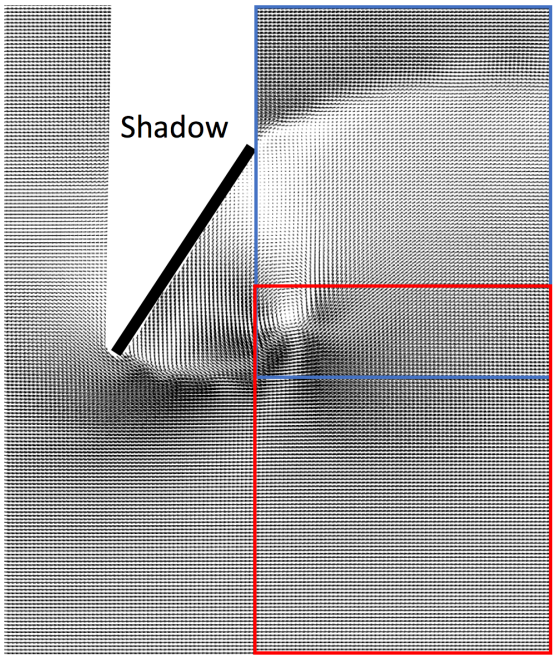

Figure C.2: Stitched upstream and wake FOVs.

overlapped region was smoothed using a 3x3 moving averaging filter. Fine-tuning the location of the cameras was performed using the calibration wizard in DaVIS v8.4.

The FOV shown in Fig. C.1b is still not sufficient, as the near wake is barely captured. DeVoria *et al.* (2014) have shown that to minimize the errors in impulse-based force estimation, the downstream boundary of the control volume should be located approximately 1 chord length downstream of the airfoil trailing edge. Since we only had two cameras to work with, the PIV cameras were moved downstream to a marked location, and all the experiments were repeated. The upstream and wake FOVs were then stitched together, and the result is shown in Fig. C.2.

Finally, in order to obtain velocity measurements in the shadow region (which is caused by the airfoil blocking the PIV laser sheet), the experiments were repeated at a phase delay of 180° for each phase of interest. The 180° out of phase velocity

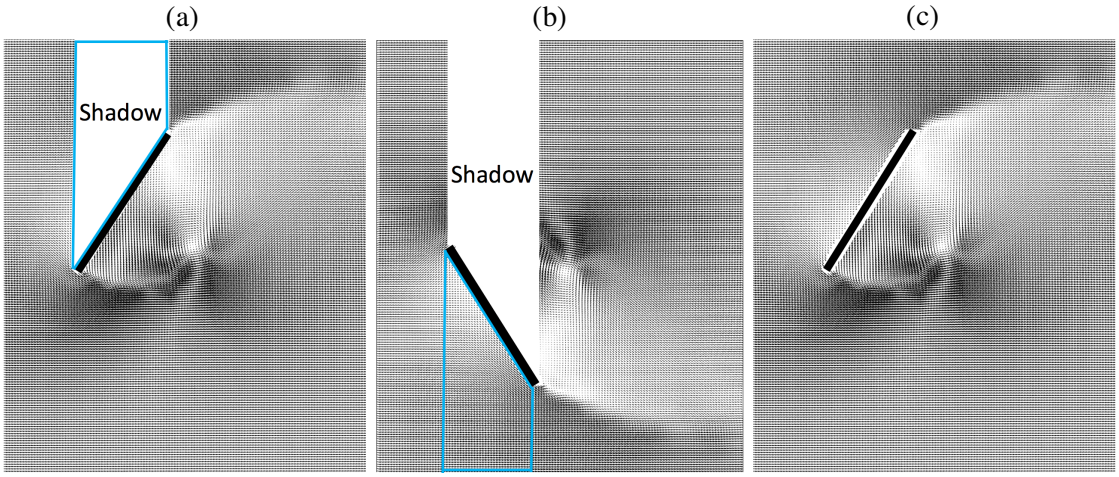

Figure C.3: (a) Velocity field with the shadow region, (b) 180° out of phase velocity field and (c) full velocity field.

fields were then mirrored and stitched to the rest of the velocity field to construct the full flow field surrounding the airfoil. This process is shown in Fig C.3.

One obvious concern with the full velocity field construction is the precision of the stitching process. If not carefully treated, the stitching process may result in noisy data due to the artificially increased velocity gradients in the overlapped region. An example of a noisy vorticity field is shown in Fig C.4a, where the vorticity was calculated after stitching the velocity fields. It can be seen that there is considerable noise in the vorticity, especially within the LEV where different FOV regions are overlapped. The noise levels in vorticity can be significantly decreased by calculating the vorticity of each FOV individually, and then stitch the vorticity fields together. This will ensure that the large velocity gradients caused by the stitching of the velocity fields do not contribute to vorticity calculation. The result is shown in Fig. C.4b.

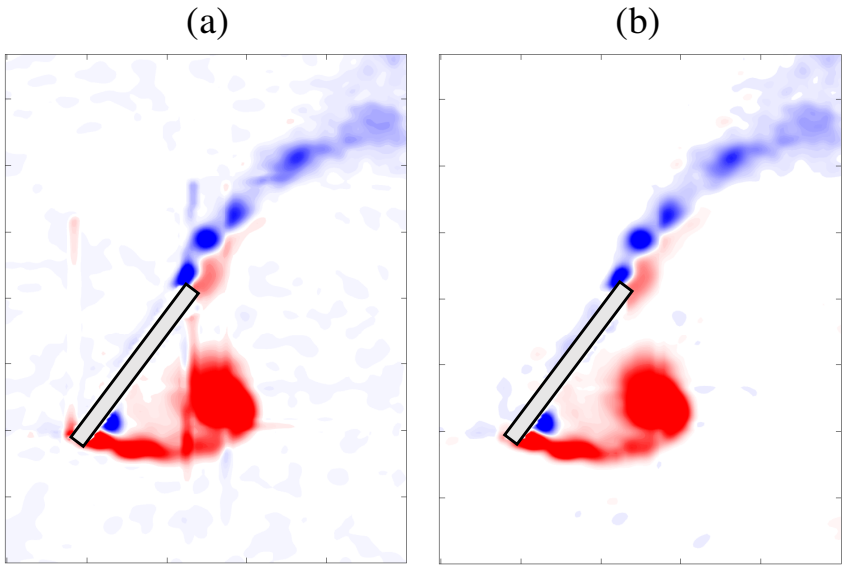

Figure C.4: (a) Vorticity field calculated after velocity field stitching and (b) vorticity field calculated prior to velocity field stitching.

Appendix D Impulse-based force equations: time-derivative of the force and moment impulse

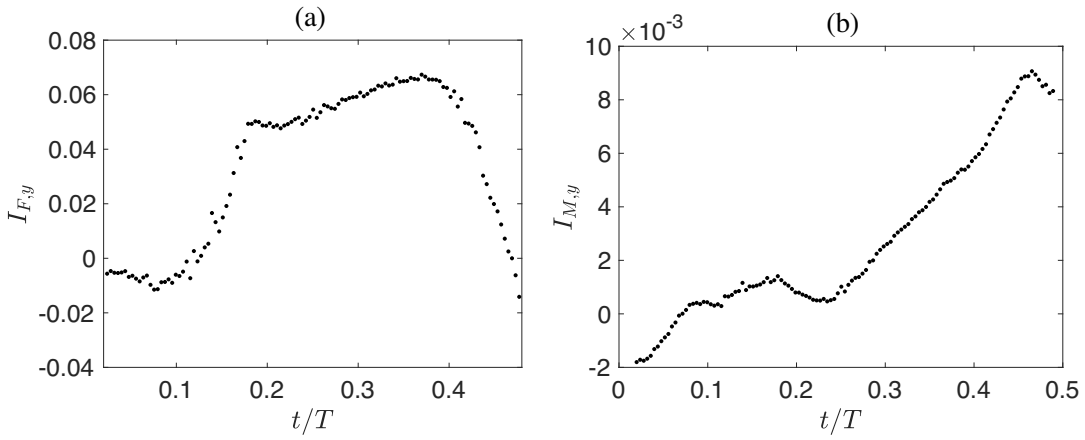

Figure D.1: An example of the raw (a) impulse force and (b) impulse moment versus time.

Using the impulse-based force and moment equations requires evaluating the time derivative of the vortex impulse:

$$F_{I,z} = -\rho \frac{d}{dt} \int_{CV} x\omega_z dA = -\rho \frac{dI_{F,y}}{dt} \tag{D.0.1}$$

$$M_{I,z} = \rho \frac{d}{dt} \int_{CV} (x^2 + y^2)\omega_z dA = \rho \frac{dI_{M,z}}{dt} \tag{D.0.2}$$

Prior to taking the time-derivative, it is important to ensure that the data are continuous and smooth. Examples of the raw data for $I_{F,y}$ and $I_{M,z}$ versus time are shown in Fig. D.1. One way to ensure the smoothness of the data is to fit it with a smoothing spline. A smoothing spline can be formed by a piece-wise

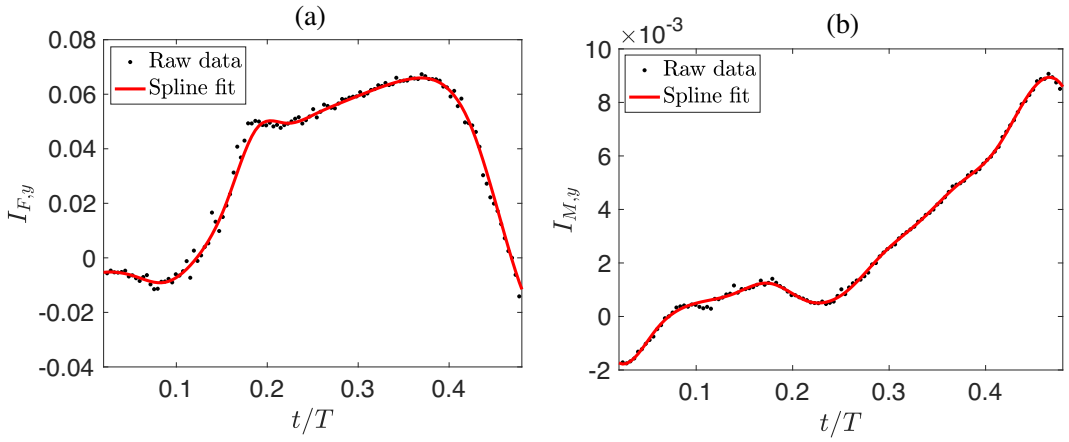

Figure D.2: Optimal spline fit applied to (a) impulse force and (b) impulse moment.

polynomial of degree n with $n-1$ continuous derivatives at each break point. In this work, a cubic ($n = 3$) is used. We follow the method developed by Epps *et al.* (2010) to determine the optimal spline fit. Essentially, the optimal spline fit is the one that follows the data as closely as possible without being affected by the roughness due to the noise in the data. We can characterize the error of a particular spline, $s(t)$, as follows:

$$E = \sum_{i=1}^{N} |\tilde{y}(t_i) - s(t_i)|^2 \Delta t \tag{D.0.3}$$

where $\tilde{y}$ is the data to be fitted. The cubic spline roughness is defined as:

$$R = \int_{t_1}^{t_N} \left| \frac{d^2 s}{dt^2} \right|^2 dt \tag{D.0.4}$$

Then, the optimal spline can be determined by minimizing the following quantity:

$$J = pE + (1-p)R \tag{D.0.5}$$

where p is the smoothing parameter which varies from 0 to 1, and it controls the

amount of smoothing applied to the spline. The value of p must be chosen *a priori*. If $p = 1$ is chosen, then minimizing the value of J requires minimizing the error E. On the other hand if $p = 0$ is chosen, then minimizing J requires minimizing the roughness R. The approach of the method developed by Epps *et al.* (2010) is to choose an error tolerance, E, and find the spline with the least roughness R. In this work, we chose an error tolerance of $1e^{-5}$. The objective then becomes to vary the spline parameters such as the number of break points and smoothness. An example of the optimal spline for the raw data shown in Fig. D.1 is provided in Fig. D.2.

Bibliography

Ansari, SA, Żbikowski, R & Knowles, Kevin 2006 Aerodynamic modelling of insect-like flapping flight for micro air vehicles. *Progress in Aerospace Sciences* **42** (2), 129–172.

Ashraf, MA, Young, J & Lai, JCS 2011*a* Reynolds number, thickness and camber effects on flapping airfoil propulsion. *Journal of Fluids and Structures* **27** (2), 145–160.

Ashraf, MA, Young, J, S. Lai, JC & Platzer, MF 2011*b* Numerical analysis of an oscillating-wing wind and hydropower generator. *AIAA Journal* **49** (7), 1374–1386.

Babinsky, Holger, Stevens, Robbie J, Jones, Anya R, Bernal, Luis P & Ol, Michael V 2016 Low order modelling of lift forces for unsteady pitching and surging wings. In *54th AIAA Aerospace Sciences Meeting*, p. 0290.

Baik, Yeon Sik, Bernal, Luis, Shyy, Wei & Ol, Michael 2011 Unsteady force generation and vortex dynamics of pitching and plunging flat plates at low reynolds number. In *49th AIAA Aerospace Sciences Meeting including the New Horizons Forum and Aerospace Exposition*, p. 220.

Baik, Yeon Sik, Bernal, Luis P, Granlund, Kenneth & Ol, Michael V 2012 Unsteady force generation and vortex dynamics of pitching and plunging aerofoils. *Journal of Fluid Mechanics* **709**, 37–68.

Batchelor, George Keith 2000 *An introduction to fluid dynamics*. Cambridge university press.

Birch, James M, Dickson, William B & Dickinson, Michael H 2004 Force production and flow structure of the leading edge vortex on flapping wings at high and low reynolds numbers. *Journal of Experimental Biology* **207** (7), 1063–1072.

Brown, CE 1954 Effect of leading-edge separation on the lift of a delta wing. *Journal of the Aeronautical Sciences* **21** (10), 690–694.

Brunton, Steven & Rowley, Clarence 2010 Unsteady aerodynamic models for agile flight at low reynolds number. In *48th AIAA Aerospace Sciences Meeting Including the New Horizons Forum and Aerospace Exposition*, p. 552.

Charonko, John J, King, Cameron V, Smith, Barton L & Vlachos, Pavlos P 2010 Assessment of pressure field calculations from particle image velocimetry measurements. *Measurement Science and Technology* **21** (10), 105401.

Chen, Di, Kolomenskiy, Dmitry, Nakata, Toshiyuki & Liu, Hao 2017 Forewings match the formation of leading-edge vortices and dominate aerodynamic force production in revolving insect wings. *Bioinspiration & Biomimetics* **13** (1), 016009.

Chin, Diana D & Lentink, David 2016 Flapping wing aerodynamics: from insects to vertebrates. *Journal of Experimental Biology* **219** (7), 920–932.

Cleaver, DJ, Gursul, Ismet, Calderon, DE & Wang, Zhijin 2014 Thrust enhancement due to flexible trailing-edge of plunging foils. *Journal of Fluids and Structures* **51**, 401–412.

Corkery, SJ, Babinsky, Holger & Graham, WR 2019 Quantification of added-mass effects using particle image velocimetry data for a translating and rotating flat plate. *Journal of Fluid Mechanics* **870**, 492–518.

Dabiri, John O 2009 Optimal vortex formation as a unifying principle in biological propulsion. *Annual Review of Fluid Mechanics* **41**, 17–33.

Dabiri, John O, Bose, Sanjeeb, Gemmell, Brad J, Colin, Sean P & Costello, John H 2014 An algorithm to estimate unsteady and quasi-steady pressure fields from velocity field measurements. *Journal of Experimental Biology* **217** (3), 331–336.

Darakananda, Darwin, Eldredge, Jeff, Colonius, Tim & Williams, David R 2016 A vortex sheet/point vortex dynamical model for unsteady separated flows. In *54th AIAA Aerospace Sciences Meeting*, p. 2072.

Dean, Robert C 1959 On the necessity of unsteady flow in fluid machines. *Journal of Basic Engineering* **81** (1), 24–28.

Deng, Jian, Caulfield, CP & Shao, Xueming 2014 Effect of aspect ratio on the energy extraction efficiency of three-dimensional flapping foils. *Physics of Fluids* **26** (4), 043102.

DeVoria, Adam C, Carr, Zakery R & Ringuette, Matthew J 2014 On calculating forces from the flow field with application to experimental volume data. *Journal of Fluid Mechanics* **749**, 297–319.

Dickinson, Michael H, Lehmann, Fritz-Olaf & Sane, Sanjay P 1999 Wing rotation and the aerodynamic basis of insect flight. *Science* **284** (5422), 1954–1960.

Dobrev, Ivan & Massouh, Fawaz 2011 Cfd and piv investigation of unsteady flow through savonius wind turbine. *Energy Procedia* **6**, 711–720.

Doligalski, TL, Smith, CR & Walker, JDA 1994 Vortex interactions with walls. *Annual Review of Fluid Mechanics* **26** (1), 573–616.

Dumas, G & Kinsey, T 2006 Eulerian simulations of oscillating airfoils in power extraction regime. *WIT Transactions on Engineering Sciences* **52**.

Dunne, Reeve & McKeon, Beverley J 2015 Dynamic stall on a pitching and surging airfoil. *Experiments in Fluids* **56** (8), 157.

Eldredge, Jeff D & Jones, Anya R 2019 Leading-edge vortices: mechanics and modeling. *Annual Review of Fluid Mechanics* **51**, 75–104.

Ellington, Charles P 1999 The novel aerodynamics of insect flight: applications to micro-air vehicles. *Journal of Experimental Biology* **202** (23), 3439–3448.

Ellington, Charles P, Van Den Berg, Coen, Willmott, Alexander P & Thomas, Adrian LR 1996 Leading-edge vortices in insect flight. *Nature* **384** (6610), 626.

Epps, Brenden P 2010 An impulse framework for hydrodynamic force analysis: fish propulsion, water entry of spheres, and marine propellers. PhD thesis, Massachusetts Institute of Technology.

Epps, Brenden P, Truscott, Tadd T & Techet, Alexandra H 2010 Evaluating derivatives of experimental data using smoothing splines. In *Proceedings of Mathematical Methods in Engineering International Symposium. MMEI, Lisbon Portugal*.

Ford, CW Pitt & Babinsky, Holger 2013 Lift and the leading-edge vortex. *Journal of Fluid Mechanics* **720**, 280–313.

Gharib, Morteza, Rambod, Edmond & Shariff, Karim 1998 A universal time scale for vortex ring formation. *Journal of Fluid Mechanics* **360**, 121–140.

Graftieaux, Laurent, Michard, Marc & Grosjean, Nathalie 2001 Combining piv, pod and vortex identification algorithms for the study of unsteady turbulent swirling flows. *Measurement Science and technology* **12** (9), 1422.

Gurka, Roi, Liberzon, Alex, Hefetz, D, Rubinstein, D & Shavit, U 1999 Computation of pressure distribution using piv velocity data. In *Workshop on Particle Image Velocimetry*, , vol. 2.

Hammer, Patrick, Altman, Aaron & Eastep, Frank 2014 Validation of a discrete vortex method for low reynolds number unsteady flows. *AIAA Journal* **52** (3), 643–649.

Hansen, Martin OL 2015 *Aerodynamics of wind turbines*. Routledge.

Hedenström, Anders & Johansson, L Christoffer 2015 Bat flight: aerodynamics, kinematics and flight morphology. *Journal of Experimental Biology* **218** (5), 653–663.

Ho, Steven, Nassef, Hany, Pornsinsirirak, Nick, Tai, Yu-Chong & Ho, Chih-Ming 2003 Unsteady aerodynamics and flow control for flapping wing flyers. *Progress in Aerospace Sciences* **39** (8), 635–681.

Hoke, CM, Young, J & Lai, JCS 2015 Effects of time-varying camber deformation on flapping foil propulsion and power extraction. *Journal of Fluids and Structures* **56**, 152–176.

Hubel, Tatjana Y, Hristov, Nickolay I, Swartz, Sharon M & Breuer, Kenneth S 2009 Time-resolved wake structure and kinematics of bat flight. *Experiments in Fluids* **46** (5), 933.

Hubel, Tatjana Y & Tropea, Cameron 2010 The importance of leading edge vortices under simplified flapping flight conditions at the size scale of birds. *Journal of Experimental Biology* **213** (11), 1930–1939.

Jones, K, Platzer, M, Jones, K & Platzer, M 1997 Numerical computation of flapping-wing propulsion and power extraction. In *35th Aerospace Sciences Meeting and Exhibit*, p. 826.

Kang, LL, Liu, LQ, Su, WD & Wu, JZ 2018 Minimum-domain impulse theory for unsteady aerodynamic force. *Physics of Fluids* **30** (1), 016107.

Karbasian, HR, Esfahani, Javad Abolfazli & Barati, E 2016 The power extraction by flapping foil hydrokinetic turbine in swing arm mode. *Renewable Energy* **88**, 130–142.

Kármán, Th von 1938 Airfoil theory for non-uniform motion. *Journal of the Aeronautical Sciences* **5** (10), 379–390.

Kim, Daegyoum, Hussain, Fazle & Gharib, Morteza 2013 Vortex dynamics of clapping plates. *Journal of Fluid Mechanics* **714**, 5–23.

Kim, Daegyoum, Strom, Benjamin, Mandre, Shreyas & Breuer, Kenneth 2017 Energy harvesting performance and flow structure of an oscillating hydrofoil with finite span. *Journal of Fluids and Structures* **70**, 314–326.

Kinsey, Thomas & Dumas, Guy 2008 Parametric study of an oscillating airfoil in a power-extraction regime. *AIAA Journal* **46** (6), 1318–1330.

Kinsey, Thomas & Dumas, Guy 2012 Computational fluid dynamics analysis of a hydrokinetic turbine based on oscillating hydrofoils. *Journal of Fluids Engineering* **134** (2), 021104.

Lamb, Horace 1932 *Hydrodynamics*. Cambridge university press.

Le, Tuyen Quang, Ko, Jin Hwan & Byun, Doyoung 2013 Morphological effect of a scallop shell on a flapping-type tidal stream generator. *Bioinspiration & Biomimetics* **8** (3), 036009.

Leishman, J Gordon 1994 Unsteady lift of a flapped airfoil by indicial concepts. *Journal of Aircraft* **31** (2), 288–297.

Li, Gao-Jin & Lu, Xi-Yun 2012 Force and power of flapping plates in a fluid. *Journal of Fluid Mechanics* **712**, 598–613.

Li, Juan & Wu, Zi-Niu 2015 Unsteady lift for the wagner problem in the presence of additional leading/trailing edge vortices. *Journal of Fluid Mechanics* **769**, 182–217.

Li, Juan & Wu, Zi-Niu 2016 A vortex force study for a flat plate at high angle of attack. *Journal of Fluid Mechanics* **801**, 222–249.

Lighthill, James 1986*a* Fundamentals concerning wave loading on offshore structures. *Journal of Fluid Mechanics* **173**, 667–681.

Lighthill, James 1986*b* An informal introduction to theoretical fluid mechanics .

Lin, J-C & Rockwell, D 1996 Force identification by vorticity fields: techniques based on flow imaging. *Journal of Fluids and Structures* **10** (6), 663–668.

Liu, Wendi, Xiao, Qing & Cheng, Fai 2013 A bio-inspired study on tidal energy extraction with flexible flapping wings. *Bioinspiration & Biomimetics* **8** (3), 036011.

Liu, Xiaofeng & Katz, Joseph 2006 Instantaneous pressure and material acceleration measurements using a four-exposure piv system. *Experiments in Fluids* **41** (2), 227.

Liu, Zhengliang, Lai, Joseph CS, Young, John & Tian, Fang-Bao 2016 Discrete vortex method with flow separation corrections for flapping-foil power generators. *AIAA Journal* **55** (2), 410–418.

Liu, Zhengliang, Tian, Fang-Bao, Young, John & Lai, Joseph CS 2017 Flapping foil power generator performance enhanced with a spring-connected tail. *Physics of Fluids* **29** (12), 123601.

Lu, Kun, Xie, Yonghui & Zhang, Di 2014 Nonsinusoidal motion effects on energy extraction performance of a flapping foil. *Renewable Energy* **64**, 283–293.

Lu, Kun, Xie, Yonghui, Zhang, Di & Xie, Gongnan 2015 Systematic investigation of the flow evolution and energy extraction performance of a flapping-airfoil power generator. *Energy* **89**, 138–147.

Lua, KB, Zhang, XH, Lim, TT & Yeo, KS 2015 Effects of pitching phase angle and amplitude on a two-dimensional flapping wing in hovering mode. *Experiments in Fluids* **56** (2), 35.

Ma, Penglei, Yang, Zhihong, Wang, Yong, Liu, Haibin & Xie, Yudong 2017 Energy extraction and hydrodynamic behavior analysis by an oscillating hydrofoil device. *Renewable Energy* **113**, 648–659.

Mackowski, AW & Williamson, CHK 2015 Direct measurement of thrust and efficiency of an airfoil undergoing pure pitching. *Journal of Fluid Mechanics* **765**, 524–543.

Madangopal, Rajkiran, Khan, Zaeem A & Agrawal, Sunil K 2005 Biologically inspired design of small flapping wing air vehicles using four-bar mechanisms and quasi-steady aerodynamics. *Journal of Mechanical Design* **127** (4), 809–816.

McKinney, William & DeLaurier, James 1981 Wingmill: an oscillating-wing windmill. *Journal of Energy* **5** (2), 109–115.

Miao, J-M & Ho, M-H 2006 Effect of flexure on aerodynamic propulsive efficiency of flapping flexible airfoil. *Journal of Fluids and Structures* **22** (3), 401–419.

Milano, Michele & Gharib, Morteza 2005 Uncovering the physics of flapping flat plates with artificial evolution. *Journal of Fluid Mechanics* **534**, 403–409.

Mohebbian, Ali & Rival, David E 2012 Assessment of the derivative-moment transformation method for unsteady-load estimation. *Experiments in Fluids* **53** (2), 319–330.

Moriche, Manuel, Flores, Oscar & Garcia-Villalba, Manuel 2017 On the aerodynamic forces on heaving and pitching airfoils at low reynolds number. *Journal of Fluid Mechanics* **828**, 395–423.

Morse, Daniel R & Liburdy, James A 2009 Vortex dynamics and shedding of a low aspect ratio, flat wing at low reynolds numbers and high angles of attack. *Journal of Fluids Engineering* **131** (5), 051202.

Mueller, Thomas J 2001 *Fixed and flapping wing aerodynamics for micro air vehicle applications*. American Institute of Aeronautics and Astronautics.

Muijres, FT, Johansson, L Christoffer, Barfield, Ryan, Wolf, Marta, Spedding, GR & Hedenström, Anders 2008 Leading-edge vortex improves lift in slow-flying bats. *Science* **319** (5867), 1250–1253.

Nakata, Toshiyuki & Liu, Hao 2012 A fluid–structure interaction model of insect flight with flexible wings. *Journal of Computational Physics* **231** (4), 1822–1847.

Nakata, T, Liu, H, Tanaka, Y, Nishihashi, N, Wang, X & Sato, A 2011 Aerodynamics of a bio-inspired flexible flapping-wing micro air vehicle. *Bioinspiration & Biomimetics* **6** (4), 045002.

Noca, Flavio 1997 On the evaluation of time-dependent fluid-dynamic forces on bluff bodies. Phd dissertation, Pasadena, CA.

Noca, F, Shiels, D & Jeon, D 1999 A comparison of methods for evaluating time-dependent fluid dynamic forces on bodies, using only velocity fields and their derivatives. *Journal of Fluids and Structures* **13** (5), 551–578.

Onoue, Kyohei & Breuer, Kenneth S 2016 Vortex formation and shedding from a cyber-physical pitching plate. *Journal of Fluid Mechanics* **793**, 229–247.

Peng, Zhangli & Zhu, Qiang 2009 Energy harvesting through flow-induced oscillations of a foil. *Physics of Fluids* **21** (12), 123602.

Platzer, Max F, Jones, Kevin D, Young, John & S. Lai, JC 2008 Flapping wing aerodynamics: progress and challenges. *AIAA Journal* **46** (9), 2136–2149.

Polhamus, Edward C 1971 Predictions of vortex-lift characteristics by a leading-edge suctionanalogy. *Journal of Aircraft* **8** (4), 193–199.

Prier, Michael W 2018 Energy harvesting performance of a flapping foil with leading edge motion. Ms thesis, Oregon State University, Corvallis, OR.

Raffel, Markus, Willert, Christian E, Scarano, Fulvio, Kähler, Christian J, Wereley, Steve T & Kompenhans, Jürgen 2018 *Particle image velocimetry: a practical guide*. Springer.

Ramesh, Kiran, Gopalarathnam, Ashok, Granlund, Kenneth, Ol, Michael V & Edwards, Jack R 2014 Discrete-vortex method with novel shedding criterion for unsteady aerofoil flows with intermittent leading-edge vortex shedding. *Journal of Fluid Mechanics* **751**, 500–538.

Rival, David, Prangemeier, Tim & Tropea, Cameron 2009 The influence of airfoil kinematics on the formation of leading-edge vortices in bio-inspired flight. *Experiments in Fluids* **46** (5), 823–833.

Rival, David E, Kriegseis, Jochen, Schaub, Pascal, Widmann, Alexander & Tropea, Cameron 2014 Characteristic length scales for vortex detachment on plunging profiles with varying leading-edge geometry. *Experiments in Fluids* **55** (1), 1660.

Saffman, Philip G 1992 *Vortex dynamics*. Cambridge university press.

Saidur, R, Rahim, NA, Islam, MR & Solangi, KH 2011 Environmental impact of wind energy. *Renewable and Sustainable Energy Reviews* **15** (5), 2423–2430.

Sane, Sanjay P 2003 The aerodynamics of insect flight. *Journal of Experimental Biology* **206** (23), 4191–4208.

Sciacchitano, Andrea & Wieneke, Bernhard 2016 Piv uncertainty propagation. *Measurement Science and Technology* **27** (8), 084006.

Seddon, John & Newman, Simon 2001 *Basic helicopter aerodynamics*. American Institute of Aeronautics and Astronautics.

Shyy, Wei, Lian, Yongsheng, Tang, Jian, Viieru, Dragos & Liu, Hao 2007 *Aerodynamics of low Reynolds number flyers*, , vol. 22. Cambridge University Press.

Siala, FF & Liburdy, JA 2019*a* Leading edge vortex dynamics and impulse-based lift force analysis of oscillating airfoils. *Under Revision, Experiments in Fluids* .

Siala, Firas & Liburdy, James A 2015 Energy harvesting of a heaving and forward pitching wing with a passively actuated trailing edge. *Journal of Fluids and Structures* **57**, 1–14.

Siala, Firas F & Liburdy, James A 2019*b* Leading edge vortex dynamics and impulse-based lift force analysis of oscillating airfoils. *Experiments in Fluids, Under Review* .

Siala, Firas F & Liburdy, James A 2019*c* Power estimation of flapping foil energy harvesters using vortex impulse theory. *Renewable Energy, Under Review* .

Siala, Firas F, Prier, Michael W & Liburdy, James A 2018 Force production mechanisms of a heaving and pitching foil operating in the energy harvesting regime. In *ASME 2018 5th Joint US-European Fluids Engineering Division Summer Meeting*, pp. V001T07A002–V001T07A002. American Society of Mechanical Engineers.

Siala, Firas F, Totpal, Alexander D & Liburdy, James A 2017 Optimal leading edge vortex formation of a flapping foil in energy harvesting regime. In *ASME 2017 Fluids Engineering Division Summer Meeting*, pp. V01CT23A008–V01CT23A008. American Society of Mechanical Engineers.

Srygley, RB & Thomas, ALR 2002 Unconventional lift-generating mechanisms in free-flying butterflies. *Nature* **420** (6916), 660.

Stevens, PRRJ & Babinsky, Holger 2017 Experiments to investigate lift production mechanisms on pitching flat plates. *Experiments in Fluids* **58** (1), 7.

Tchieu, Andrew A & Leonard, Anthony 2011 A discrete-vortex model for the arbitrary motion of a thin airfoil with fluidic control. *Journal of Fluids and Structures* **27** (5-6), 680–693.

Theodorsen, T 1934 Naca report 496: General theory of aerodynamic instability and the mechanism of flutter. *Tech. Rep.*. VA, USA: Advisory Committee for Aeronautics.

Tian, Fang-Bao, Young, John & Lai, Joseph CS 2014 Improving power-extraction efficiency of a flapping plate: From passive deformation to active control. *Journal of Fluids and Structures* **51**, 384–392.

Torbert, Shane 2016 *Applied computer science*. Springer.

Totpal, Alexander D. 2017 The energy extraction performance of an oscillating rigid and flexible foil. Ms thesis, Oregon State University, Corvallis, OR.

Totpal, Alexander D, Siala, Firas F & Liburdy, James A 2017 Flow energy harvesting of an oscillating foil with rigid and passive surface flexibility. In *ASME 2017 Fluids Engineering Division Summer Meeting*, pp. V01CT19A002–V01CT19A002. American Society of Mechanical Engineers.

Totpal, Alexander D, Siala, Firas F & Liburdy, James A 2018 Energy harvesting of an oscillating foil at low reduced frequencies with rigid and passively deforming leading edge. *Journal of Fluids and Structures* **82**, 329–342.

Triantafyllou, George S, Triantafyllou, MS & Grosenbaugh, MA 1993 Optimal thrust development in oscillating foils with application to fish propulsion. *Journal of Fluids and Structures* **7** (2), 205–224.

Tuncer, Ismail H & Kaya, Mustafa 2005 Optimization of flapping airfoils for maximum thrust and propulsive efficiency. *AIAA Journal* **43** (11), 2329–2336.

Tuncer, Ismail H & Platzer, Max F 2000 Computational study of flapping airfoil aerodynamics. *Journal of Aircraft* **37** (3), 514–520.

Van Oudheusden, BW 2013 Piv-based pressure measurement. *Measurement Science and Technology* **24** (3), 032001.

Villegas, Arturo & Diez, F Javier 2014 On the quasi-instantaneous aerodynamic load and pressure field measurements on turbines by non-intrusive piv. *Renewable Energy* **63**, 181–193.

Wagner, Herbert 1925 Über die entstehung des dynamischen auftriebes von tragflügeln. *ZAMM-Journal of Applied Mathematics and Mechanics/Zeitschrift für Angewandte Mathematik und Mechanik* **5** (1), 17–35.

Wang, Chengjie & Eldredge, Jeff D 2013 Low-order phenomenological modeling of leading-edge vortex formation. *Theoretical and Computational Fluid Dynamics* **27** (5), 577–598.

Widmann, A & Tropea, C 2015 Parameters influencing vortex growth and detachment on unsteady aerodynamic profiles. *Journal of Fluid Mechanics* **773**, 432–459.

Wieneke, Bernhard 2015 Piv uncertainty quantification from correlation statistics. *Measurement Science and Technology* **26** (7), 074002.

Willert, Christian E & Gharib, Morteza 1991 Digital particle image velocimetry. *Experiments in Fluids* **10** (4), 181–193.

Williamson, Charles HK & Roshko, Anatol 1988 Vortex formation in the wake of an oscillating cylinder. *Journal of Fluids and Structures* **2** (4), 355–381.

Wong, Jaime G & Rival, David E 2015 Determining the relative stability of leading-edge vortices on nominally two-dimensional flapping profiles. *Journal of Fluid Mechanics* **766**, 611–625.

Wu, James C 1981 Theory for aerodynamic force and moment in viscous flows. *AIAA Journal* **19** (4), 432–441.

Wu, J-Z, Lu, X-Y & Zhuang, L-X 2007*a* Integral force acting on a body due to local flow structures. *Journal of Fluid Mechanics* **576**, 265–286.

Wu, Jie-Zhi, Ma, Hui-Yang & Zhou, M-D 2007*b* *Vorticity and vortex dynamics*. Springer Science & Business Media.

Xia, X & Mohseni, K 2013 Lift evaluation of a two-dimensional pitching flat plate. *Physics of Fluids* **25** (9), 091901.

Xiao, Qing, Liao, Wei, Yang, Shuchi & Peng, Yan 2012 How motion trajectory affects energy extraction performance of a biomimic energy generator with an oscillating foil? *Renewable Energy* **37** (1), 61–75.

Xiao, Qing & Zhu, Qiang 2014 A review on flow energy harvesters based on flapping foils. *Journal of Fluids and Structures* **46**, 174–191.

Xie, Yonghui, Lu, Kun & Zhang, Di 2014 Investigation on energy extraction performance of an oscillating foil with modified flapping motion. *Renewable Energy* **63**, 550–557.

Young, John, Lai, Joseph CS & Platzer, Max F 2014 A review of progress and challenges in flapping foil power generation. *Progress in Aerospace Sciences* **67**, 2–28.

Zhao, Liang, Deng, Xinyan & Sane, Sanjay P 2011 Modulation of leading edge vorticity and aerodynamic forces in flexible flapping wings. *Bioinspiration & Biomimetics* **6** (3), 036007.

Zhu, Qiang 2011 Optimal frequency for flow energy harvesting of a flapping foil. *Journal of Fluid Mechanics* **675**, 495–517.